Ore Geology Reviews 194 (2026) 107345

Contents lists available at ScienceDirect

Ore Geology Reviews

journal homepage: www.elsevier.com/locate/oregeorev

Low-sulfidation epithermal mineralization in a post-subduction setting: Insights from the Eocene Gicik Au-Ag ± Te deposit, North-Central Anatolia (Türkiye)

Akın Çil, Ali İmer *

Department of Geological Engineering, Middle East Technical University, Ankara 06800, Türkiye

A B S T R A C T

The Turkish segment of the Western Tethyan Metallogenic Belt hosts numerous epithermal deposits; however, parts of north-central Anatolia remain underexplored, limiting understanding of mineralization styles and tectonomagmatic controls in this sector. The Gicik Au–Ag ± Te deposit, located along the southern Pontide margin, provides an opportunity to address this gap. This study aims to characterize the geology, mineralization styles, and timing of the Gicik epithermal system, and to constrain its relationship with regional tectonomagmatic evolution through field observations combined with mineralogical, geochemical, and geochronological analyses.

Mineralized veins are hosted by a volcanic–volcaniclastic sequence composed of medium-K calc-alkaline dacitic agglomerates and lavas displaying arc-like geochemical signatures. Low-sulfidation-style epithermal Au-Ag ± Te mineralization occurs along sub-vertical veins emplaced within NNE-trending oblique-slip faults. A core of silicification passes first into vein-proximal argillic alteration and then into a broader zone of propylitic alteration. Veins display superimposed textures including stockwork and lattice-bladed veins as well as multi-stage colloform banding and hydrothermal brecciation. Two distinct stages of mineralization were identified in association with these textures. Early stage is comprised by pyrite-arsenopyrite-marcasite with refractory gold primarily occurring in colloform-banded, massive silica, and lattice-bladed veins. Main Au-Ag-Te mineralization occurs in late breccia veins consisting of pyrite, Ag-tetrahedrite, native Au, tellurides, and rare selenides.

Overlapping ages of volcanic hosts and hydrothermal illite suggest that the Gicik epithermal system was spatio-temporally associated with middle Eocene (~44.5 Ma) magmatism that post-dated Pontide–Anatolide-Tauride collision. Formation of low-sulfidation epithermal mineralization was controlled by NNE-trending, transpressional structures developed during the advanced stages of collision.

1. Introduction

The convergence between the Pontide and Anatolide-Tauride fragments during the Mesozoic was culminated in the closure of the northern branch of the Neotethys ocean basin, followed by widespread collisional to post-collisional magmatic activity in northern Türkiye. The resulting extensive Eocene magmatic belt (>1400 km-long) stretches between the Lesser Caucasus in the east and Biga Peninsula in the west (Fig. 1A), and predominantly comprises calc-alkaline, felsic to intermediate composition plutonic and volcanic/volcaniclastic rocks. A large number of magmatic-hydrothermal deposits are hosted by these igneous systems including the regionally significant deposits such as the Lapseki, Kartaldağ/Madendağ (Ünal-İmer et al., 2013), and TV Tower epithermal Au (Leroux, 2016) and the Halilağa porphyry Cu-Au deposits (Brunetti, 2016) in the Biga Peninsula, the Kaymaz orogenic Au (Demirbilek et al., 2018) and Muratdere porphyry Cu-Mo-Re (Kuşcu et al., 2019; McFall et al., 2019) systems in the Eskişehir-Bursa district (Fig. 1A), and the Mastra (Bilir, 2015) and Bahçecik epithermal Au (Revan et al., 2024), Ardala porphyry Cu-Au-Mo and Salınbaş carbonate-replacement Au systems (Rabayrol et al., 2021; Çil et al., 2025) in the Eastern Pontides. A good understanding of the mineralization potential and metallogenic significance of the eastern (Eastern Pontides) and western segments (Biga Peninsula) of the belt has already been established during the past two decades. However, the central part of the belt remaining to the north of the Kırşehir Massif has been relatively underexplored for similar styles of magmatic-hydrothermal mineralization. Several epithermal and porphyry prospects have been identified, but no major deposits of Eocene age have been discovered yet.

The Gicik Au-Ag ± Te deposit is located around the small town of Gicik located ~ 15 km north of Ankara city center. It appears to be the most significant mineralization that has been discovered to date in north central Anatolia associated with Eocene magmatic activity. In addition, epithermal veins at Gicik are locally enriched in tellurium, a feature that is either uncommon or overlooked for most magmatic-hydrothermal

* Corresponding author.
E-mail address: aimer@metu.edu.tr (A. İmer).

https://doi.org/10.1016/j.oregeorev.2026.107345
Received 8 December 2025; Received in revised form 31 March 2026; Accepted 29 May 2026
Available online 1 June 2026
0169-1368/© 2026 The Authors. Published by Elsevier B.V. This is an open access article under the CC BY license (http://creativecommons.org/licenses/by/4.0/).

systems in this part of the metallogenic belt. Epithermal-style veins were discovered during the late 1980s by Eurogold through soil and channel sampling, geophysical surveys, and detailed geological mapping. Later, 26 diamond drill holes totaling approximately 2,500 m were completed mainly targeting the exposed veins. Koza Gold acquired the project in 2005 and carried out follow-up drilling until 2023, completing an additional 144 diamond drill holes. Small-scale open pit (later back-filled) mining of the higher-grade Au-Ag ore was also carried out in 2009, which resulted in production of about 2,800 oz of gold and 4,100 oz of silver (Koza Altın İşletmeleri A.Ş. Annual Activity Report, 2025).

Despite detailed and prolonged exploration efforts, the mineralized vein system at Gicik remained understudied. In an earlier study with a regional focus, Besbelli and Varol (2002) provided mineralogical data from hydrothermally-altered rocks from one of the main vein exposures near Gicik. Their findings indicated that the siliceous veins are surrounded by zones of silicification and argillic alteration (predominantly

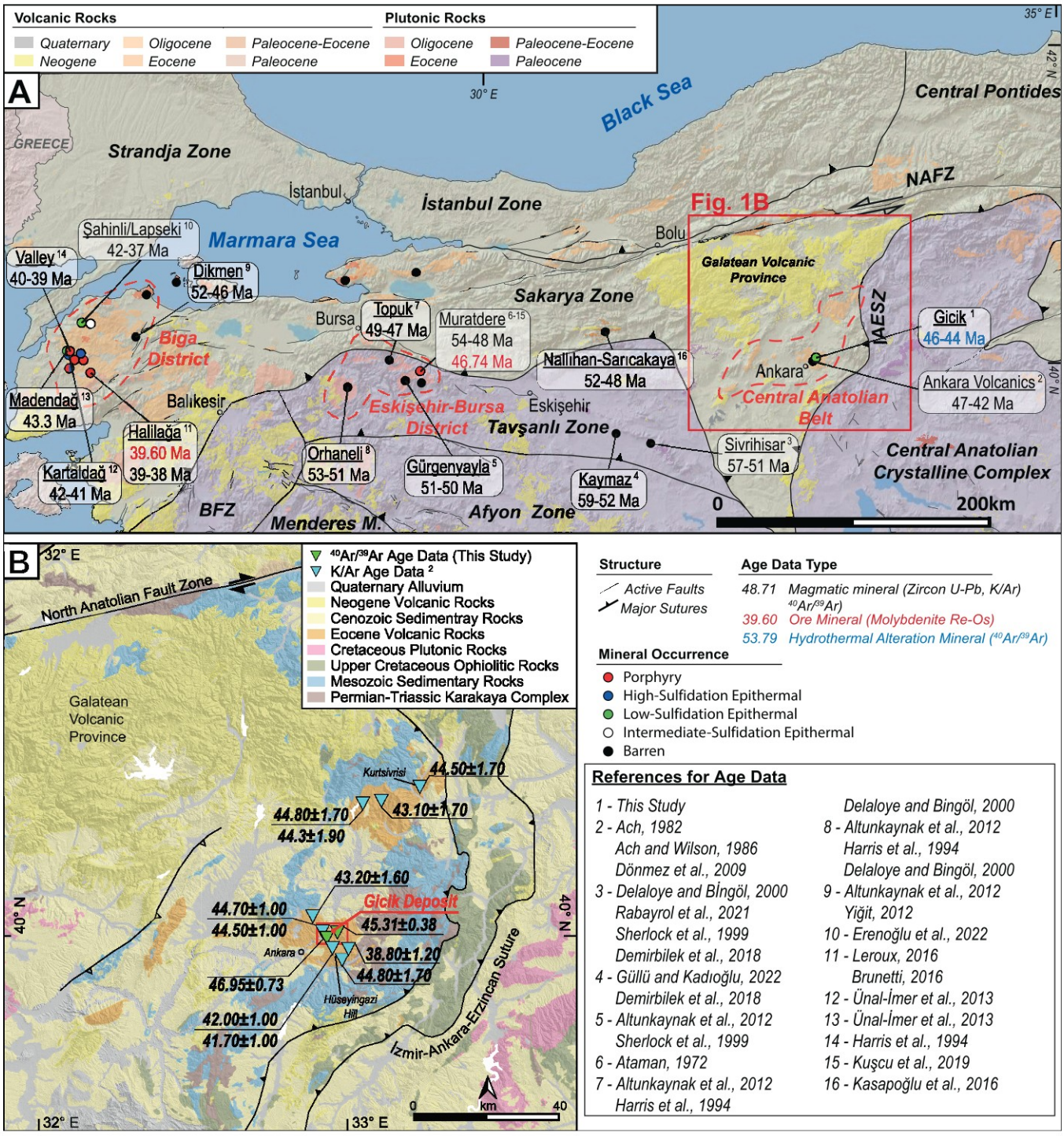


Fig. 1. A) Map of Türkiye showing the distribution of Eocene volcanic and plutonic rocks. Also shown are the location of major porphyry-epithermal deposits and radiometric ages of host rocks and hydrothermal alteration minerals. Major tectonic divisions are from Okay and Tüysüz, 1999, Moix et al., 2008. B) Geological setting of north central Anatolia (Structural features are from Gülyüz et al., 2019). Abbreviations: IZ-Istanbul Zone, CACC-Central Anatolian Crystalline Complex, BFZ-Bornova Flysch Zone, NAFZ-North Anatolian Fault Zone.

kaolinite-illite) and these alteration styles were produced by low-temperature (mostly < 200°C) aqueous fluids.

The widespread volcanic and plutonic rocks found along the collided margin between the Pontides and the Kırşehir Massif in north central Anatolia recorded a prolonged magmatic history from transition from Late Cretaceous subduction-related to Eocene and younger post-subductional tectonism. Several differing interpretations have been provided to explain the formation of the volcanic units also hosting the Gicik mineralization in north Ankara. Some authors claimed that these volcanic rocks represent the eastward extension of the post-collisional Miocene Galatean Volcanic Province (e.g., Akyürek et al., 1984; Tankut, 1985), whereas others have argued that volcanism in north Ankara occurred during the Eocene, and was related to ongoing Neotethyan subduction (Ach, 1982; Dönmez et al., 2009). Eocene magmatism elsewhere along the belt is often attributed to break-off of the northern Neotethyan slab (Altunkaynak, 2007; Dilek and Altunkaynak, 2009; Karslı et al., 2011), but a recent study by Mueller et al. (2019) linked this magmatic episode to partial melting of the underthrusted lower crust during advanced stages of collision. These competing models and a lack of geochronological data on timing of hydrothermal activity at Gicik introduced uncertainties regarding its geological setting within a complex collisional belt. The present study aims to resolve these ambiguities by reporting new geochemical and geochronological data from the least-altered and altered igneous lithologies from Gicik. We also provide a detailed framework on the geology and structure of the Gicik deposit as well as on the alteration and mineralization characteristics of the epithermal-style Au-Ag ± Te veins to build on the preliminary findings of Besbelli and Varol (2002).

2. Geological setting

2.1. Geology of the Sakarya Zone

The Gicik epithermal mineralization is preserved in a volcanic-volcaniclastic sequence (Fig. 1B, 2 and 3) emplaced along a convergent plate margin dominated by collisional tectonics since the Late Mesozoic. Here, the basement units of the Sakarya Zone of Laurasian affinity have been juxtaposed against the southerly Kırşehir Massif along the ophiolitic belt of the İzmir-Ankara-Erzincan Suture Zone (İAESZ). The Sakarya Zone, together with the İstanbul and Rhodope-Strandja Zones, make up the extensive Pontide fragment comprising the entire northern Türkiye. It consists of Variscan metamorphic basement units (330–310 Ma; Okay et al., 2006) and cross-cutting Paleozoic granitoids (Delaloye and Bingöl, 2000; Okay et al., 2006).

Until the Late Triassic, the Sakarya Zone remained as a part of the active Laurasian margin to the north of the Paleotethys ocean basin. Paleotethys closure was accompanied by development of subduction-accretion complexes (the Karakaya and Küre complexes) during the Permo-Triassic and Early Jurassic (Pickett and Robertson, 1996; Okay and Göncüoğlu, 2004; Okay et al., 2006). Opening of the marginal Küre Ocean in the Late Triassic resulted in the rifting of Sakarya Zone off of Laurasia (Ustaömer and Robertson, 1994), but the Sakarya Zone and other Pontic fragments re-accreted to the Laurasian margin in the Early Jurassic following the closure of Küre Ocean due to subduction beneath the Sakarya Zone (Ustaömer and Robertson, 1994; Okay and Nikishin, 2015; Aygül et al., 2016). This initiated opening of the İzmir-Ankara-Erzincan Ocean (northern Neotethys) to the south of these fragments due to northward roll-back of subducting slab (Okay and Tüysüz, 1999; Moix et al., 2008). By this time, the Anatolide-Tauride Block (ATB) and the Kırşehir Block already occupied the north-facing southern margin of the İzmir-Ankara-Erzincan Ocean.

Closure of the northern Neotethys basin occurred in the Cretaceous, leading to development of arc complexes mainly in the eastern Pontides (Okay and Şahintürk, 1997; Rice et al., 2006; Sipahi et al., 2018), and less commonly around Biga and Thrace regions (e.g. Şevketiye pluton; Delaloye and Bingöl, 2000; Rice et al., 2006) as well as in central Pontides (e.g. Beypazarı Granitoid; Helvacı et al., 2014; Berber et al., 2021; Sayit et al., 2022). Continent-continent collision between the Sakarya Zone and the Kırşehir Block occurred in the Late Cretaceous (Kaymakçı, et al., 2003; Rice et al., 2006; Kaymakcı et al., 2009). The Late Cretaceous collision is generally regarded as a "soft collision", followed by ultimate "hard collision" likely occurred during the late Paleocene–early Eocene (Rice et al., 2006; Kaymakcı et al., 2009). At this time the Kırşehir Block was probably an independent terrane (Okay and Tüysüz, 1999; Nairn et al., 2012), but van Hinsbergen et al. (2016) and Mueller et al. (2019) argued that it was the lateral continuation of the Tavşanlı Zone and both were connected to the ATB during the collision.

Late Cretaceous–Paleocene elimination of the İzmir-Ankara-Erzincan Ocean was followed by two major episodes of magmatism in north central Anatolia. The first of these is represented by middle Eocene volcanic and plutonic rocks that formed in response to Sakarya-ATB collision. Magmatic products of this stage in northern Ankara include calc-alkaline andesitic-dacitic lavas and agglomerates (Fig. 1B; Ankara Volcanics; Ach, 1982; Seyitoğlu and Büyükönal, 1995; Dönmez et al., 2009), monzonitic-granitic plutons near Sivrihisar farther northwest (Fig. 1A; Sherlock et al., 1999; Altunkaynak et al., 2012; Demirbilek et al., 2018), and Sarıcakaya-Nallıhan volcanics towards the west (Fig. 1A; Kasapoğlu et al., 2016; Mueller et al., 2019; Göçmengil et al., 2022). Rocks of similar age and composition are also exposed widely in the eastern Pontides (Topuz et al., 2005; Topuz et al., 2011; Aydınçakır and Şen, 2013), in the Eskişehir-Bursa district (e.g. Gürgenyayla, Tepeldağ, Topuk, and Orhaneli plutons; Fig. 1A; Harris et al., 1994; Yılmaz, 2005; Altunkaynak et al., 2012), and Biga Peninsula (Altunkaynak and Genç, 2008; Altunkaynak et al., 2012. Okay et al., 2022, Aluç et al., 2024). Eocene magmatism is commonly accepted to have developed in response to breaking off of the northward-subducting Neotethyan lithosphere (Altunkaynak, 2007; Keskin et al, 2008; Karslı et al., 2011; Dokuz et al., 2019). However, Mueller et al. (2019), proposed that Eocene volcanism in north-central Anatolia was a product of renewed underthrusting (i.e., continued shortening and collision).

The second stage of magmatism mainly affected the region between the central and western parts of the collisional belt, and is responsible for formation of the prominent Galatean Volcanic Province (GVP) to the northwest of Ankara (Fig. 1B). GVP covers an area of approximately 6500 km^2 and consists primarily of Early–Late Miocene calc-alkaline trachyandesite-andesite to trachydacite-dacite volcanic and volcaniclastic sequences with minor rhyolite (Büyükönal, 1971; Çalgın et al., 1973; Tankut, 1985; Wilson et al., 1997; Tankut et al., 1998; Yürür et al, 2002; Varol et al., 2007, 2008). GVP is developed around several main volcanic eruption centers during post-collisional crustal extension following subduction of the northern Neotethys (Varol et al., 2014).

Volcanic complexes exposed to the north of Ankara ("Ankara Volcanics" of Ach, 1982 and "Tekke Volcanics" of Akyürek et al., 1984) are commonly regarded as the eastern extension of the Miocene GVP (Akyürek et al., 1984; Tankut, 1985; Besbelli and Varol, 2002), as also shown in the regional maps by General Directorate of Mineral Research and Exploration of Türkiye (MTA). These include some of the notable eruptive centers in Hüseyingazi (located 4–5 km to the south of Gicik), Elmadağ, Çubuk, and Sincan. However, published K-Ar ages of 47 and 42 Ma from Gicik, Hüseyingazi, and Kurtsivrisi (Ach, 1982; Ach and Wilson, 1986; Dönmez et al., 2009) indicate that these calc-alkaline volcanic-volcaniclastic sequences are rather associated with Eocene magmatism.

2.2. Mineralization in the Central-Western Sakarya Zone

Magmatic-hydrothermal mineralization related to Eocene magmatic activity occurs in two main regions in central and western parts of the Sakarya Zone. These are the Biga Peninsula and Eskişehir-Bursa District in the west, and the Eastern Pontides in the east (Fig. 1A). A large number of porphyry, epithermal, skarn/CRD-type mineralizations are

associated with volcano-plutonic complexes in these three areas (Fig. 1A).

2.2.1. Biga Peninsula

Cenozoic magmatic activity in Biga Peninsula (Fig. 1A) in NW Türkiye occurred in two main stages: (1) during 49–36 Ma, but mainly peaking between 41 and 36 Ma (Delaloye and Bingöl, 2000; Ustaömer et al., 2009; Altunkaynak et al., 2012), and (2) during 32–22 Ma (Ercan et al., 1995, 1998; Aldanmaz et al., 2000; Altunkaynak and Genç, 2008; Akal, 2013). Both post-collisional stages have seen production of magmas with broadly similar chemistry represented by calc-alkaline medium- to high-K, felsic to intermediate composition volcanic and plutonic rocks until the late Miocene.

Base and precious metal mineralization in the Biga Peninsula is temporally and spatially related to these Eocene–Miocene magmatic rocks, but deposits of Eocene age are relatively less common in part due to the extensive cover of younger volcanic and sedimentary rocks. Major Eocene systems include the Halilağa Cu-Au deposit (39.6 Ma molybdenite Re-Os, and 39.4–37.8 Ma zircon U-Pb ages; Brunetti, 2016; Kuşcu et al., 2019), the most significant porphyry discovery in the Peninsula to date, the > 1 Moz Lapseki low-sulfidation epithermal Au deposit (37.3 Ma K-Ar age; Ercan et al., 1998; Yılmaz et al., 2010; Gülyüz et al., 2020; Dilekler, 2022), the highly prospective TV Tower district containing the Camelback and Valley porphyry Cu-Au, Karaayı, Kuşçayırı, and Kartaldağ high-sulfidation (Ünal-İmer et al., 2013; Leroux, 2016; Smith et al., 2016; Sánchez et al., 2016; Kuşcu et al., 2019), and Madendağ low-sulfidation epithermal Au-Ag ± Cu deposits (Ünal-İmer et al., 2013; Fig. 1A).

2.2.2. Eskişehir-Bursa district

The Eskişehir-Bursa District (EBD; Fig. 1A) is the eastern extension of the Cenozoic magmatic belt in Biga, but unlike the latter its western part adjacent to Biga Peninsula primarily contains calc-alkaline, medium-K plutonic rocks and their volcanic counterparts. Towards east, however, volcanic products dominate, particularly between Eskişehir and Nallıhan, and Eocene granitoids are localized along two separate corridors aligned parallel to the İAESZ. The northern corridor includes the dioritic to granitic rocks of Armutlu, Kapıdağ (45.3–36.0 Ma; Delaloye and Bingöl, 2000; Altunkaynak et al., 2012), and Karabiga plutons (47.0–44.4 Ma; Delaloye and Bingöl, 2000; Altunkaynak et al., 2012), whereas Orhaneli (57.9–50.5 Ma; Harris et al., 1994; Delaloye and Bingöl, 2000; Altunkaynak et al., 2012), Topuk (~48.8 Ma; Kuşcu et al., 2019), Gürgenyayla (~49.9 Ma; Kuşcu et al., 2019), Tepeldağ (~45.0 Ma; Okay and Satır, 2006; Altunkaynak et al., 2012), and Sivrihisar plutons (55.2–53.0 Ma; Sherlock et al., 1999; Rabayrol et al., 2021) are exposed in the south and southeast (Altunkaynak et al., 2012; Fig. 1A).

Several intrusion-related mineralizations occur within the EBD, but most of these seem to be sub-economic with the sole exception of Kaymaz (Fig. 1A), where gold mineralization is controlled by a major shear zone developed between listwaenites and ~ 53 Ma-old granitoids (Sherlock et al., 1999; Yavuz et al., 2022). Other significant systems include the Muratdere, Sarıçayıryayla, Gelemiç, Tüfekçikonak, Mayıslar, and Topukdere porphyry Cu ± Mo ± Re prospects, and the Demirtepe Cu skarn prospect (Parlak, 2016; McFall et al., 2019; Kuşcu et al., 2019; Zürcher et al., 2019; Rabayrol et al., 2021).

3. Sampling and methods

This study was carried out during 2018–2020 and included fieldwork followed by laboratory studies. Studied area lies immediately outside the bounds of the Ankara city center enabling easy access to the vein exposures.

3.1. Fieldwork

Fieldwork was carried out in Gicik during 2018–2019. Lithological and alteration mapping was conducted at a scale of 1:5000. Existing Eurogold geological maps were used as base maps. Structural measurements were collected from fault surfaces, dikes, and veins for kinematic analysis. Least-altered and altered rock samples representing various lithologies at Gicik were collected from igneous outcrops that have not undergone significant hydrothermal alteration and surface weathering. Systematic sampling along traverses normal to the veins was also completed.

3.2. Mineralogic and petrographic studies

A total of 66 polished thin sections prepared from both least-altered and altered ± mineralized igneous rocks as well as from vein samples were investigated using transmitted and reflected light polarizing microscopes with an aim to highlight host rock mineralogy, ore and gangue mineral assemblages, ore textures, and alteration mineralogy.

Following petrographic work, nineteen altered rock samples were selected for X-ray diffractometry (XRD) analysis for detailed characterization of alteration assemblages. Particular focus was on clay minerals, which could not be identified accurately through petrography. Clay identification was achieved on fine fractions what were air-dried at room temperature, saturated with ethylene glycol, and heated sequentially to 300°C and 550°C. Sample preparation was carried out at the Geological Engineering Department at Middle East Technical University (METU), and XRD analyses were completed at the MTA in Ankara.

3.3. Whole-rock geochemistry

Nine samples selected from a suite of least-altered and altered igneous rocks including lava flows, agglomerates, and dikes were analyzed for determination of their major, minor, and trace element compositions. Eight of these samples were collected from the volcanic-volcaniclastic sequence at Gicik and one sample was obtained from volcanic rock exposures from several km to the west of Gicik. Lithogeochemical analyses were performed at Actlabs (Ontario, Canada) and at ALS Laboratories (Türkiye) with a combination of inductively-coupled plasma (ICP), inductively-coupled plasma emission mass spectrometry (ICP-MS), and instrumental neutron activation analysis (INAA) methods. Accuracy for major elements is typically within 5 relative percent and for trace elements within 10 relative percent, as indicated by replicate analyses of certified standards.

3.4. Electron probe micro analyses (EPMA) and scanning electron microscopy (SEM)

The compositions of primary silicate and oxide minerals in least-altered volcanic rocks as well as compositions of sulfide, sulfosalt, and telluride minerals in mineralized veins were determined through wavelength dispersive spectrometry (WDS) using a JEOL JXA-8230 electron microprobe at the Central Laboratories at METU. Operating conditions were 20 kV accelerating voltage, 20nA beam current and 5 μm beam diameter. Selected natural and synthetic standards for the analyses are as follows: Cu-metal (Cu), PbS (Pb), ZnS (Zn, S), hematite (Fe), Au-metal (Au), InAs (As), Sb-metal (Sb), HgS (Hg), Co-metal (Co), Bi-metal (Bi), CdS (Cd), Se-metal (Se), InTe (Te), Mo-metal (Mo), wollastonite (Si, Ca), Al_2O_3 (Al), orthoclase (K), TiO_2 (Ti), rhodonite (Mn), MgO (Mg), albite (Na), Cr_2O_3 (Cr), V-metal (V), and Ni-metal (Ni). Raw X-ray intensity data were corrected for matrix effects using the standard correction algorithms provided by the JEOL operating software.

Structural formulae for silicate minerals were calculated from oxide wt.% data using stoichiometric normalization to the appropriate number of oxygens/cations: feldspars were normalized on the basis of 8 oxygens, pyroxenes on 6 oxygens, and amphiboles and micas using standard mineral-specific normalization schemes. Amphibole formulae and site allocations were calculated using the MagMin_PT, and Excel based mineral classification and geothermobarometry software of Gündüz and Asan (2022) which utilizes various published methods. Biotite and feldspar end-member proportions were calculated from cation apfu values. Because H_2O cannot be measured directly by EPMA, oxide totals for hydrous silicates are reported on an anhydrous basis. Representative analyses are provided in the Electronic Supplementary Material, whereas summary statistics (minimum, maximum, average, and standard deviation) are reported in the main text tables.

3.5. $^{40}Ar/^{39}Ar$ geochronology

Two hydrothermally-altered samples containing sericite/illite were selected for $^{40}Ar/^{39}Ar$ geochronological analysis in order to constrain the timing of hydrothermal alteration associated with the Gicik epithermal system. Mineral separation included crushing/sieving of rock samples followed by standard gravimetric and electromagnetic techniques, and then by hand picking to ensure purity of the separates. Separates were irradiated together with neutron flux monitors and compositionally comparable samples at the McMaster Nuclear Reactor, Hamilton, Ontario. Fish Canyon Tuff sanidine (FCs; 28.02 Ma; Renne et al., 1998) was used as the neutron fluence monitor. $^{40}Ar/^{39}Ar$ geochronological analyses were carried out at the Noble Gas Laboratory, Pacific Centre for Isotopic and Geochemical Research, University of British Columbia, Canada, using a Micromass VG5400 mass spectrometer. All data were corrected for system blanks, instrumental sensitivity, mass discrimination, radioactive decay during and after irradiation, and interfering argon isotopes derived from atmospheric contamination and neutron-induced reactions involving Ca, Cl, and K. Age calculations were performed using Isoplot (Ludwig, 2001, 2008). Reported uncertainties are given at the 2σ (95% confidence) level and include all propagated analytical errors except those related to mass spectrometer sensitivity and the assigned age of the flux monitor. Interpretation of the $^{40}Ar/^{39}Ar$ data followed the standard procedures outlined by McFall et al. (2019).

4. Results

4.1. Geology of Gicik

4.1.1. Geology of Gicik

The Gicik Au deposit is situated approximately 15 km north of Ankara city center, and lies adjacent to the densely populated urban center (Fig. 2). Host volcanic lithologies include dacitic lavas, agglomerates, and tuff that are part of a large volcanic system exposed near Pursaklar and Çubuk areas, and also extending both to the northwest and east of Ankara (Fig. 1B). Previous studies by Akyürek et al. (1984) and Besbelli and Varol (2002) considered this volcanic succession as a part of the Miocene GVP (Fig. 1B) based on stratigraphic relationships with locally interbedded sedimentary units.

4.1.2. Gicik volcanics

Regional basement rocks are neither exposed at Gicik nor encountered in exploration drill holes extending down to 170 m. Nevertheless, they are presumed to overlie unconformably the Paleozoic-Mesozoic metamorphic units of the Sakarya Zone based on observations from other localities north of Ankara (Akyürek et al., 1982, 1984). In and around the Gicik tenement, the volcanic succession is well-exposed between a section of the peripheral highway near Pursaklar in the south and the Gicik village in the north (Figs. 2 and 3). Roadcuts along the highway as well as incised valleys particularly provide some of the best outcrops, which helped broad subdivision of the local volcanic stratigraphy into three sequences based on dominant lithological units and macro-textural observations.

The Gicik volcanic sequence starts with the lower volcanic series, which comprises pinkish and yellow-gray, massive dacitic lavas without any significant volcaniclastic input (Fig. 3, 4D, and F). This unit occupies the southern sector of the tenement at relatively lower elevations, and is especially well-exposed along the highway (Fig. 3). Further north, dacitic lavas are overlain by intercalations of agglomerate, tuff, and dacite porphyry of the middle volcanic series (Fig. 2, 4B, and C). This section of the volcanic sequence outcrops widely around the mineralized veins to the south and nearby the Gicik village (Fig. 4C). Agglomerates of the middle volcanic series are gray to beige colored, and consist of rounded to sub-angular dacitic blocks of variable size (from a few centimeters up to 30 cm in diameter) set in a tuffaceous matrix (Fig. 4B).

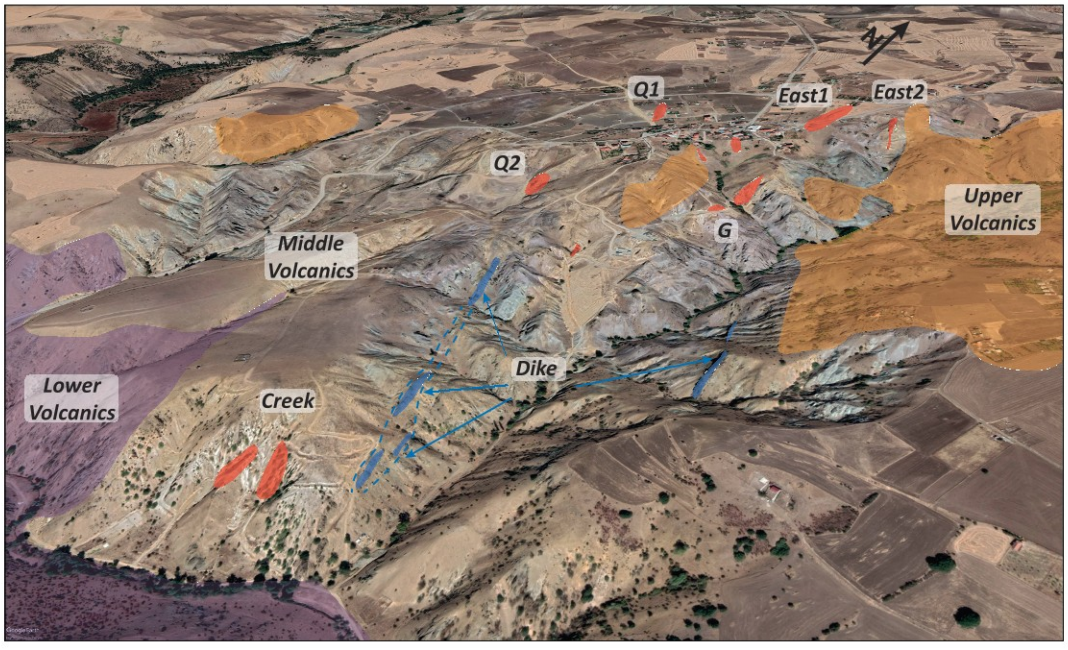


Fig. 2. Google Earth image showing distribution of siliceous veins (in red) and dikes (in blue) at Gicik.

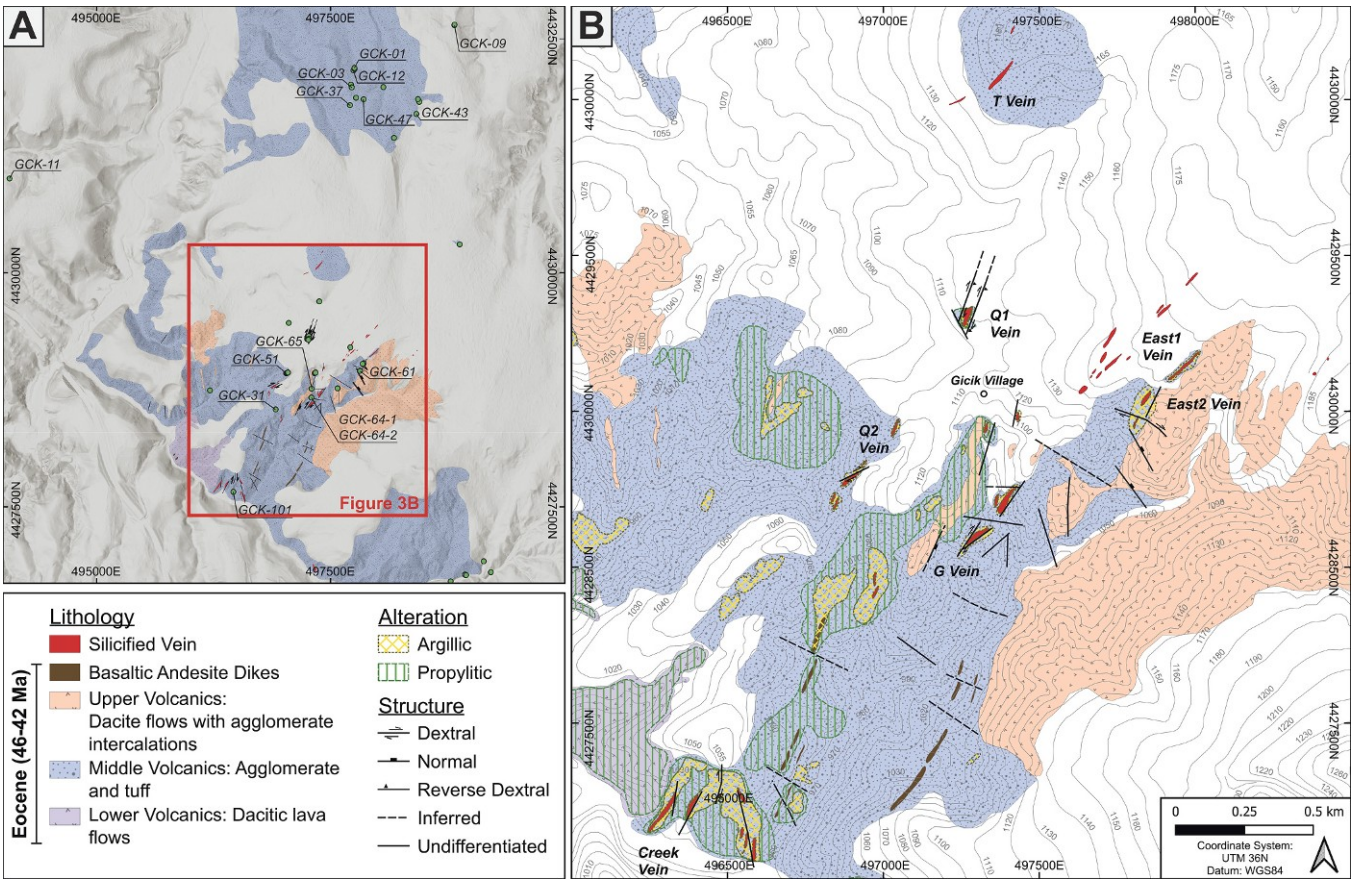


Fig. 3. (A) Geological map of the Gicik area in north Ankara. Sampling locations are also shown. (B) Detailed outcrop geology map of Gicik. Blank areas represent agricultural and recreational fields where there is no exposure.

Dacites typically display porphyritic texture with abundant plagioclase and lesser hornblende, biotite, and quartz phenocrysts (Fig. 5A). Similar fragments were also observed in agglomerates, and consequently these were interpreted to be of juvenile origin derived from the erupting magma. The upper volcanic series crop out in the northern and eastern sectors of the study area (Fig. 4A). This unit is represented by approximately N–S-trending dacite flows with agglomerate intercalations, which cap the underlying lower and middle volcanic series rocks. Agglomerates of the upper volcanic series contain both juvenile and cognate andesitic to dacitic fragments, often with gray to pinkish colors and porphyritic texture (Fig. 4A).

Lower to upper volcanic series rocks have been cut by a number of isolated basaltic andesite dikes that are commonly 5 to 15 m wide (Fig. 4D). Basaltic andesite dikes trend mainly in the NE-SW direction similar to that of the mineralized veins. Dikes are dark colored due to relatively higher abundance of ferromagnesian minerals, and display microphaneritic textures dominated by plagioclase and hornblende.

4.2. Mineralogy of Gicik volcanics

Lavas and agglomerates of the lower, middle, and upper volcanic series are characterized by broadly similar mineral contents. Modal abundances of the main mineral phases also do not show much variation throughout the volcanic sequence. Plagioclase, hornblende, and biotite are ubiquitous in the samples and are the predominant phenocryst phases (Fig. 5A). Quartz is present in smaller amounts, whereas clinopyroxene is scarce (Fig. 5B). These minerals, as well as microphenocrysts of magnetite and ilmenite are set in a fine-grained, partially devitrified matrix in the dacitic volcanic rocks. Representative chemical compositions of primary silicate and oxide minerals are given in Tables 1–4.

Plagioclase generally occurs as large isolated phenocrysts, occasionally as glomerocrysts, and also as microlites within the finer-grained groundmass (Fig. 5B). Phenocrystic plagioclase is often complexly zoned (Fig. 5B) suggesting disequilibrium conditions. These zoned plagioclase phenocrysts also contain abundant melt inclusions. Plagioclase has uniform composition represented by andesine (An_{40}-An_{46}; Fig. 6A; Table 1).

Amphibole is the predominant ferromagnesian mineral phase in dacitic rocks and is present as euhedral to subhedral phenocrysts with minute inclusions of plagioclase and magnetite (Fig. 5C). It is dark brown in color likely due to its high Fe content (Gribble and Hall, 1992). EPMA measurements indicate calcic compositions for amphiboles, which are of magnesio-hornblende variety (Fig. 6B; Table 2). Most phenocrysts have been partially to completely opacitized into Fe-Ti oxides, a feature that has often been attributed to magmatic oxidation or depressurization of magma upon rapid ascent to shallow crustal levels (Rutherford and Hill, 1993; Chambefort et al., 2013).

Biotite is only a minor phenocryst phase compared to amphibole in Gicik volcanic rocks. Biotite crystals have sizes ranging from 300 to 700 μm. Analyzed biotite grains are slightly enriched in TiO_2 (avg.: 4.38 wt %; Table 3) and are phlogopitic in composition (Fig. 6C). Observed TiO_2 enrichments may be an artifact of widespread opacite development particularly along the rims (Fig. 5D).

Magnetite and ilmenite are common microphenocryst phases (usually 30–50 μm in diameter) observed in the least-altered rocks. Isolated crystals of both minerals are present in most samples, whereas in a few samples these two phases occur as exsolutions.

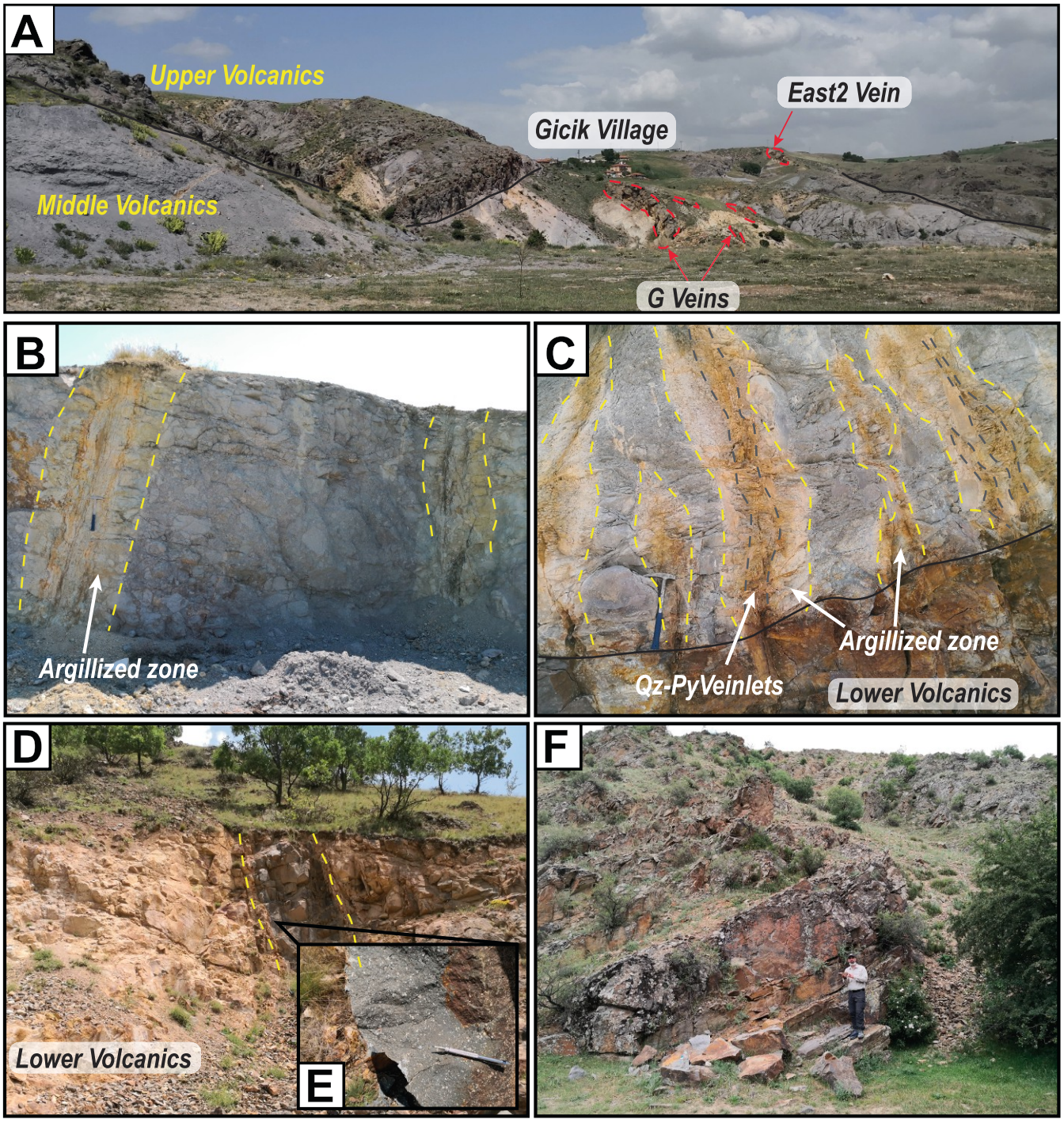


Fig. 4. Field photographs from the main outcrops at Gicik. A) General view of the Gicik volcanic sequence, B) Agglomerate with cm-size andesite clasts showing argillic alteration zones due to thin quartz-pyrite veins C) Contact between the massive lava flows from the lower and agglomerates of the middle volcanics. D) Basaltic andesite dikes cross-cutting the lower volcanics. E) Close-up image of the basaltic andesite dikes. F) Massive lava flows of the lower volcanics.

4.3. Lithogeochemistry

Major and trace element compositions of Gicik volcanic rock samples were evaluated to determine host rock compositions, possible magma source(s), and tectonic setting. Full lithogeochemical data is provided in Table 5. Lithogeochemical data from regional middle Eocene magmatic systems throughout the Sakarya Continent, including those from north central Anatolia, Biga Peninsula, and Eskişehir-Bursa District (EBD) as well as Oligo-Miocene volcanic rocks of the GVP were also plotted for comparison purposes. Major oxide abundances were normalized to 100% volatile-free basis prior to plotting.

All Gicik samples have undergone at least some degree of hydrothermal alteration, and contain secondary minerals. Nevertheless, a distinction was made between least-altered and significantly-altered samples as based on loss-on-ignition (LOI) values, and also as confirmed through petrographic inspection. In the least-altered samples, primary mineral phases are well-preserved including magnetite microphenocrysts, but alteration minerals and sulfides are either absent or are

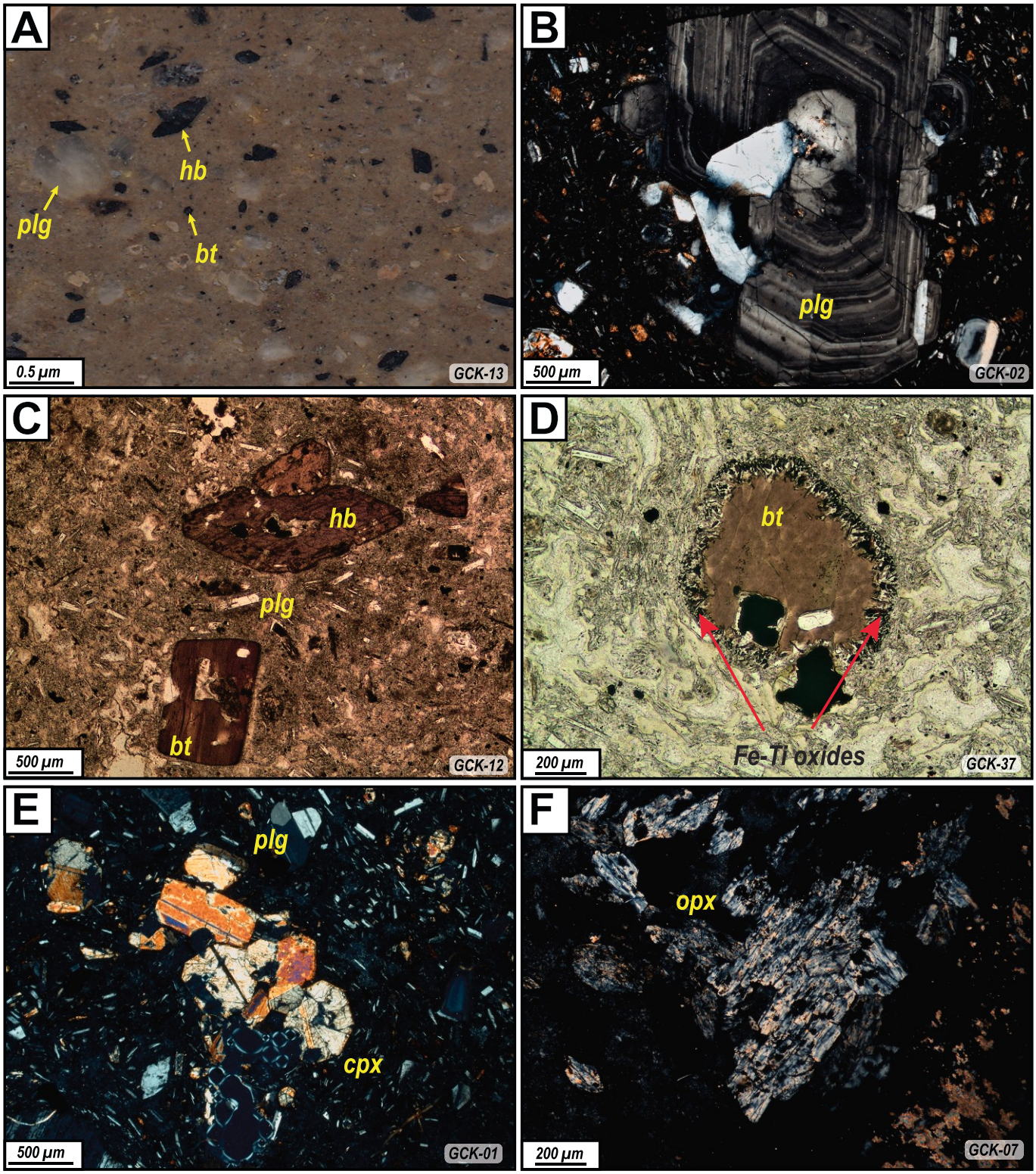


Fig. 5. Close-up image (A) and photomicrographs (B–F) of the Gicik volcanic rock samples. A) Typical porphyritic textures with hornblende, biotite, and plagioclase assemblages observed in dacite, B) Compositionally-zoned plagioclase (plg) phenocrysts in dacitic volcanic rock, C) Euhedral, slightly oxidized phenocrysts of hornblende (hb) and biotite (bt), D) Fe-Ti oxide opacite rims around biotite, E) Clinopyroxene (cpx) and F) Orthopyroxene (opx) clusters displaying glomeroporphyritic texture.

Table 1
Average plagioclase compositions. All values are reported in wt.%.

Composition	GCK-01				GCK-12				GCK-43			
	min	max	avg	std	min	max	avg	std	min	max	avg	std
Na_2O	5.59	6.76	6.22	0.30	4.99	6.54	6.03	0.41	6.64	8.75	7.69	0.64
SiO_2	56.70	60.11	58.49	0.87	54.94	59.55	58.04	1.17	57.18	59.62	58.69	0.97
Al_2O_3	24.97	26.84	25.84	0.53	24.77	28.01	25.85	0.84	25.19	27.49	25.91	0.85
MgO	–	–	–	–	–	–	–	–	–	–	–	–
K_2O	0.31	0.52	0.40	0.05	0.26	1.01	0.44	0.17	0.41	0.46	0.44	0.03
CaO	7.02	9.16	8.00	0.59	7.07	10.39	8.16	0.86	5.95	8.32	7.01	0.84
$FeO_{(t)}$	0.16	0.23	0.21	0.02	0.19	0.30	0.22	0.03	0.12	0.34	0.22	0.07
MnO	–	–	–	–	–	–	–	–	0.00	0.03	0.01	0.01
NiO	–	–	–	–	–	–	–	–	0.00	0.17	0.08	0.06
TiO_2	–	–	–	–	–	–	–	–	–	–	–	–
Cr_2O_3	–	–	–	–	–	–	–	–	0.02	0.07	0.04	0.02
SrO	0.08	0.18	0.13	0.02	0.09	0.16	0.13	0.02	–	–	–	–
BaO	0.00	0.09	0.04	0.02	0.00	0.13	0.04	0.04	–	–	–	–
Total	98.81	100.03	99.34	0.25	98.45	99.34	98.91	0.26	99.70	99.95	99.82	0.09
Si	10.37	10.81	10.61	0.13	10.05	10.82	10.58	0.20	10.25	10.65	10.47	0.15
Ab	51.44	61.57	57.02	2.67	45.76	60.71	55.67	3.80	59.09	71.09	65.73	3.86
An	35.55	46.58	40.54	2.96	36.27	52.66	41.66	4.30	26.71	40.91	33.24	4.72
Or	1.88	3.07	2.44	0.32	1.58	6.12	2.67	1.02	0.00	2.57	1.03	1.29

Table 2
Average amphibole compositions. All values are reported in wt.%.

Composition	GCK-01				GCK-12				GCK-43			
	min	max	avg	std	min	max	avg	std	min	max	avg	std
Na_2O	1.04	1.63	1.32	0.17	0.89	1.54	1.25	0.16	1.16	1.39	1.30	0.08
SiO_2	47.05	50.86	49.32	1.12	44.94	49.76	48.26	0.98	48.29	51.21	50.07	1.06
Al_2O_3	5.67	7.44	6.64	0.44	4.94	8.68	6.50	0.74	5.81	6.72	6.36	0.28
MgO	14.89	17.68	16.35	0.77	13.89	17.43	16.08	0.97	16.53	17.53	17.01	0.34
K_2O	0.30	0.42	0.36	0.04	0.27	0.55	0.36	0.07	–	–	–	–
CaO	10.15	11.29	10.67	0.30	10.23	13.22	10.88	0.61	10.11	10.56	10.35	0.16
$FeO_{(t)}$	10.33	12.34	11.35	0.58	9.14	13.18	11.31	0.82	10.31	11.15	10.75	0.28
MnO	0.36	0.52	0.42	0.05	0.34	0.45	0.41	0.04	0.43	0.51	0.47	0.03
NiO	0.00	0.41	0.11	0.11	0.00	0.04	0.02	0.01	0.07	0.23	0.15	0.05
TiO_2	1.03	1.42	1.21	0.10	0.93	1.67	1.21	0.18	1.02	1.26	1.11	0.08
Cr_2O_3	0.01	0.09	0.03	0.03	0.01	0.10	0.03	0.03	0.01	0.07	0.04	0.02
Total	94.78	98.99	98.35	0.86	95.34	98.95	97.05	1.10	94.64	98.83	97.59	1.79
Si	6.88	7.17	7.06	0.08	6.66	7.22	7.01	0.11	7.04	7.22	7.13	0.05
Al^{IV}	0.83	1.14	0.95	0.08	0.80	1.36	1.01	0.12	0.79	0.99	0.88	0.06
Al^{VI}	0.10	0.25	0.17	0.05	0.00	0.18	0.11	0.04	0.10	0.26	0.18	0.06
Fe^{3+}	0.46	0.58	0.51	0.03	0.27	0.52	0.46	0.05	0.50	0.57	0.53	0.02
Fe^{2+}	0.67	0.99	0.85	0.09	0.81	1.11	0.91	0.08	0.68	0.79	0.75	0.04
OH	1.69	1.87	1.78	0.06	1.71	2.00	1.82	0.08	1.72	1.85	1.77	0.05
P (MPa)	99.8	158.4	129.8	15.6	84.4	183.3	118.7	19.7	114.9	137.3	129.5	6.8
T (°C)	784.0	862.7	828.1	23.8	766.9	847.6	805.3	16.1	827.9	847.6	837.8	6.9
ΔFMQ	0.89	3.15	1.94	0.49	1.30	3.49	2.35	0.72	2.02	3.06	2.47	0.34
$\log fO_2$	−12.96	−10.54	−12.26	0.62	−13.39	−11.05	−12.32	0.75	−11.94	−11.13	−11.53	0.27
H_2O_{melt} (%)	4.02	5.13	4.64	0.28	4.61	8.04	5.50	0.88	4.37	4.89	4.60	0.18

present in low amounts. During geochemical evaluation, altered samples with elevated LOI values were treated with caution. Accordingly, petrogenetic interpretations were based mainly on relatively immobile elements and overall trace-element patterns. Broadly identical trace element compositions of altered and least-altered samples suggest that trace element systematics of altered samples were not significantly modified through hydrothermal alteration.

4.3.1. Major elements

Samples from lower, middle, and upper volcanic series are metaluminous to slightly peraluminous (Fig. 7C), medium-K calc-alkaline (Fig. 7B) dacites with SiO_2 contents ranging between 61.9 and 70.2 wt% (Table 5). A post-mineralization dike sample (sample GCK-101) represents a high-K calc-alkaline basaltic andesite with 53.5 wt% SiO_2 (Table 5). Major element abundances of Gicik samples and other regional Eocene plutonic/volcanic rocks from north of Ankara were plotted against SiO_2 (Fig. 7).

4.3.2. Trace elements

On a primitive-normalized trace element diagram, incompatible elements mainly including large-ion lithophile elements (LILE) such as K, Rb, Cs, Sr, and Ba show relative enrichments in all samples (Fig. 8A). Negative anomalies for high field strength elements (HFSE) such as Ta, Nb, and Ti suggest derivation from subduction-related magmas (Gill, 1981; Brenan et al., 1994). Relative depletions observed in Ti and P (Fig. 8A), on the other hand, were interpreted to reflect fractionation of magnetite, Fe-Ti oxides, amphibole, and apatite. Contrary to the rest of the samples, the basaltic andesite dike sample does not display any negative Ti and P anomalies, while retaining negative Ta and Nb anomalies (Fig. 8A).

On the chondrite-normalized rare earth element diagram (Fig. 8B), samples of lower, middle, and upper volcanic series are moderately enriched in light rare earth elements (LREE) compared to medium (MREE) and heavy rare earth elements (HREE). The weak listric pattern these samples display, with relatively steep slopes from LREE to MREE

Table 3
Average biotite compositions. All values are reported in wt.%.

Composition	GCK-01				GCK-12			
	min	max	avg	std	min	max	avg	std
Na_2O	0.47	1.11	0.87	0.21	0.94	0.94	0.94	–
SiO_2	37.70	40.21	39.34	0.93	37.55	37.55	37.55	–
Al_2O_3	13.86	15.03	14.63	0.42	14.56	14.56	14.56	–
MgO	13.77	17.67	16.51	1.25	16.26	16.26	16.26	–
K_2O	8.27	8.81	8.48	0.15	8.58	8.58	8.58	–
CaO	0.02	0.05	0.04	0.02	–	–	–	–
$FeO_{(t)}$	12.27	14.57	12.95	0.81	14.01	14.01	14.01	–
MnO	0.13	0.25	0.17	0.04	–	–	–	–
NiO	0.00	0.35	0.15	0.12	–	–	–	–
TiO_2	4.14	4.50	4.38	0.12	4.57	4.57	4.57	–
Cr_2O_3	0.04	0.12	0.06	0.03	–	–	–	–
Total	98.01	98.94	98.42	0.26	96.47	96.47	96.47	–
Si	2.86	2.91	2.88	0.02	2.80	2.80	2.80	–
Al^{IV}	1.77	1.86	1.82	0.03	1.99	1.99	1.99	–
Al^{VI}	0.82	0.97	0.89	0.05	0.75	0.75	0.75	–
Fe_2O_3	3.95	6.66	5.61	0.81	5.61	5.61	5.61	–
FeO	6.41	11.02	7.90	1.45	8.96	8.96	8.96	–
H_2O	3.67	3.89	3.82	0.09	3.75	3.75	3.75	–
Fe#	0.28	0.37	0.31	0.03	0.33	0.33	0.33	–
Mg#	0.63	0.72	0.69	0.03	0.67	0.67	0.67	–
$X_{phlogopite}$	0.57	0.66	0.63	0.03	0.62	0.62	0.62	–
$X_{siderophyllite}$	0.14	0.18	0.15	0.01	0.18	0.18	0.18	–
X_{annite}	0.20	0.25	0.22	0.02	0.21	0.21	0.21	–

Table 4
Average pyroxene compositions. All values are reported in wt.%.

Composition	GCK-01				GCK-43			
	min	max	avg	std	min	max	avg	std
Na_2O	–	–	–	–	–	–	–	–
SiO_2	46.23	53.54	52.09	1.33	54.17	55.11	54.56	0.34
Al_2O_3	2.08	8.68	3.29	1.25	1.63	2.59	2.11	0.48
MgO	10.99	18.23	16.45	1.27	29.50	31.55	30.36	0.76
K_2O	–	–	–	–	–	–	–	–
CaO	18.39	21.49	19.36	0.59	1.14	1.34	1.22	0.08
$FeO_{(t)}$	5.24	9.89	6.87	0.91	7.89	10.78	9.82	1.06
MnO	0.10	0.33	0.22	0.06	0.20	0.38	0.28	0.06
NiO	0.08	0.43	0.21	0.07	0.17	0.35	0.23	0.07
TiO_2	–	–	–	–	0.19	0.20	0.20	0.01
Cr_2O_3	0.03	1.51	0.23	0.27	0.22	0.35	0.28	0.05
Total	94.21	99.24	98.03	1.57	97.34	98.54	97.86	0.49
Si	1.75	2.04	1.96	0.05	1.93	1.99	1.96	0.02
Al^{IV}	0.00	0.25	0.05	0.05	0.00	0.07	0.03	0.03
Al^{VI}	0.06	0.14	0.08	0.02	0.03	0.04	0.03	0.00
$Fe_T/(Fe_T + Mg)$	0.14	0.34	0.19	0.03	0.12	0.17	0.15	0.02
$Fe^{2+}/(Fe^{2+}+Mg)$	0.14	0.29	0.19	0.03	0.11	0.17	0.15	0.02
Wo	38.08	48.29	40.69	1.71	2.20	2.64	2.39	0.16
En	34.36	52.20	48.03	3.11	80.96	85.74	82.62	1.77
Fs	8.56	17.35	11.28	1.64	12.03	16.44	14.99	1.64

and flattening between MREE to HREE is explained by hornblende ± titanite fractionation and by compatibility of HREE with zircon as well as with other mafic silicate mineral phases (Green and Pearson, 1985; Sisson, 1994; Bachmann et al., 2005; Prowatke and Klemme, 2006). The basaltic andesite dike sample is slightly more enriched (up to ~ 1.5 times) in most REEs compared to other Gicik samples (Fig. 9B), and is also characterized by a relatively steeper down-sloping pattern from LREE to HREE (Fig. 9B).

All Gicik samples, including the basaltic andesite dike sample, lack significant Eu anomalies as shown on the chondrite-normalized REE plot (Fig. 8B) and as also suggested by Eu_N/Eu^* ratios that vary between 0.91 and 1.02 (avg. 0.97, n = 9; Fig. 9A). This is indicative of suppression of early plagioclase fractionation possibly due to high magmatic water contents and/or magma oxidation states (Frey et al., 1978; Hanson, 1980). Most samples are moderately-enriched in LREE ($[La/Sm]_n$ = 4.96–6.61, avg. 5.56; Fig. 9B), but are only weakly-enriched in MREE with respect to HREE ($[Dy/Yb]_n$ = 1.00–1.16, avg. 1.08; Fig. 9B) suggesting the role of hornblende fractionation in the melt source. The basaltic andesite dike sample is distinguished from other samples with its relatively lower $[La/Sm]_n$ and higher $[Dy/Yb]_n$ (Fig. 9B).

In the Sr/Y vs. Y diagram, Gicik volcanics plot within the adakitic range (Fig. 9C), but they straddle the boundary between the adakite and normal andesite-dacite-rhyolite fields in a plot of La/Yb vs. Y diagram (Fig. 9D). No clear fractionation trends are discernible in Sr/Y and La/Yb ratios with increasing SiO_2 due to Gicik samples having a quite restricted range of SiO_2 concentrations, although Sr/Y values appear to display a roughly decreasing trend within the adakitic range (Fig. 9E and F).

4.4. Estimates of magma crystallization conditions

Hornblende chemistry is used to estimate pressure and temperature conditions during crystallization as well as melt f_{O_2} and water contents based on experimental calculations of Ridolfi et al. (2010). Estimated hornblende crystallization temperatures are in the range of 767–863 ±

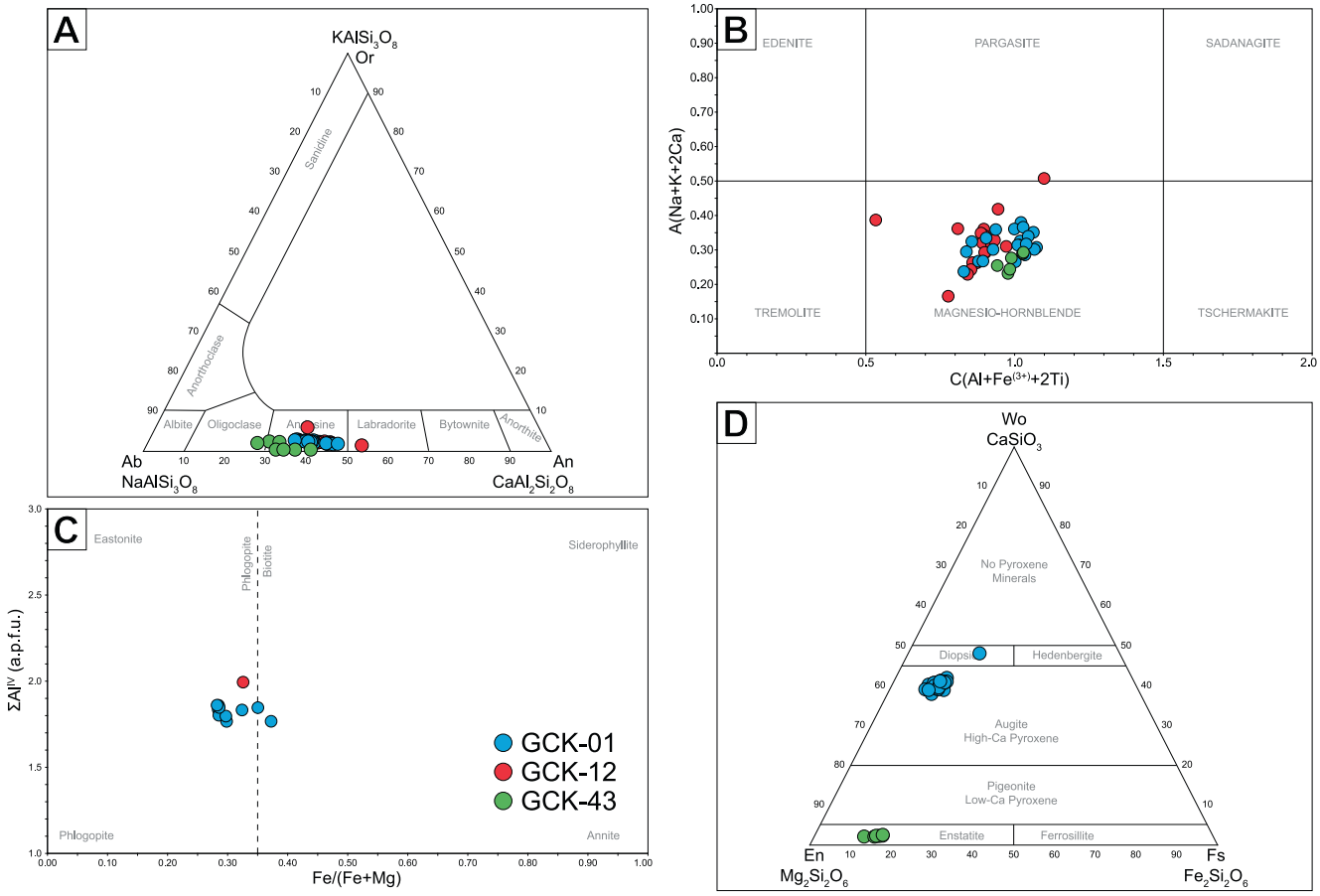


Fig. 6. Classification of A) Plagioclase (Deer et al., 1997), B) Amphibole (Hawthorne et al., 2012), C) Biotite (Deer et al., 1992), and D) Pyroxenes (Morimoto et al., 1988) in Gicik volcanic rocks based on EPMA data.

23°C (avg. = 820°C, n = 48; Fig. 10A) and pressures vary between 0.08–0.18 ± 0.02 GPa (avg. = 0.13 GPa, n = 48; Fig.10C). Oxygen fugacity values calculated using hornblende chemistry vary between + 0.89 and + 3.49 ± 0.62 (avg. = 2.19, n = 48; Fig. 10B) with respect to the fayalite-quartz-magnetite buffer (Fig. 10B). Calculated H_2O_{melt} contents, on the other hand, range between 4.02 and 8.04 ± 0.74 wt% (avg. = 4.99 wt%, n = 48; Fig. 10A). These considerably high magma fO_2 conditions and water contents are in keeping with the widespread occurrence of hornblende and biotite phenocrysts as well as magnetite microphenocrysts in Gicik volcanic rocks, respectively.

4.5. Hydrothermal alteration

The Gicik Au mineralization is generally limited to narrow vein segments in a restricted area near the town of Gicik, but hydrothermal system has a fairly large alteration footprint (>10 km^2) affecting most of the volcanic lithologies and has been partly concealed by the nearby settlements of the Gicik village as well as by agricultural and recreational fields. Mineralized veins are best exposed in the southern part of the Gicik village.

Three main alteration styles were identified in the close proximity of veins as well as in the broader area to the north of Ankara. From distal to proximal with respect to the mineralized veins these alteration types are propylitization, argillic alteration, and silicification (Fig. 3).

Propylitic alteration: Propylitic alteration is the most widespread alteration in Gicik and has also developed regionally, affecting most outcropping volcanic and volcaniclastic rocks north of Ankara to some extent. The lithological units of lower, middle, and upper volcanic series as well as cross-cutting basaltic andesite dikes show variable degrees of propylitic alteration (Fig. 11A). The intensity of propylitic alteration, however, increases significantly in the vicinity of mineralized veins, where it envelopes vein-proximal argillic alteration and silicification. In the propylitized rocks, ferro-magnesian minerals including hornblende, pyroxene, and biotite have been mainly replaced by chlorite and actinolite, whereas epidote and carbonate developed after plagioclase and occur predominantly in the groundmass alongside minor disseminated pyrite (Fig. 11B).

Argillic alteration: Pervasive argillic alteration is developed throughout the volcanic and volcaniclastic wall-rocks adjacent to the siliceous veins. It is particularly well observed in the central and southern parts of the study area, where mineralized veins are abundant (Fig. 3). This alteration style imparted a distinct light gray to beige color to the volcanic rocks with fracture planes coated with brown Fe-(hydr) oxide phases due to surface oxidation of Fe-sulfides, particularly of pyrite (Fig. 4B and C). Argillic alteration is characterized by partial to complete replacement of primary igneous minerals by quartz and clays with local sericite (Fig. 11C). Quartz-clay/sericite initially replaced the matrix or fine-grained groundmass, and with increasing degree of alteration first plagioclase and then hornblende and biotite were altered into clay/sericite assemblages. Pyrite disseminations were weakly developed, whereas rutile is significantly more abundant and developed as fine, needle-like aggregates after ferro-magnesian silicates and also possibly after magnetite and/or ilmenite. A comparison of XRD analyses of samples collected along transects vertical to the mineralized veins showed no significant variation in the clay mineral assemblage, though alteration intensity changes rapidly within a few meters around the veins. The clay assemblage is uniformly comprised by kaolinite, illite, and minor smectite. Carbonate is also present, but in minor quantities in

Table 5
Whole-rock lithogeochemistry data for the Gicik volcanic rocks.

Sample	GCK-01	GCK-03	GCK-09	GCK-11	GCK-31	GCK-37	GCK-47	CAV-03	GCK-101
Easting	497,756	497,727	498,824	493,889	496,914	497,708	497,854	496,839	496,462
Northing	4,432,189	4,431,981	4,432,646	4,429,698	4,428,540	4,431,791	4,431,854	4,421,764	4,427,659
Description	Gicik Altered	Gicik Altered	Gicik	Gicik	Gicik Altered	Gicik Altered	Gicik Altered	Gicik Regional	Gicik Dike
Rock Type	Dacite	Dacite	Dacite	Dacite	Dacite	Dacite	Dacite	Dacite	Basaltic Andesite
SiO_2	62.27	64.14	70.18	65.46	63.59	62.72	61.91	65.64	53.45
TiO_2	0.70	0.63	0.58	0.81	0.72	0.66	0.69	0.69	1.52
Al_2O_3	15.35	14.28	15.02	16.37	15.65	15.14	16.08	15.46	16.68
Fe_2O_3	4.47	3.66	3.45	4.39	4.09	4.08	3.98	4.03	7.47
MnO	0.06	0.07	0.04	0.04	0.06	0.05	0.07	0.06	0.11
MgO	1.37	1.72	0.37	0.63	1.62	2.18	2.53	1.40	4.14
CaO	6.00	5.53	3.32	4.27	4.45	5.60	5.93	3.94	6.12
Na_2O	3.36	2.99	3.62	3.80	3.50	2.99	3.18	3.90	3.15
K_2O	1.38	2.44	2.65	2.60	2.07	1.28	1.07	2.46	2.30
P_2O_5	0.21	0.20	0.17	0.22	0.19	0.20	0.21	0.19	0.48
LOI	4.31	4.66	1.07	2.14	4.16	4.11	4.31	1.90	5.56
Total	99.49	100.30	100.50	100.70	100.30	99.20	100.15	99.82	101.25
Sc	9.75	8.05	5.15	8.65	6.00	7.00	9.00	8.00	7.10
Cr	89.50	86.00	21.50	41.00	20.00	70.00	70.00	40.00	17.00
V	66.00	77.00	42.00	80.00	43.00	102.00	104.00	103.00	188.00
Ni	40.00	40.00	14.00	19.00	19.00	38.00	43.00	16.00	16.00
Co	9.70	10.70	5.70	10.20	10.00	13.00	12.00	10.00	22.00
Cu	17.00	29.00	17.00	14.00	6.00	13.00	20.00	8.00	26.00
Zn	39.00	48.00	28.00	51.00	40.00	59.00	52.00	43.00	75.00
Ga	16.00	16.00	15.00	18.00	15.60	16.20	17.20	18.10	18.00
Rb	37.00	51.00	64.00	63.00	38.50	69.80	76.50	80.90	62.60
Sr	627.00	431.00	358.00	435.00	513.00	583.00	696.00	414.00	643.00
Y	12.00	12.00	10.00	13.00	13.70	12.80	14.00	16.50	18.90
Zr	144.00	127.00	133.00	143.00	133.00	146.00	146.00	169.00	175.00
Nb	12.40	10.50	12.10	16.10	13.50	13.50	14.30	19.80	24.30
Cs	10.30	4.40	1.30	2.50	1.51	31.30	22.90	4.18	20.40
Ba	923.00	606.00	567.00	488.00	581.00	544.00	568.00	509.00	776.00
La	27.30	24.80	24.90	26.60	22.40	24.90	27.10	29.70	29.10
Ce	46.50	42.00	41.30	45.10	37.60	43.20	46.10	46.80	56.90
Pr	4.66	4.17	3.98	4.39	4.17	4.50	4.92	4.98	6.18
Nd	16.60	14.50	14.00	15.40	14.10	15.60	17.10	17.80	25.00
Sm	3.15	2.67	2.36	3.18	2.83	2.87	3.10	3.37	4.82
Eu	0.94	0.79	0.72	0.93	0.82	0.86	0.97	0.97	1.36
Gd	2.73	2.15	2.08	2.71	2.69	2.52	2.71	2.99	4.18
Tb	0.41	0.35	0.29	0.42	0.38	0.38	0.43	0.47	0.63
Dy	2.41	2.28	1.92	2.50	2.37	2.30	2.48	2.67	3.49
Ho	0.45	0.44	0.38	0.49	0.44	0.46	0.50	0.55	0.69
Er	1.37	1.27	1.13	1.48	1.45	1.32	1.40	1.62	1.76
Tm	0.20	0.19	0.17	0.22	0.20	0.19	0.20	0.24	0.27
Yb	1.29	1.24	1.17	1.32	1.45	1.29	1.42	1.61	1.58
Lu	0.20	0.21	0.17	0.20	0.21	0.19	0.22	0.25	0.26
Hf	3.20	2.90	3.00	3.10	3.40	3.40	3.40	3.90	3.98
Ta	0.97	0.98	1.12	1.49	0.80	1.20	1.20	1.70	1.50
Pb	12.00	13.00	11.00	10.00	9.00	11.00	7.00	9.00	8.00
Th	8.98	8.87	9.73	9.96	8.35	9.00	9.63	11.25	6.40
U	1.30	2.01	2.32	2.86	1.34	1.61	2.74	3.67	1.74
Tl	0.37	0.36	0.41	0.26	<0.02	0.33	0.23	0.02	0.06
Au	< 1	< 1	1.00	< 1	–	–	–	–	–
Ag	< 0.5	< 0.5	< 0.5	< 0.5	<0.5	<0.5	<0.5	<0.5	<0.5
As	4.00	3.00	3.00	3.00	7.00	1.20	0.80	0.50	2.60
Be	1.00	1.00	1.00	2.00	–	–	–	–	–
Bi	< 0.1	< 0.1	0.40	< 0.1	0.01	0.10	0.08	0.01	0.02
Br	< 0.5	< 0.5	< 0.5	< 0.5	–	–	–	–	–
Cd	< 0.5	< 0.5	< 0.5	< 0.5	<0.5	<0.5	<0.5	<0.5	1.10
Ge	0.90	0.90	1.30	1.40	<5	<5	<5	<5	–
Hg	< 1	< 1	< 1	< 1	0.01	0.01	0.01	0.01	0.01
In	< 0.1	< 0.1	< 0.1	< 0.1	0.02	0.01	0.01	0.01	0.04
Ir	< 1	< 1	< 1	< 1	–	–	–	–	–
Mo	< 2	< 2	< 2	2.00	<1	<1	<1	3.00	2.00
S	0.00	0.00	0.00	0.00	0.02	0.01	<0.01	<0.01	0.01
Sb	1.00	0.60	1.00	0.90	0.19	0.11	0.12	0.07	3.77
Se	< 0.5	< 0.5	< 0.5	< 0.5	<0.2	<0.2	<0.2	<0.2	0.20
Sn	< 1	1.00	1.00	1.00	1.00	1.00	1.00	2.00	1.30
Eu_n/Eu^*	0.98	1.01	1.00	0.97	0.91	0.98	1.02	0.93	0.93
$(La/Sm)_n$	5.43	5.82	6.61	5.24	4.96	5.44	5.48	5.52	3.78
$(Dy/Yb)_n$	1.15	1.13	1.01	1.16	1.00	1.10	1.07	1.02	1.36
Sr/Y	52.25	35.92	35.80	33.46	37.45	45.55	49.71	25.09	34.02
La/Yb	21.16	20.00	21.28	20.15	15.45	19.30	19.08	18.45	18.42

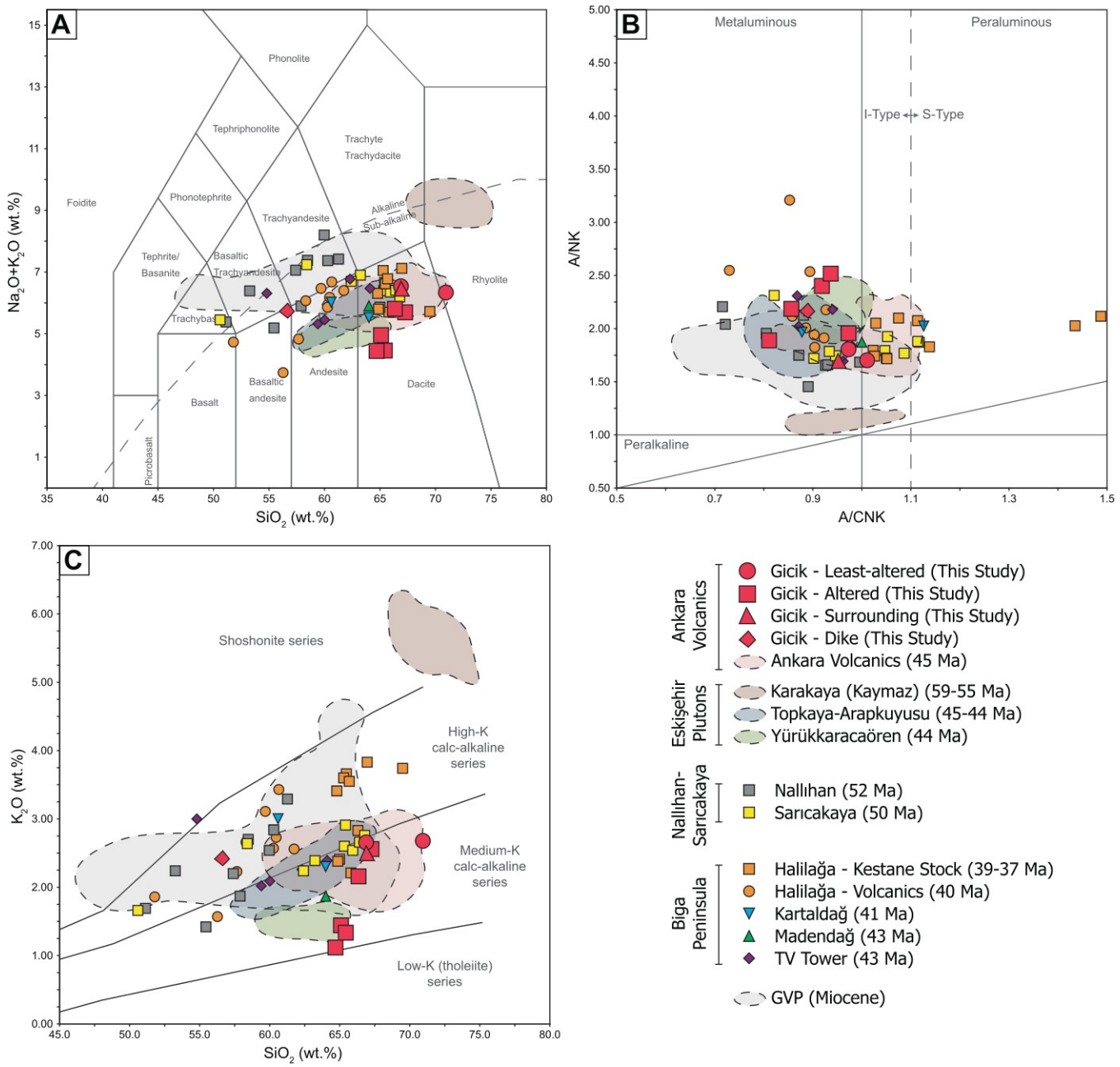


Fig. 7. Plots of the least-altered and altered rock samples from Gicik, and Central Ankara volcanics (both this study and literature data), Biga Peninsula, and Eskişehir-Bursa District. Galatean Volcanic Province also included in the figures for comparison. A) Total-Alkali versus Silica (Middlemost, 1994). The alkalic/sub-alkalic boundary is from Irvine and Baragar (1971), B) ANK versus ACNK diagram (Maniar and Piccoli, 1989). ANK molar $Al_2O_3/Na_2O + K_2O$, ACNK molar $Al_2O_3/CaO + Na_2O + K_2O$, and C) K_2O versus SiO_2 diagram of sub-alkalic rocks (Peccerillo and Taylor, 1976). Data sources: Ach (1982); Seyitoğlu and Büyükönal (1995); Wilson et al. (1997); Besbelli and Varol (2002); Varol et al. (2007, 2008); Ünal-İmer et al. (2013); Kasapoğlu et al. (2016); Leroux (2016); Parlak (2016); Brunetti (2016); Demirbilek et al. (2018); Göçmengil et al. (2022); Güllü and Kadıoğlu (2022).

weakly-argillized rocks due to slightly to moderately acidic nature of the fluids. Relatively coarse-grained muscovitic sericite (Fig. 1E) was also locally observed, and its presence likely indicates slightly higher fluid temperatures.

Silicification: Silicification (Fig. 3) is closely associated with and is restricted to the mineralized veins. It is readily represented by various forms of silica. Groundmass of dacitic wall-rocks adjacent to the veins has been replaced by microcrystalline quartz, whereas phenocryst phases including hornblende, biotite, pyroxene, and plagioclase have been partially to completely leached out due to fluid acidity occasionally resulting in a vuggy appearance (Fig. 11F). Vuggy cavities in silicified dacite have been locally infilled by chalcedony or granular quartz. Silicified wall-rocks also contain minor amounts of illite.

4.6. *Au-Ag ± Te mineralization*

4.6.1. *Mineralized veins*

The Gicik Au-Ag ± Te mineralization is contained within a series of NNE-trending sub-parallel siliceous veins that have been mainly emplaced within steep faults cross-cutting the lower and middle volcanic series (Fig. 3). Surface observations and legacy drill hole data indicate that vein thicknesses typically vary between 1 and 5 m, and rarely

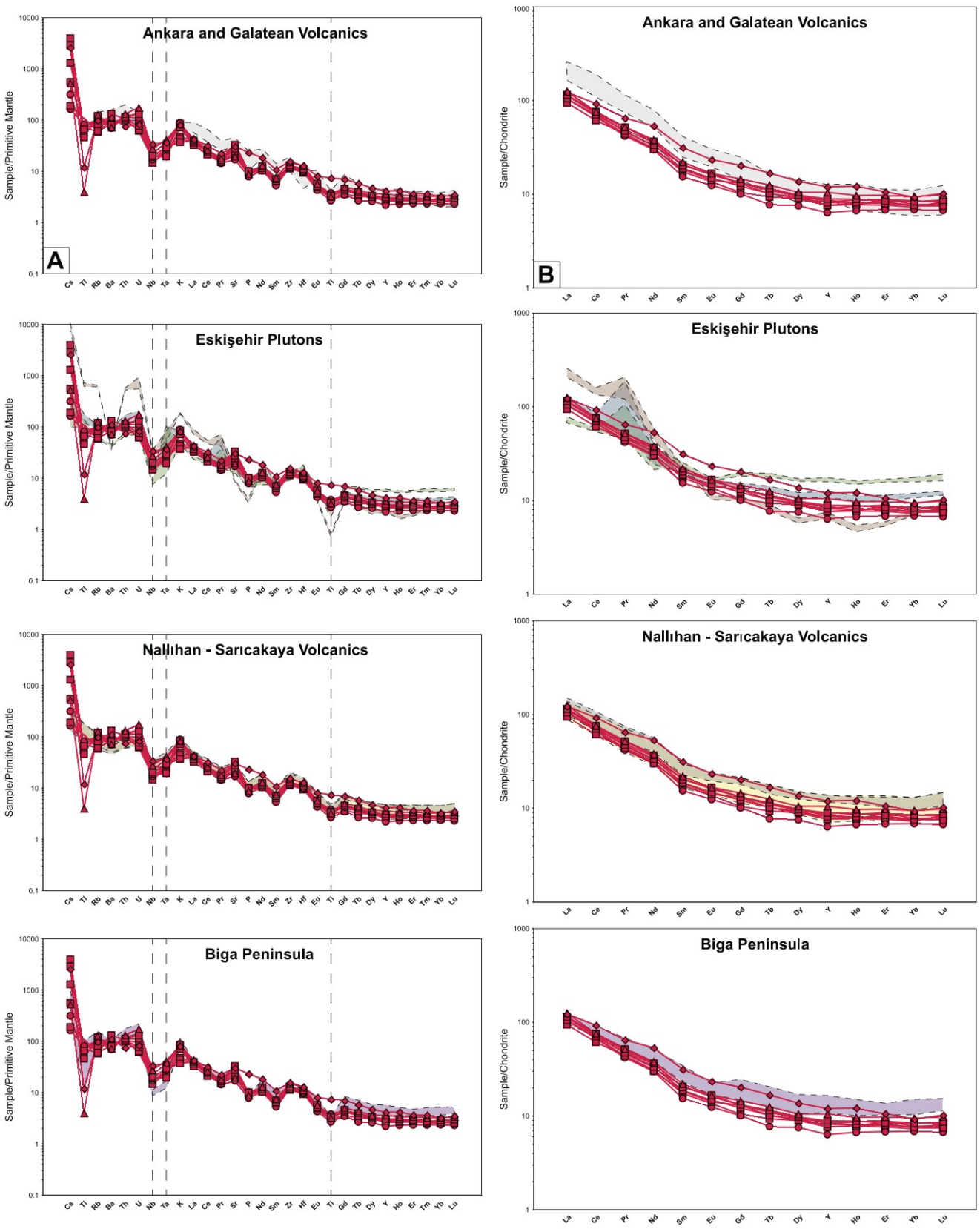


Fig. 8. Multi-element diagrams of the least-altered and altered rock samples from Gicik, and Central Ankara volcanics (both this study and literature data), Biga Peninsula, and Eskişehir-Bursa District. Galatean Volcanic Province also included in the figures for comparison. A) Primitive mantle-normalized diagram, and B) Chondrite- normalized diagram. Primitive mantle normalization values are from Sun and McDonough (1989) and chondrite normalization values are from Sun and McDonough (1989).

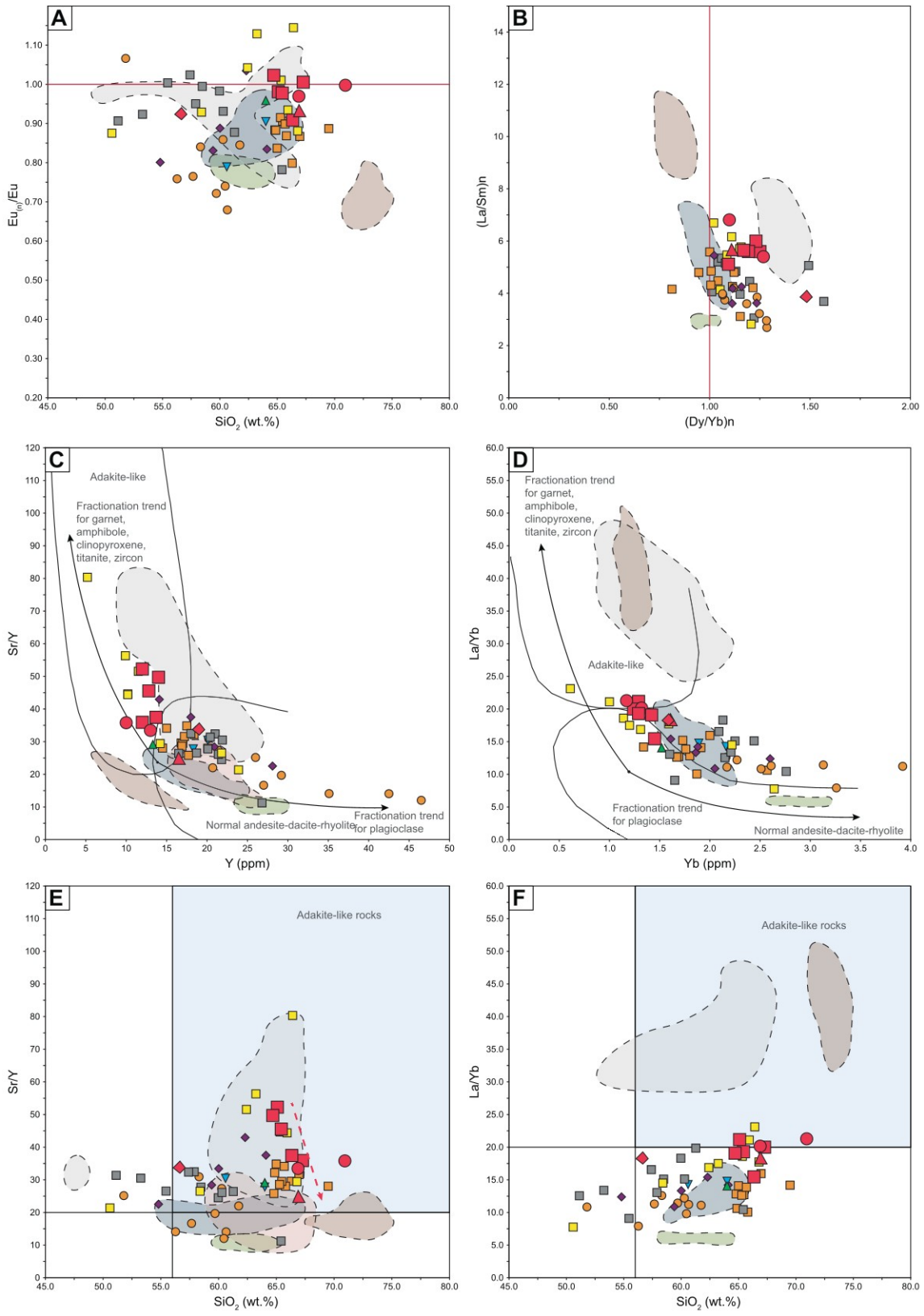


Fig. 9. Trace element diagrams of samples from Gicik, and Central Ankara volcanics (both this study and literature data), Biga Peninsula, and Eskişehir-Bursa District. Galatean Volcanic Province also included in the figures for comparison. A) Eu_n/Eu^* vs. SiO_2, B) $(La/Sm)_n$ vs. $(Dy/Yb)_n$, C) Sr/Y vs. Y, D) La/Yb vs. Yb, E) Sr/Y vs. SiO_2, and F) La/Yb vs SiO_2. Fields for adakite-like rocks from Richards and Kerrich (2007).

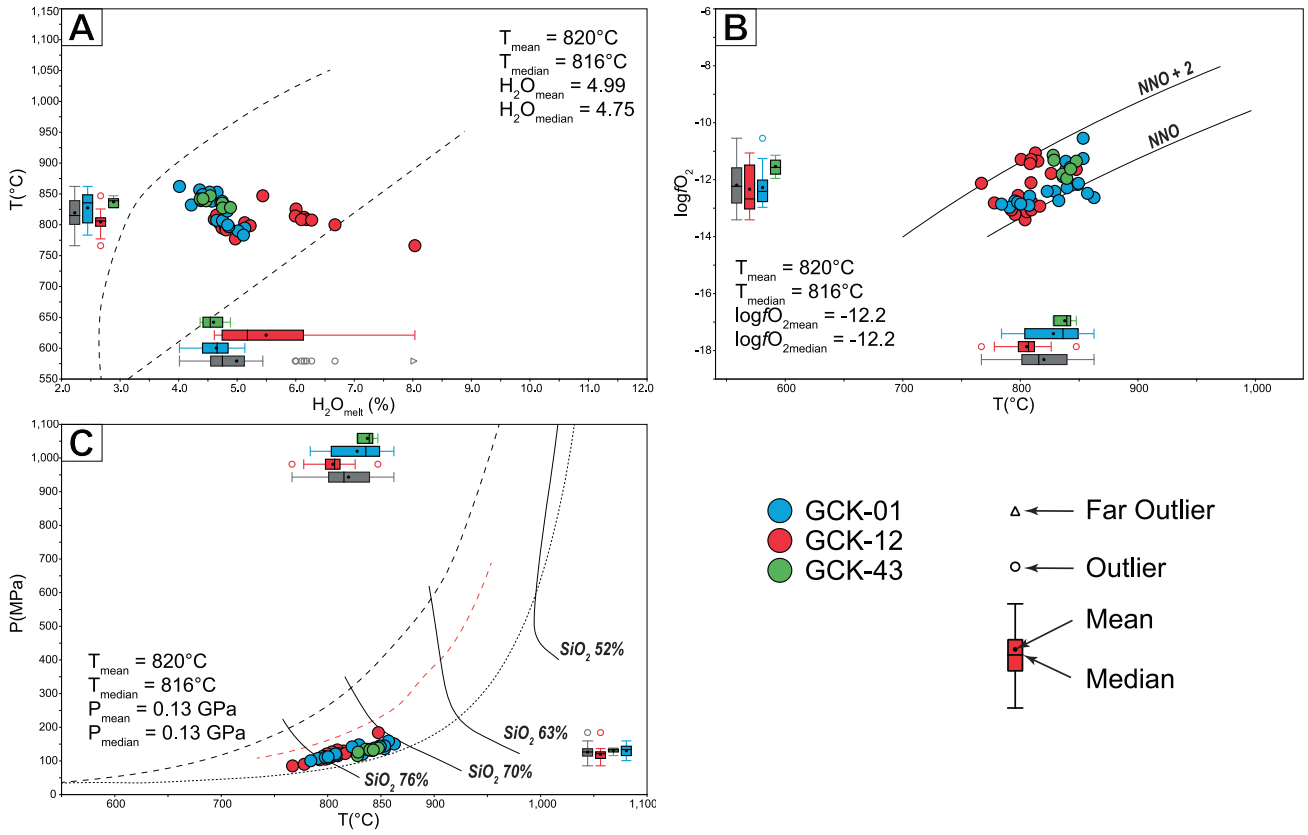


Fig. 10. Empirical results obtained from hornblende phenocrysts from Gicik volcanic sequence (Ridolfi et al., 2010). A) Temperature vs·H_2O_{melt} diagram, B) logf_{02} vs. temperature diagram, and C) Pressure vs. temperature diagram.

reach up to ~ 10 m. Veins are steeply-dipping, planar to curviplanar, often discontinuous, and have been sharply truncated and displaced by post-mineralization structures (Fig. 3). Consequently, strike lengths do not exceed few tens of meters. During early exploration by Eurogold, mapped vein segments were assigned different names as T, Q, G, East, and Creek veins (Figs. 2 and 3). Descriptions below retain the same vein nomenclature for convenience. Summary characteristics of distinct vein segments are provided in Table 6.

T Vein: In the northern part of Gicik, a small number of veins collectively named as the T vein (Fig. 12A) crop out at elevations of 1,100–1,200 m a.s.l. These veins, primarily made up of milky barren quartz at the surface, have limited exposure as they are mostly concealed by alluvium and also by the units of the upper volcanic series (Fig. 3). Some silicified outcrops and quartz-rich float occur in the northeast of Gicik, but no associated veins were identified at the surface. However, significant assay values (up to 16.8 g/t Au over one-meter intervals) were obtained during Eurogold's early initial drilling program. Most mineralization occurs in the east and south of Gicik, where veins provide better exposures between elevations of 1,000–1,100 m a.s.l. due to marked erosion in this sector.

Q Vein: Veins exposed at elevations lower than 1,100 m near the Gicik village include the Q, G, East and Creek veins (Fig. 12B), which host an important part of the known epithermal Au-Ag ± Te mineralization. The N–S-trending Q vein is the original discovery vein and is located within the settled area in the Gicik village. Its thickness varies between 5 and 15 m with a strike length of approximately 65 m. It displays the best lateral zonation from a central silica-rich zone sharply passing into first a 4 m-wide zone of argillized, and later into propylitized dacite (Fig. 12B).

East vein: The East vein was mapped on the east of Gicik and is subdivided into two as E1 and E2 segments (Fig. 3). E1 vein is oriented NE-SW and can be traced at the surface for about 40 m along strike. Its thickness varies between 1 and 3 m (Fig. 12C). The vein itself is poorly-exposed, and thus its full extent is likely underestimated. E1 vein is primarily characterized by fragmented silicified volcanic rocks, and only a minor portion of it is made up of thin silica veins. A cluster of several relatively smaller veins form the NE-SW-trending E2 segment, which has a strike length of ~140 m with its thickness ranging from 2 to 7 m (Fig. 12C). Contrary to E1, it displays a wide variety of hydrothermal textures such as hydrothermal brecciation, lattice bladed, cockade, stockwork veinlets, and dark gray massive silica zones. Fe-sulfide minerals such as pyrite, marcasite, and arsenopyrite are mostly concentrated as disseminations within the E2 vein.

G Vein: The NNE-trending steeply-dipping G veins, extending from the Gicik village (Fig. 12D and E) to farther south towards the peripheral highway, are represented by at least two discontinuous vein segments that are ~ 1 to 3 m-thick and 10 to 60 m-long. Hosted by the agglomerates of the lower volcanic unit, G veins are exposed at relatively lower elevations between 1,070 and 1,130 m a.s.l. Thus, their surface exposures are considered to represent relatively deeper levels of the mineralized system compared to other vein segments. The G vein returned the best assays during Eurogold's drilling campaign with the most significant drill intercept averaging ~ 21.6 g/t Au over an 11-meter-long interval. Parts of these veins were previously exploited through open-pit mining and subsequently back-filled, which precluded accurate mapping of G veins in the mined areas. At higher elevations, the G vein comprises massive coarse- to fine-grained quartz, which passes into gray silica-pyrite and later into colloform banded, well-mineralized silica-sulfide veins at deeper levels.

Creek Veins: Creek veins (Fig. 12F) represent the southernmost sector of the Gicik mineralized system, where the elevation is lowest (960–1,070 m a.s.l.). Creek veins are a swarm of 3–4 m-wide veins that

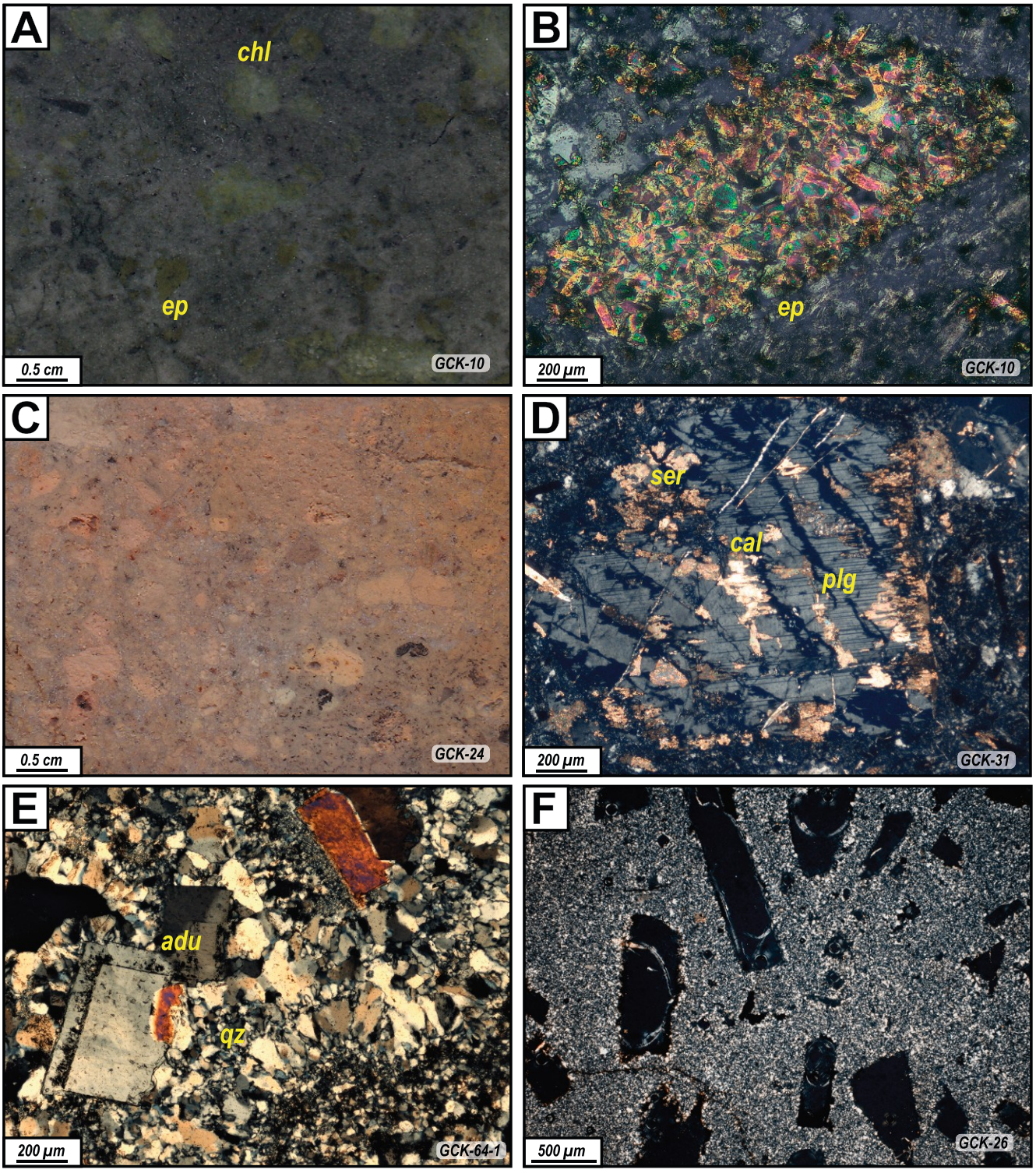


Fig. 11. Hand specimen images and photomicrographs of the various alteration styles observed in Gicik samples. A) Close-up image of propylitic alteration evident by the greenish color due to presence of chlorite (chl) and epidote (ep). B) Epidote replacing a primary ferromagnesian mineral phase. C) Close-up view of argillic alteration. Note the complete replacement of plagioclase phenocrysts by clay minerals. D) Sericite (ser) and calcite (cal) after plagioclase, E) Euhedral adularia (adu) crystal in argillized dacite. F) Intensely-silicified, porphyritic dacite in which primary phenocryst phases have been leached out, leaving behind a vuggy appearance.

are oriented NE–SW with a strike length of ~ 40 m. These veins mainly comprise massive quartz locally displaying comb and lattice-bladed textures, and rare colloform-banding.

4.6.2. Vein paragenesis and mineralization

Veins at Gicik recorded multiple stages of incremental growth with successive development of various textural styles and mineral assemblages. Siliceous veins display broadly similar textures and ore/gangue mineralogy, but some textures are better developed in certain vein

Table 6
Summary descriptions of Gicik veins.

Vein	Segment	Thickness	Exposed Strike Length	Orientation	Description	Textures	Ore Minerals	Gangue Minerals
T	–	~2–3 *m*	~120 *m*	NE-SW	Blocks and boulders of silicified intermediate composition volcanic rocks	2–5 cm thick massive quartz veinlets	–	Quartz
Q	Q1	~5–15 *m*	~65 *m*	N-S	Siliceous vein surrounded by intensely altered host rock	Stockwork, colloform banding, lattice bladed, cockade, open space filling, hydrothermal breccia	Pyrite	Quartz, amethystine quartz
	Q2	~2–3 *m*	~37 *m*	NE-SW	Two vein sets merging at the south forming the main vein	Colloform, massive, open space filling, cockade, hydrothermal breccia	Pyrite	Quartz
G	–	~1–3 *m*	~10–60 *m*	NE-SW	Comprises of several small veins	Colloform banding, gray colored silicification, open space filling	Pyrite, arsenopyrite, tetrahedrite	Quartz
East	E1	~1–3 *m*	~15–40	NE-SW	Blocks and boulders of silicified host rock	–	–	Quartz
	E2	~2–7 *m*	~140 *m*	NE-SW	Several thin veins in the same orientation forming the main vein	Hydrothermal breccia, gray colored silicification, stockwork	Pyrite, arsenopyrite	Quartz
Creek	–	~3–4 *m*	~40 *m*	NE-SW	Silica vein with intensely silicified host rock	Massive, open space filling	Minor pyrite	Quartz

segments. This variation is interpreted, at least in part, due to different levels of exposure between veins that are largely concealed in the northern part of the study area and the southerly veins around which narrow valleys and creeks provide access to deeper levels of the hydrothermal system.

Most veins at Gicik have a central zone of massive, milky quartz that is characterized by interlocking crystals of abundant fine-grained, anhedral mosaic/jigsaw quartz in thin section (Fig. 13A). Coarser-grained varieties of quartz are also present in massive silica veins, but these quartz crystals are often polygonal and are interpreted to have formed through recrystallization of finer-grained quartz. Northerly veins with relatively poor exposure, such as the T vein, mainly display this type of texture at the surface. Recent construction work carried out along an extension of the T vein, however, has revealed presence of various overprinting textures (e.g., breccias as well as lattice-bladed and cockade textures).

Massive, milky quartz is typically barren of sulfides and it represents the earliest stage of vein development at Gicik. Milky quartz was first overprinted by gray quartz-sulfide veinlets (Fig. 13A), and then progressively by lattice bladed quartz (Fig. 13B), hydrothermal brecciation (Fig. 13C), and colloform banding (Fig. 13D) with all stages variably associated with gold mineralization.

Thinly stockworking veinlets with gray silica and sulfide infill occur as an overprint mostly along the margins of the massive milky quartz veins, and laterally extending into the argillized dacite and dacitic agglomerate. Intensity of stockworking around individual veins is low particularly in the northern and central sectors of vein system. On the other hand, sub-parallel sets of massive quartz veins in the southern sector of the study area were observed as surrounded by domains of stronger intensity stockworking veinlets of silica-Fe-sulfides (Fig. 13E). The colloform banded "gray silica-sulfide veinlets" consist of fine bands of microcrystalline quartz, cryptocrystalline silica, and very fine-grained sulfides. Sulfide abundances are typically <5 vol.% and the sulfide assemblage is comprised by finely-disseminated pyrite with lesser arsenopyrite and marcasite (Fig. 13F). In gray silica-sulfide veins, gold was not detected petrographically, but EPMA studies of sulfides returned gold concentrations of up to ~410 ppm and ~ 160 ppm from pyrite and arsenopyrite grains, respectively (Table 7).

Dark gray quartz-sulfide veins were overprinted by lattice bladed textures (Fig. 13C) characterized by platy quartz crystals that probably replaced earlier calcite deposited from boiling fluids. Lattice bladed veins are abundant throughout Gicik, but have been particularly well-developed along certain veins such as in the Q vein immediately to the west and southwest of Gicik. Some lattice bladed quartz is also present in the T vein, Creek veins and E1-2 veins. In these veins, platy quartz crystals are surrounded by microcrystalline to cryptocrystalline silica. Sulfide abundances are typically very low (<3 vol.%) with main sulfide phase being fine-grained pyrite accompanied by rare fine-grained (<40 μm) native gold (Fig. 13G).

Hydrothermal breccias are common throughout the Gicik deposit, overprinting both the gray silica-sulfide and lattice bladed veins, particularly within the Q and G veins (Fig. 13C). Breccias have polymictic character and are comprised by sub-rounded to angular clasts of argillized andesite as well as by fragments of gray silica-sulfide and less commonly by bladed quartz veins (Fig. 13C). Some of the breccias contain clasts showing comb/crustiform textures with coarse-grained and growth-zoned quartz (Fig. 13C). Comb/crustiform quartz is not known at surface, and thus, such fragments were interpreted to have been derived from deeper levels of the epithermal system. Breccia matrices are made up of colloform bands of cryptocrystalline to microcrystalline silica without any significant sulfides (Fig. 13H). Where fine-grained silica matrix developed in concentric bands around clasts, breccias appear to have cockade textures (Fig. 13H).

Amethystine quartz was identified in Q1 vein, where it commonly occurs as a late-stage infill in vugs and fractures. This phase is not associated with any mineralization. Rare granular quartz is also present in hydrothermal breccias in the Q1 vein. Interestingly, these granular quartz clasts contain primary co-existing two-phase, vapor-rich and also multi-phase, high salinity fluid inclusions that trapped halite and opaque solid phases (Fig. 13I).

Main stage Au-Ag-Te mineralization was introduced later in the form of colloform silica-rich veins that are best developed at surface along the G vein (Fig. 14A). These primarily occur as massive, colloform silica veins or more locally as matrix-supported breccia veins that are up to ~30 cm-wide. Colloform bands are dominated by chalcedonic silica and microcrystalline quartz. However, in places, colloform bands may also be dominated by feathery (or flamboyant or plumose) quartz (Fig. 13F) that is much coarser-grained and more pristine-looking under the microscope. Similar to massive silica veins, appearance of such coarse-grained quartz is interpreted to be a result of widespread recrystallization at Gicik. Where brecciated, colloform silica dominates the matrix, which surrounds various angular to sub-angular fragments derived from earlier siliceous veins as well as fragments of argillized and silicified dacitic wall-rocks.

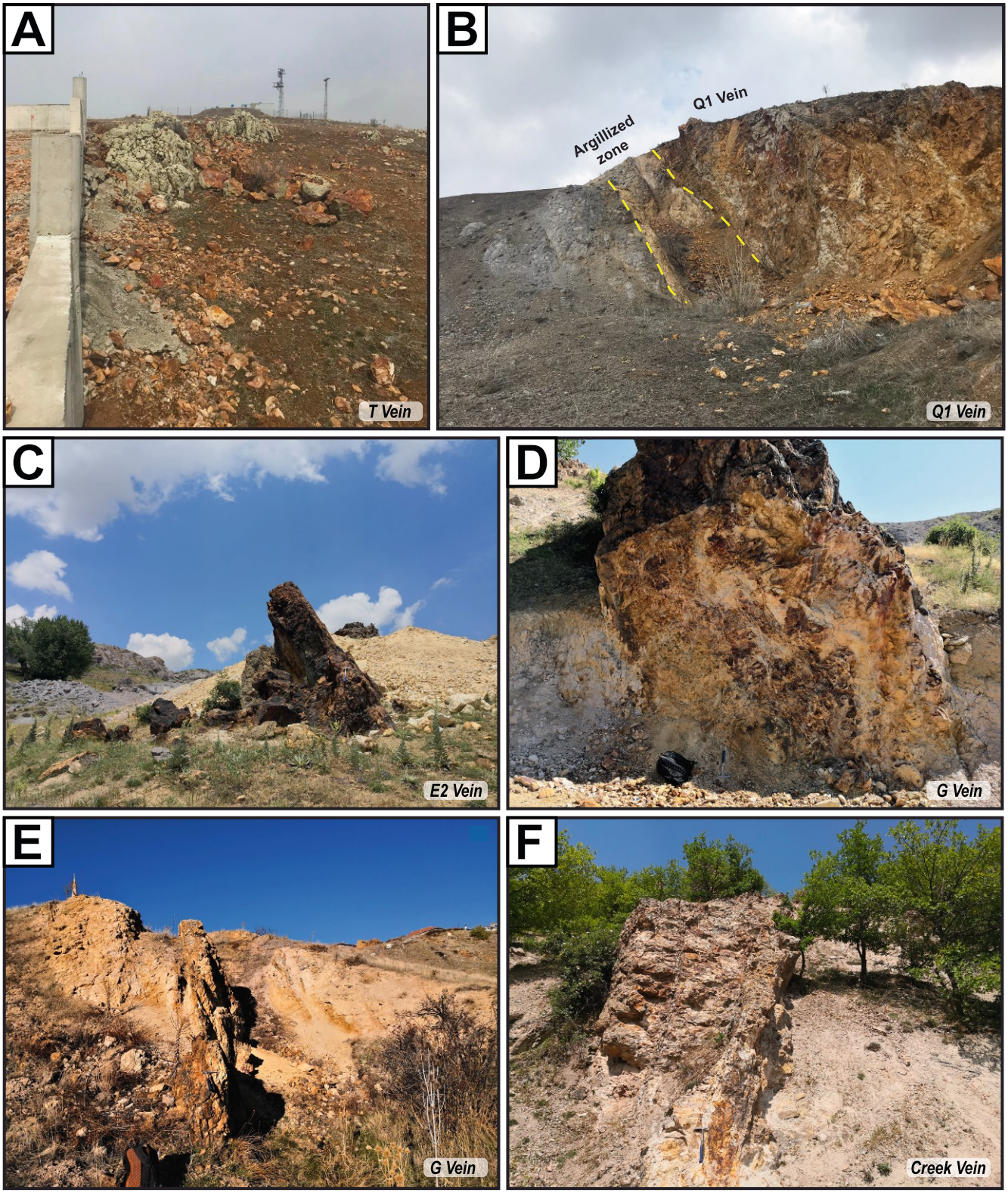


Fig. 12. Field photographs of A) T vein exposed in the north of Gicik. B) Contact between argillized agglomerate and siliceous vein in Q-1 vein in the north of Gicik Village. C) Outcrop view of NE–SW trending E2 vein. D) Southern segment of the G Vein. Dark brown colored center is dominated by dark gray silicified zone, with disseminated pyrite, cut by thin, white colored quartz veinlets. E) The best exposed section of the NE-SW trending northern segment G Vein exposed immediately to the south of Gicik village. F) Best exposed section of northerly Creek veins.

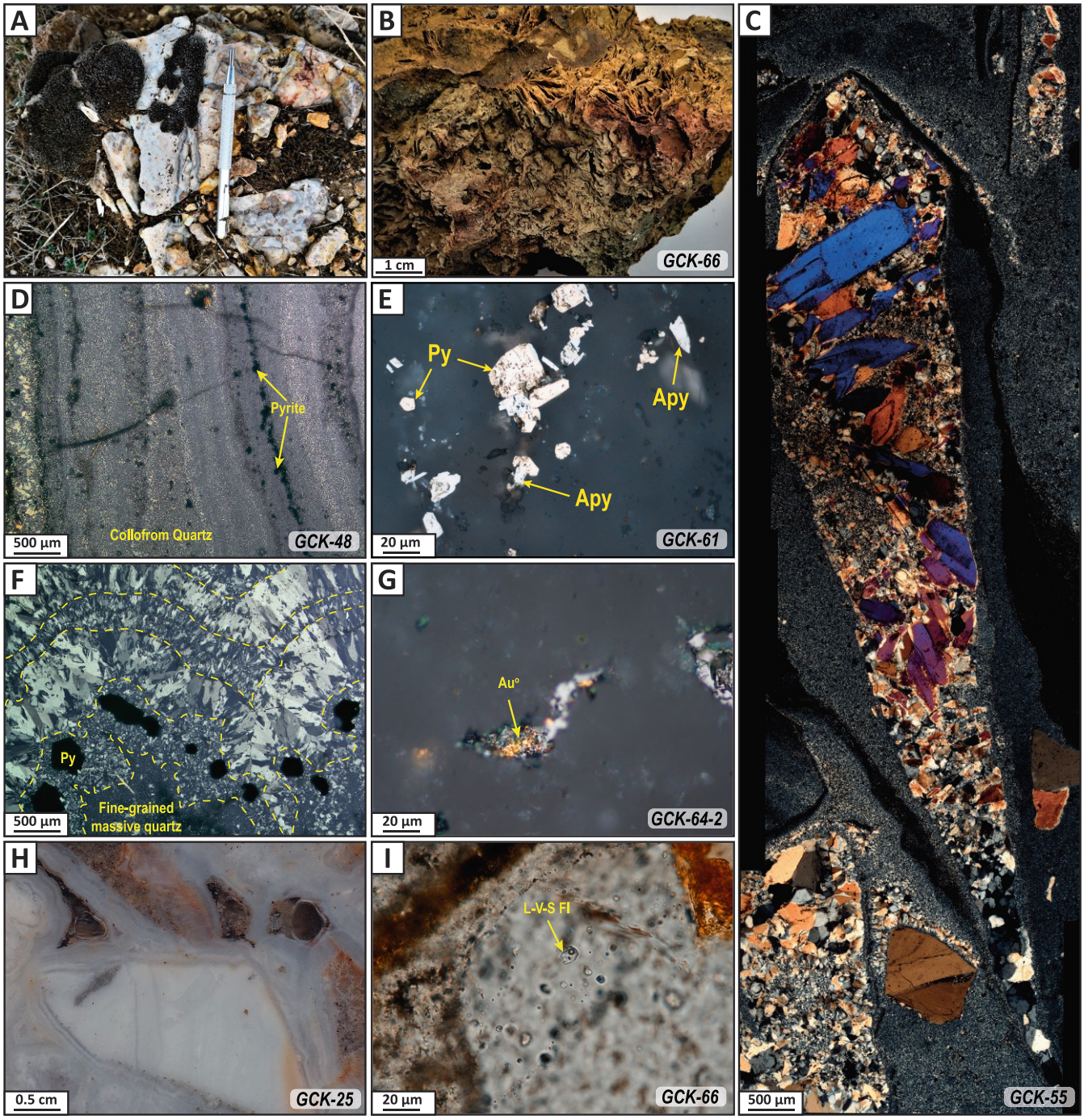


Fig. 13. Various vein textures observed in Gicik veins. A) Outcrop image of dark gray, fine-grained sulfide-rich bands overprinting massive milky quartz. B) Hand specimen of lattice bladed texture vein sample. C) Hydrothermal breccia sample containing vein clasts with euhedral quartz crystals. D) Photomicrograph of colloform bands with minor disseminated pyrite. E) Fine disseminations of pyrite (py) and arsenopyrite (apy). F) Photomicrograph of late-stage barren, coarse-grained quartz bands enveloping fine-grained massive quartz with sulfides. G) Native Au grain in siliceous vein. H) Close-up image hydrothermal breccia sample containing early vein clasts surrounded by colloform-banded silica. I) Polyphase (L-V-S) fluid inclusions hosted in quartz clasts from breccia veins.

The late Au-Ag-Te veins have relatively higher abundance of sulfides (up to ~10 vol.%) compared to earlier veins and these also display a greater variation of ore minerals including sulfides, sulfosalts, tellurides, and rare selenides. Coarse (up to 3 cm-long), euhedral Ag-tetrahedrite and fine- to medium-grained, euhedral pyrite are the predominant phases. Electron microprobe analyses indicated elevated levels of silver (up to ~7 wt.%) and zinc (up to ~7.5 wt.%), as well as significant amounts of Se (up to 0.8 wt.%) and Cd (up to 0.6 wt.%; Table 6) in Ag-tetrahedrite. Other sulfide phases are minor chalcopyrite and sparse sphalerite. The former is observed as intergrown with Ag-tetrahedrite and pyrite, whereas sphalerite is commonly present as minute inclusions within aforementioned sulfides and less commonly as isolated grains (Fig. 14B).

In the main stage veins, gold primarily occurs in native form (Fig. 14C) and as electrum (Fig. 14D and 14E) with grain sizes ranging between 10 and 80 µm. Various gold-silver telluride minerals also occur alongside native gold and electrum primarily including calaverite ($AuTe_2$; Fig. 14C), sylvanite ($(Au,Ag)_2Te_4$; Fig. 14D), and petzite

Table 7
Summary of chemical data from ore minerals. All values are reported in wt.%.

Element			As	Se	S	Sb	Cu	Pb	Zn	Fe	Hg	Co	Cd	Te	Ag	Au	Ni	Pt	Bi	Total
GCK-51	**Chalcopyrite**	**Min**	0.03	–	32.32	–	40.30	–	1.33	23.33	–	–	–	–	0.03	–	–	–	–	99.69
		Max	0.05	–	33.42	–	42.48	–	1.64	25.26	–	–	–	–	0.03	–	–	–	–	99.90
		Avg	0.04	–	32.93	–	41.12	–	1.49	24.21	–	–	–	–	0.03	–	–	–	–	99.79
		Std	0.01	–	0.37	–	0.81	–	0.11	0.63	–	–	–	–	0.00	–	–	–	–	0.09
	Covellite	**Min**	–	–	25.56	–	71.49	–	2.58	0.14	–	–	–	–	–	0.17	0.06	–	–	100.00
		Max	–	–	25.56	–	71.49	–	2.58	0.14	–	–	–	–	–	0.17	0.06	–	–	100.00
		Avg	–	–	25.56	–	71.49	–	2.58	0.14	–	–	–	–	–	0.17	0.06	–	–	100.00
		Std	–	–	–	–	–	–	–	–	–	–	–	–	–	–	–	–	–	–
	Galena	**Min**	0.02	–	8.68	–	0.85	85.64	0.15	0.02	–	0.03	–	–	0.04	–	0.33	–	–	99.52
		Max	0.50	–	11.55	–	1.64	90.23	0.78	0.86	–	0.18	–	–	0.04	–	0.68	–	–	100.01
		Avg	0.18	–	10.36	–	1.26	87.10	0.44	0.22	–	0.07	–	–	0.04	–	0.44	–	–	99.97
		Std	0.14	–	0.68	–	0.28	1.08	0.16	0.23	–	0.05	–	–	0.00	–	0.10	–	–	0.12
GCK-61	**Pyrite**	**Min**	0.01	0.01	50.92	0.01	0.01	–	0.01	44.02	–	0.12	0.01	0.01	0.00	0.00	–	–	–	97.44
		Max	4.51	0.04	54.67	0.34	0.12	–	0.22	46.27	–	0.12	0.03	0.02	0.13	0.04	–	–	–	100.54
		Avg	0.39	0.02	53.48	0.06	0.03	–	0.03	45.50	–	0.12	0.02	0.01	0.03	0.02	–	–	–	99.30
		Std	0.97	0.01	0.68	0.10	0.04	–	0.05	0.49	–	0.00	0.01	0.00	0.04	0.01	–	–	–	0.49
	Arsenopyrite	**Min**	42.92	–	21.55	–	–	–	0.03	28.73	–	0.01	–	–	0.09	–	–	–	–	99.25
		Max	48.56	–	24.71	–	–	–	0.07	33.66	–	0.01	–	–	0.16	–	–	–	–	99.58
		Avg	45.36	–	22.51	–	–	–	0.05	31.46	–	0.01	–	–	0.13	–	–	–	–	99.38
		Std	1.78	–	0.97	–	–	–	0.02	1.49	–	0.00	–	–	0.04	–	–	–	–	0.10
	Sphalerite	**Min**	0.10	–	26.87	0.21	3.20	–	59.95	0.04	–	0.04	0.22		0.02	–	–	0.14	–	98.44
		Max	0.19	–	28.48	0.21	11.06	–	66.84	0.45	–	0.09	0.22		0.02	–	–	0.14	–	99.01
		Avg	0.14	–	27.82	0.21	4.83	–	65.54	0.27	–	0.06	0.22		0.02	–	–	0.14	–	98.70
		Std	0.04	–	0.54	0.00	2.80		2.51	0.13		0.02	0.00		0.00	–	–	0.00		0.20
GCK-64–1	**Tetrahedrite**	**Min**	3.73	0.20	23.86	15.93	34.80	–	3.80	0.01	0.01	0.01	0.24	1.54	1.41	0.01	–	–	0.01	94.26
		Max	6.23	0.96	25.34	24.88	40.59	–	7.58	0.13	0.51	0.02	1.08	1.54	8.50	0.07	–	–	0.09	103.12
		Avg	4.89	0.45	24.77	22.37	37.02	–	6.08	0.08	0.17	0.01	0.38	1.54	3.25	0.03	–	–	0.02	99.46
		Std	0.69	0.21	0.41	2.78	1.53	–	1.13	0.04	0.18	0.00	0.20	0.00	2.35	0.02	–	–	0.03	2.56
GCK-64–2	**Pyrite**	**Min**	0.09	0.02	52.39	0.03	0.01	–	0.01	41.54	–	0.01	0.01	0.01	0.01	0.01	–	–	–	98.12
		Max	2.67	0.61	54.20	0.26	1.18	–	0.03	46.62	–	0.01	0.03	0.43	0.33	0.96	–	–	–	100.89
		Avg	1.09	0.20	53.21	0.16	0.42	–	0.02	45.42	–	0.01	0.01	0.22	0.09	0.37	–	–	–	99.99
		Std	1.07	0.24	0.57	0.10	0.50	–	0.01	1.90	–	0.00	0.01	0.20	0.14	0.43	–	–	–	0.68
	Sphalerite	**Min**	0.02	0.04	28.65	0.02	0.40	–	57.48	0.02	–	–	0.47	0.03	0.01	–	–	–	–	89.19
		Max	0.08	0.10	29.46	0.77	2.08	–	58.84	0.07	–	–	0.77	0.07	0.15	–	–	–	–	90.16
		Avg	0.05	0.06	29.24	0.36	1.23	–	57.94	0.05	–	–	0.65	0.05	0.09	–	–	–	–	89.64
		Std	0.02	0.03	0.31	0.25	0.55	–	0.49	0.02	–	–	0.11	0.02	0.06	–	–	–	–	0.33
	Tetrahedrite	**Min**	3.69	0.19	24.97	17.74	37.45	–	4.09	0.02	0.01	0.01	0.14	0.28	0.36	0.01	–	–	–	93.25
		Max	7.92	0.60	25.45	24.90	41.32	–	7.60	0.10	0.06	0.02	0.37	0.28	0.81	0.05	–	–	–	103.63
		Avg	6.53	0.36	25.20	23.19	38.30	–	6.95	0.07	0.02	0.01	0.31	0.28	0.59	0.03	–	–	–	101.54
		Std	1.25	0.10	0.13	2.05	1.11	–	1.08	0.02	0.02	0.00	0.07	0.00	0.12	0.01	–	–	–	3.24
GCK-65	**Au-Ag-Te**	**Min**	0.02	0.05	3.47	0.04	0.05	0.00	–	0.01	0.01	0.01	–	0.00	0.00	0.00	0.38	0.03	0.03	92.19
		Max	0.44	14.68	10.69	4.77	6.68	3.14	–	4.71	9.66	0.11	–	94.79	47.25	88.61	4.18	0.20	1.57	100.01

(*continued on next page*)

Table 7 (*continued*)

Element		As	Se	S	Sb	Cu	Pb	Zn	Fe	Hg	Co	Cd	Te	Ag	Au	Ni	Pt	Bi	Total
Chalcopyrite	Avg	0.13	2.24	6.55	2.20	1.47	1.17	–	0.39	1.99	0.05	–	29.25	15.30	46.19	0.62	0.12	0.58	99.60
	Std	0.13	3.57	2.46	1.59	1.76	0.92	–	0.83	1.90	0.03	–	33.82	14.03	29.18	0.58	0.07	0.37	1.22
	Min	0.04	0.74	32.69	–	40.94	2.64	–	22.69	–	–	–	0.09	–	–	–	–	–	99.83
	Max	0.04	0.74	32.69	–	40.94	2.64	–	22.69	–	–	–	0.09	–	–	–	–	–	99.83
	Avg	0.04	0.74	32.69	–	40.94	2.64	–	22.69	–	–	–	0.09	–	–	–	–	–	99.83
	Std	0.00	0.00	0.00	–	0.00	0.00	–	0.00	–	–	–	0.00	–	–	–	–	–	0.00
Covellite	Min	0.07	0.81	23.54	0.07	70.18	2.31	–	1.35	–	–	–	0.02	–	–	–	0.18	–	100.00
	Max	0.57	0.88	25.71	0.07	71.74	2.46	–	1.35	–	–	–	0.13	–	–	–	0.18	–	100.02
	Avg	0.32	0.85	24.63	0.07	70.96	2.39	–	1.35	–	–	–	0.08	–	–	–	0.18	–	100.01
	Std	0.25	0.04	1.09	0.00	0.78	0.08	–	–	–	–	–	0.06	–	–	–	0.00	–	0.01
Pyrite	Min	0.09	0.02	50.82	0.03	0.01	3.11	0.01	43.22	–	–	0.01	0.01	0.01	0.01	–	0.37	–	98.12
	Max	0.99	0.85	54.20	0.05	0.60	3.45	0.03	46.62	–	–	0.04	0.49	0.12	0.03	–	0.43	–	100.89
	Avg	0.36	0.18	52.97	0.04	0.17	3.28	0.02	45.85	–	–	0.02	0.18	0.03	0.02	–	0.40	–	99.99
	Std	0.37	0.30	0.96	0.01	0.25	0.17	0.01	1.09	–	–	0.01	0.22	0.04	0.01	–	0.03	–	0.68

(Ag_3AuTe_2; Fig. 14E). Hessite (Ag_2Te; Fig. 14E) is sparse and further SEM analyses revealed presence of various Ag-Cu selenide phases tentatively identified as klockmannite (CuSe; Fig. 14F), bohdanowiczite ($AgBiSe_2$; Fig. 14G), and penzhinite ($(Ag,Cu)_4Au(S,Se)_4$). Colloform-silica veins returned highest gold assays of up to 68.5 g/t during Eurogold's drilling. A breccia sample obtained from the G vein cropping out to the south of Gicik village also returned significant concentrations for Au (1.3 g/t), Te (>500 ppm; above upper analytical detection limit), Ag (>100 ppm), Cu (>1 wt%), and Zn (0.23 wt%).

Almost all surface samples of mineralized rocks display various degrees of supergene oxidation particularly of Fe-sulfides. Veins with pyrite, arsenopyrite, and marcasite commonly show partial to complete replacement by hematite and goethite (Fig. 14H). Coarse Ag-tetrahedrite grains in main stage, colloform silica veins with Au–Ag ± Te mineralization have been partially transformed into covellite along rims, and other minute, isolated crystals of covellite likely developed after finely-disseminated chalcopyrite (Fig. 14B and D).

4.7. Structure

Structure exerted a major control on vein formation at Gicik as majority of the mineralized veins have been emplaced along steeply-dipping faults. A total of 142 measurements from fault planes, 156 measurements from veins, and 26 measurements from dikes were plotted on a stereoplot to identify the relation between faults and veins (Fig. 15).

Two fault sets were identified in the field. The first set of faults strike NNE with dips varying between 34° to 88°. Kinematic analyses of fault plane data indicated that these are dextral oblique-slip faults with predominant reverse movement. Mineralized veins and basaltic andesite dikes have comparable NNE strikes to this group of faults and they also mostly dip steeply to SE (Figs. 3 and 15). Earlier NNE-trending faults and veins are cut and displaced consistently by E–W-trending pure dextral strike slip and NE–SW trending normal faults (Figs. 3 and 15). Offsets are minor and do not exceed few meters throughout Gicik. It is clear that there is a coherence between the trend of mineralized veins and NE-trending strike-slip oblique faults. The later normal and pure dextral strike slip faults appear to cut and offset the veins. The displacement of dikes and veins by the strike-slip faults is evident in the field; however, the relationship between the normal faults with the dikes and veins is mostly interpreted due to lack of significant field evidence.

4.8. $^{40}Ar/^{39}Ar$ geochronology

Two volcanic rock samples that have undergone argillic alteration from nearby mineralized veins at Gicik were analyzed through $^{40}Ar/^{39}Ar$ geochronology with an aim to determine the age of alteration. $^{40}Ar/^{39}Ar$ spectra and inverse isochron diagrams are shown in Fig. 16 and analytical data is reported in Table 8.

Sample 542639 is a hydrothermal breccia sample from the western sector of the study area, affected from intense argillic (quartz-sericite/illite) alteration. This sample yielded an undisturbed plateau age of 45.31 ± 0.38 Ma (MSWD = 2.1) in five consecutive steps containing 64% of the released ^{39}Ar (Fig. 16A). The plateau age closely overlaps with the inverse isochron age (44.66 ± 0.55 Ma; Fig. 16B) as well as with the total gas age (44.44 ± 1.30 Ma; Table 8).

Sample 661564 represents a dacitic rock that shows intense alteration into sericite (illite) and quartz from the northern part of the Q-1 vein. This sample yielded one low apparent age step followed by a four-step plateau containing 72.5% of the released ^{39}Ar (Fig. 16C). Plateau age obtained from these steps is 46.95 ± 0.73 Ma (MSWD = 2.9). In the spectra, the plateau was followed by younger age steps (Fig. 16C) suggesting diffusive ^{40}Ar loss due to partial resetting. An inverse isochron age could not be obtained from this sample. The total gas age of 44.14 ± 0.52 Ma is accepted as a better estimate of the true age of this sample.

The two illite $^{40}Ar/^{39}Ar$ ages reported hereby closely agree with each

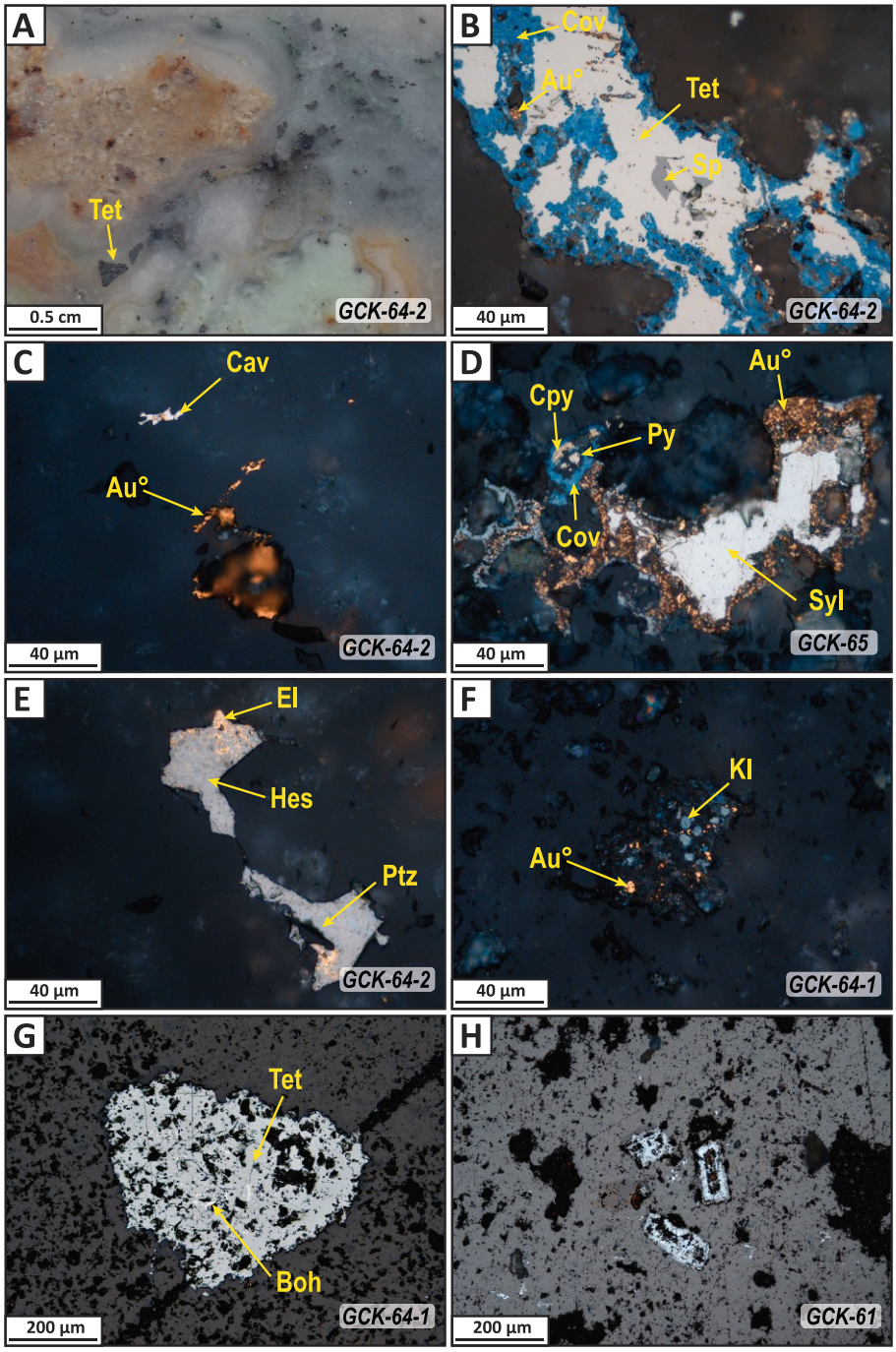


Fig. 14. Close-up images and photomicrographs of mineralized samples from Gicik. A) Close-up view of hydrothermal breccia with altered dacite and hydrothermal vein clasts surrounded by colloform silica and coarse, euhedral crystals of Ag-tetrahedrite (Tet). B) Sphalerite (Sp) and native Au enclosed in Ag-tetrahedrite. Supergene covellite (Cov) has partly replaced Ag-tetrahedrite along rims and fractures. C) Native Au and calaverite (Cav) in siliceous vein. D) Native Au surrounding sylvanite (Syl). Pyrite (Py) and chalcopyrite (Cpy) also occur as fine disseminations. The latter has been mostly replaced by supergene covellite. E) Au-rich electrum developed in petzite (Ptz) and hessite (Hes). F) Native Au and crystals of klockmannite (Kl). G) Bohdanowiczite (Boh) inclusions in tetrahedrite. H) Euhedral crystals of disseminated pyrite and arsenopyrite transformed into goethite.

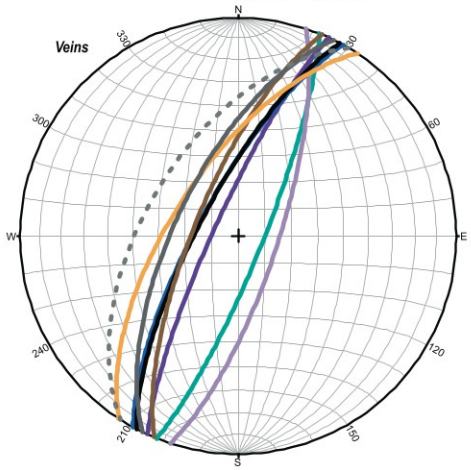
other and constrain the age of epithermal-style quartz-illite alteration at Gicik to middle Eocene. Furthermore, these ages also closely overlap with K-Ar ages from biotite (44.7 ± 1.0 Ma) and hornblende (44.5 ± 1.0 Ma) from dacitic lavas from Gicik (Ach and Wilson, 1986) suggesting a temporal relationship between volcanic activity and epithermal-style alteration/mineralization at Gicik (Table 9).

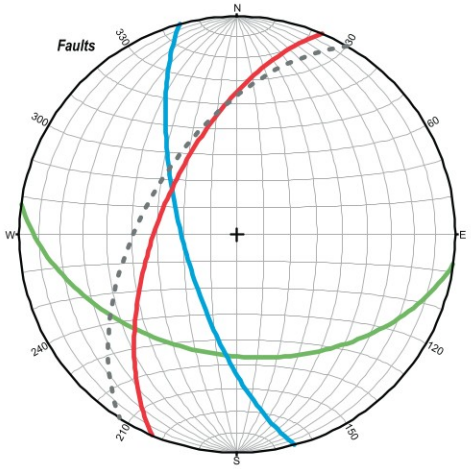
5. Discussion

5.1. Tectonic setting of the Gicik Au-Ag + Te deposit

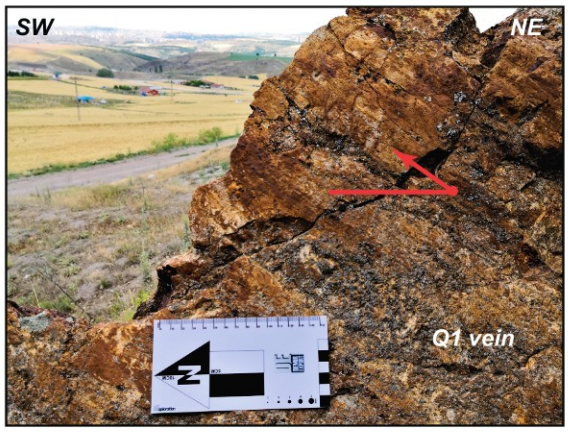
New illite $^{40}Ar/^{39}Ar$ geochronological data presented in this study from argillically-altered lithologies revealed that hydrothermal activity at Gicik occurred in the middle Eocene (~44.5 Ma). These correlate well with the previously published dates on andesitic to dacitic volcanism (47–42 Ma) from the north of Ankara (Ach and Wilson, 1986; Seyitoğlu

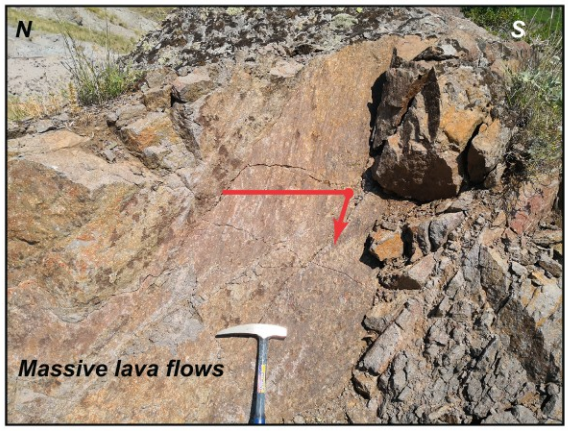
Type of Structure	Easting	Northing	Average Orientation (Dip Amount/Dip Direction)	#
T Vein	493736	4430058	67/296	10
Q1 Vein	497263	4429308	75/108	24
Q2 Vein	497046	4428931	81/295	25
G Veins	497430	4428972	81/112	31
East1 Vein	497638	4429049	65/303	12
East2 Vein	497880	4429066	74/293	23
Creek Vein	496552	4427573	75/298	31
Basaltic Andesite Dykes	496779	4428175	75/299	26
E-W Dextral Strike Slip Faults	497380	4428558	44/188	15
NNW-SSE Normal Faults with Dextral Component	497297 497503 497577 497788	4428766 4428519 4428610 4428642	70/255	49
NNE Reverse Faults with Dextral Component	497780 497825 497233 497839	4428770 4428840 4429132 4428870	61/293	78











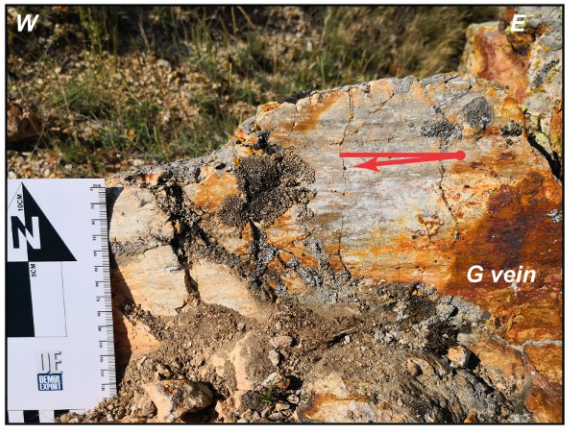


Fig. 15. Average trends of the structural features (faults, veins and dikes) plotted on the stereograph to understand their relation with each other (on the left), and representative field images of main fault types observed in Gicik (on the right).

and Büyükönal, 1995; Dönmez et al., 2009; Table 9), thus providing compelling evidence that the Gicik epithermal Au mineralization formed in close temporal association with the middle Eocene (~44.5 Ma) magmatic activity along the collisional belt between the Pontide and ATB continental fragments. However, the large errors attached to previously published ages from volcanic rocks (Table 9) preclude accurate determination of the time relationship between epithermal-style alteration and igneous activity. Volcanic and volcaniclastic host-rocks at Gicik developed at least about 20 m.y. following the Late Cretaceous continent–continent collision and ocean closure along the İAESZ (Okay and Tüysüz, 1999; Kaymakcı et al., 2009; Çinku et al., 2016; Okay et al., 2020).

The dacitic volcanic-volcaniclastic samples and the basaltic andesite dike sample from Gicik are medium-K and sub-alkaline in character, and are characterized by enrichments in LILE and depletions in HFSE including Nb, Ta, and Ti (Fig. 8). Such geochemical features are commonly attributed to typical subduction-related magmas that developed in arc settings (Gill, 1981; Hawkesworth et al., 1993; Pearce and Peate, 1995; Tatsumi and Eggins, 1995). The timing of magmatism and hydrothermal activity at Gicik clearly post-dates the Late Cretaceous continental arc magmatism in the Pontides and subsequent Pontide-ATB collision, thereby indicating a post-subduction setting for the Gicik Au-Ag ± Te system. In such a tectonic scenario, the most likely source for magmatism seems to be remelting of the arc lithosphere that was

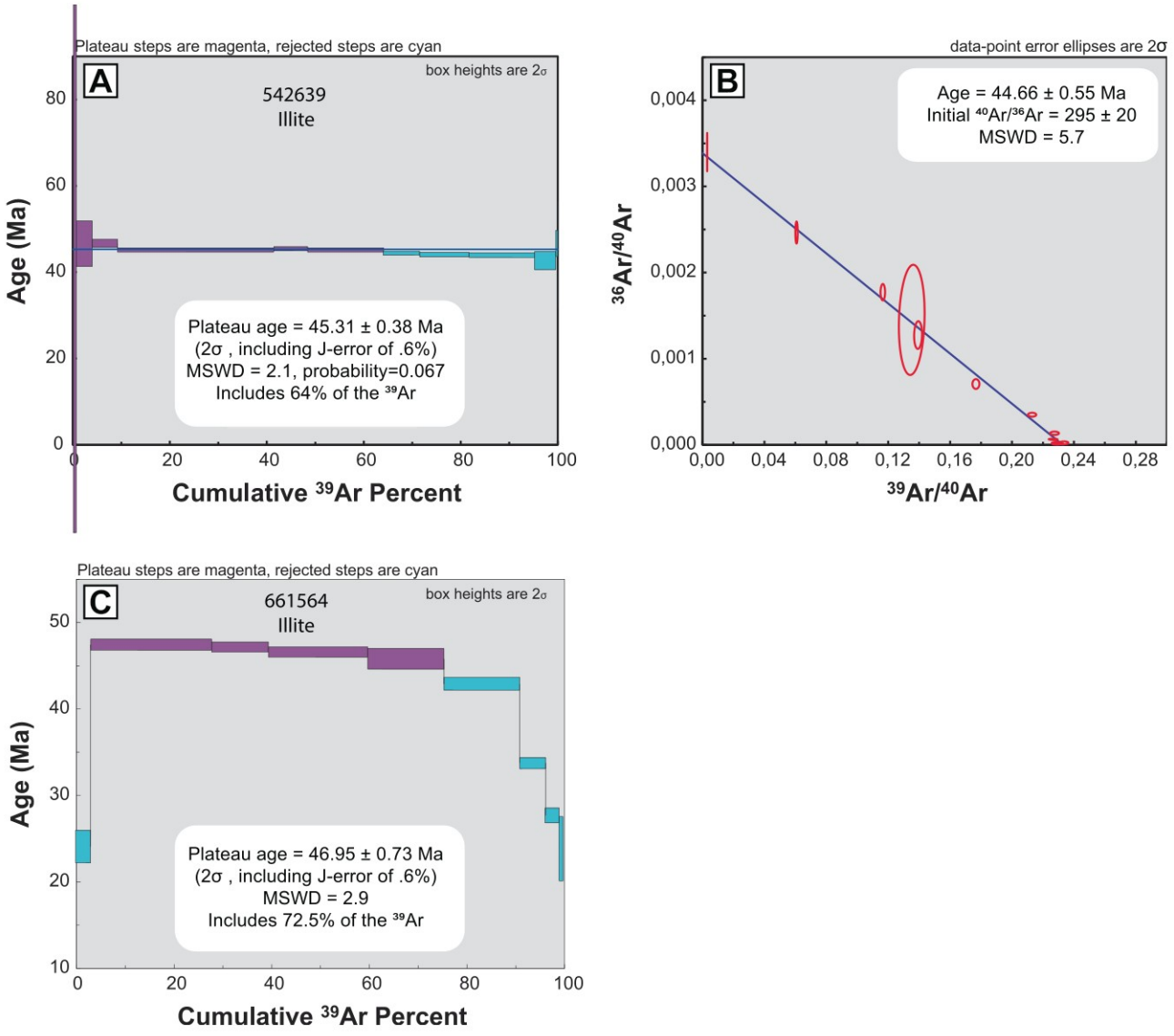


Fig. 16. $^{40}Ar/^{39}Ar$ spectra and inverse isochron plots of sericite from hydrothermally-altered rock samples form Gicik. A and B) Sample 496925E542639 (coordinates: 494683E, 4428863N), C) Sample 494683E661564 (coordinates: 496925E, 4428816N).

Table 8
Summary of $^{40}Ar/^{39}Ar$ geochronological analyses of hydrothermal sericite from the Gicik deposit.

Sample	Lithology	Mineral	%^{39}Ar released (plateau)	%^{39}Ar plateau age (Ma ± 2σ)	$^{40}Ar/^{39}Ar$ isochron age (Ma ± 2σ)	$^{40}Ar/^{39}Ar$ inverse isochron age (Ma ± 2σ)	Total Gas Age (Ma ± 2σ)
542639	Altered hydrothermal breccia	Sericite	64	45.31 ± 0.38	44.42 ± 0.58	44.66 ± 0.55	44.44 ± 1.30
661564	Altered argillized dacite	Sericite	72.5	46.95 ± 0.73	48.00 ± 3.6	–	44.14 ± 0.53

metasomatized during early subduction in the Late Cretaceous.

Gicik samples have Sr/Y and La/Yb ratios ≥ 20 in the adakitic to weakly sub-adakitic range (Fig. 9E and F). On the chondrite-normalized plots (Fig. 8), these samples also have listric-shaped REE patterns that display relative enrichments in LREE with respect to MREE and HREE, but they show broadly similar levels of enrichment in MREE and HREE ($[Dy/Yb)_N \sim 1$; Fig. 9A, Table 5). These, combined with whole-rock Eu_N/Eu^* ratios ~1 (i.e., lack of negative Eu anomalies), suggest the role of hornblende fractionation in the source (in the absence or delay of plagioclase fractionation) under relatively oxidizing and/or water-rich magmatic conditions (Hanson, 1980; Carmichael and Ghiorso, 1990; Moore and Carmichael, 1998). Ubiquitous presence of hornblende and biotite phenocrysts alongside common magnetite microphenocrysts in all samples are also in good keeping with the observed geochemical characteristics. One basaltic andesite dike sample is slightly enriched in all REEs with respect to dacitic volcanic-volcaniclastic lithologies (Fig. 8), but is otherwise identical to them geochemically (i.e., overall REE patterns and fractionating phases), and thus, it was possibly derived from the same melt source.

It remains unclear whether middle Eocene magmatic activity

Table 9
Summary of available geochronological data from north Ankara.

Sample	Location	Method	Mineral	Age (Ma ± 2σ)[a]	Reference
Igneous minerals					
Dacite	Bağlum	K/Ar	Biotite	42.00 ± 1.60	Ach (1982)
Dacite	ENE of Hüseyingazi Hill	K/Ar	Hornblende	38.80 ± 1.20	Ach and Wilson (1986)
Dacite	SE of Bağlum	K/Ar	Hornblende	44.50 ± 1.00	Ach and Wilson (1986)
Dacite	SE of Bağlum	K/Ar	Biotite	44.70 ± 1.00	Ach and Wilson (1986)
Dacite	NNW of Hüseyingazi Hill	K/Ar	Biotite	42.00 ± 1.00	Ach and Wilson (1986)
Dacite	NNW of Hüseyingazi Hill	K/Ar	Hornblende	41.70 ± 1.00	Ach and Wilson (1986)
Rhyolite	ENE of Bağlum	K/Ar	Biotite	43.20 ± 1.60	Ach and Wilson (1986)
Andesite	Hüseyingazi Hill	K/Ar	n.s.	44.80 ± 1.70	Dönmez et al. (2009)
Andesite, trachyandesite to dacite	Kurtsivrisi	K/Ar	n.s.	44.50 ± 1.70	Dönmez et al. (2009)
Hydrothermal minerals					
Altered hydrothermal breccia (542639)	Gicik	$^{40}Ar/^{39}Ar$	Sericite	45.31 ± 0.38	This study
Altered argillized dacite (661564)	Gicik	$^{40}Ar/^{39}Ar$	Sericite	46.95 ± 0.73	This study

n.s.: not specified.
[a] $^{40}Ar/^{39}Ar$ ages are reported as plateau ages unless otherwise indicated.

associated with Gicik mineralization is related to break-off of the northern Neotethyan oceanic lithosphere (Harris et al., 1994; Altunkaynak, 2007; Dilek and Altunkaynak, 2009; Ersoy et al., 2017) or renewed underthrusting following collision (Mueller et al., 2019). Slab break-off is commonly expected to be accompanied by widespread extension in the upper plate, but tectonic models from north and northwest central Türkiye does not indicate any major extensional period during the Paleocene–Eocene interval (Gökten et al., 1996; Kaymakçı et al., 2003; Meijers et al., 2010; Çinku et al., 2011; Mueller et al., 2019). Rather, compressional stress conditions prevailed for much of the period between the latest Cretaceous and Eocene due to ongoing indentation of the Pontides to the Kırşehir Massif at least until the end of the middle Eocene (Kaymakçı et al., 2003; Meijers et al., 2010). Our fault plane data from predominantly oblique-slip NNE-trending faults with reverse movement from Gicik corroborates with this and suggests that mineralized veins were likely formed under transpressional stress conditions during the collisional tectonic development of the southern Sakarya Zone margin.

5.2. Comparison with other regional Eocene to Miocene systems

Coeval magmatic rocks (50–44 Ma) farther to the west, including the Topkaya-Arapkuyusu plutons and the Yürükkaracaören volcanics near Sivrihisar and Nallıhan, show close similarities to Gicik samples in terms of their major and trace element geochemical characteristics including their overall trace element patterns, though these have slightly lower Sr/Y, La/Yb, and Eu_N/Eu^* than Gicik volcanics (Fig. 9B–F). Involvement of an enriched lithospheric mantle source in their formation is suggested by Güllü and Kadıoğlu (2022) based on $^{87}Sr/^{86}Sr$ and $^{143}Nd/^{144}Nd$ isotopic compositions. One exception to this in north central Anatolia appears to be the Eocene alkaline mafic lavas identified in the Nallıhan-Sarıcakaya areas (48–44 Ma; Göçmengil et al., 2022), which were interpreted to have formed from melting of a mélange-like source, but more fractionated volcanic lithologies (i.e., andesitic to dacitic) from these locations geochemically resemble those reported herein from Gicik. Göçmengil et al. (2022) further stated that the Nallıhan-Sarıcakaya volcanism developed during a phase of compression, rather than slab break-off-related extension. This is in agreement with our observation that the tectonomagmatic development of the Gicik volcanism was related to a period of compressional to weakly-transpressional stress conditions during the middle Eocene.

In contrary to the 50–44 Ma igneous units, older intrusions such as the ~59 Ma Karakaya granite (Güllü and Kadıoğlu, 2022) and the 58–56 Ma Günyüzü granitoids (Demirbilek et al., 2018) near Sivrihisar, are high-K calc-alkaline to shoshonitic, and are significantly more enriched in LILEs and depleted in HFSEs (Fig. 8). All Karakaya and most Günyüzü samples also display steeper REE patterns from LREE to HREE and notable negative Eu anomalies with the lowest Eu_N/Eu^* ratios (typically ≤ 0.8) among all Eocene igneous systems between north of Ankara in the east and the Biga Peninsula to the west (Fig. 8 and 9B). They are also distinguished from 50–44 Ma igneous rocks with elevated $^{87}Sr/^{86}Sr$ ratios, which were interpreted to reflect significant crustal involvement (Güllü and Kadıoğlu, 2022). This older cluster of granitoids were likely emplaced during early stages of collision, whereby greater degrees of crustal assimilation imparted distinctive whole-rock geochemical and isotopic signatures that distinguish them from the 50–44 Ma igneous units. It should be noted that the Karakaya granite within this group is spatially-associated with the adjacent Kaymaz Au deposit, but neither Karakaya nor the Günyüzü granitoids are known to be related to any magmatic-hydrothermal mineralization such as porphyry- and epithermal-type mineralization.

Major and trace element characteristics of middle Eocene magmatic rocks hosting numerous important porphyry-, epithermal-, and skarn/CRD-style mineralizations in the Biga district are also compared against Gicik samples in Figs. 7–9. Intermediate to felsic composition host intrusive and/or extrusive rocks from the Halilağa porphyry Cu-Au and Kartaldağ and Madendağ epithermal Au-Ag deposits, as well as those from the TV Tower district have sub-alkaline, medium- to high-K, and predominantly metaluminous character (Fig. 7B and C). They are relatively enriched in LILE and depleted in HFSE (Fig. 8). Their REE abundances are comparable to those from Gicik as they are relatively-enriched in LREE with respect to MREE and HREE, and have listric-shaped REE patterns with no to minor negative Eu anomalies (0.80–1.03). Although most have sub-adakitic Sr/Y and La/Yb ratios below Gicik samples (Fig. 9C–F), these were also derived from hornblende fractionated melts that are sufficiently hydrous and oxidized to potentially form porphyry- and associated epithermal-style deposits.

The advanced stages of post-collisional magmatism near Ankara are represented by the Miocene (22.5–7.5 Ma) GVP, formation of which is generally attributed to southward slab retreat and attendant regional extension with or without lower crustal delamination (e.g., Wilson et al., 1997; Tankut et al., 1998; Adıyaman et al., 2001; Varol et al., 2007, 2014; Helvacı et al., 2014; Karaoğlu et al., 2024). GVP comprises a diverse range of extrusive rocks from mafic alkaline trachybasalts to intermediate to felsic composition, high-K calc-alkaline andesites to rhyolites, which also strongly inherited subduction signatures (i.e., LILE-enriched, and depleted in HFSE such as Nb, Ta; Figs. 7–9). Sub-alkaline andesitic–rhyolitic volcanics have REE patterns almost identical to those from Gicik (only slightly LREE-enriched) without any notable Eu anomalies. Sr/Y and La/Yb ratios of GVP samples are highly variable, but interestingly a number of these have markedly high Sr/Y and La/Yb ratios (Fig. 9C–F). The same suite of samples also has Eu_N/Eu^* ratios

close to 1 (Fig. 9B) indicative of high magma oxidation states and water contents, and thus may be conducive to generate magmatic-hydrothermal mineralization observed elsewhere along the Cenozoic magmatic belt in northern Türkiye (Fig. 1). Nevertheless, igneous rocks of the GVP are currently not known to contain any significant mineralization.

5.3. Formation conditions of mineralized veins at Gicik

Gicik Au-Ag ± Te mineralization is hosted by a series of up to several-meters-thick, steeply-dipping sub-parallel veins that were emplaced in closely-spaced NNE-SSW-trending faults (Fig. 15). All veins are dominated by silica with various clays, carbonate, and sulfides as minor components. Vein textures including massive, colloform-banded, brecciated and bladed textures are well-developed along a vertical window of ~300 m, with most being restricted to an interval of ~100 m. Cross-cutting relationships observed between these textural styles from early massive veins to later colloform-banded to brecciated ores indicate that the mineralizing system built up progressively. Volcanic-volcaniclastic lithologies are everywhere altered to some degree at Gicik. Alteration is typically zoned from regional and distal propylitization (epidote-chlorite-carbonate-pyrite) to an inward zone of argillic (kaolinite-sericite/illite–smectite-quartz ± adularia) and then silicic alteration in the core. Alteration intensity shows a marked increase towards siliceous veins. Co-existence of illite and kaolinite in altered wall-rocks suggests fluid pH levels of 4–5, and the predominance of illite (rather than muscovite) in argillic alteration zones combined with ore mineralogy suggests formation temperatures between 100° and 250°C at depths below 300 m (Reyes, 1990; Hedenquist et al., 2000).

Majority of veins at Gicik, either barren or mineralized, are characterized either by abundant colloform-banded amorphous silica (Fig. 13) or euhedral, inclusion-free quartz that has been recrystallized from an amorphous silica precursor as indicated by mosaic and feathery/plumose textures in these quartz crystals (Fig. 13). Primary crystalline quartz seems to be rare, and where present; it mainly occurs either as late-stage vug fill or as individual clasts within breccia fragments that were likely transported upward from deeper parts of the hydrothermal system. Sulfides and gold are primarily present within colloform bands, and some are associated with veins with massive microcrystalline to mosaic quartz infill, whereas veins with lattice bladed textures are relatively weakly-mineralized and those with rare amethystine quartz are typically barren. Initial fluids from which these colloform-banded veins formed should have low temperatures (<180°C; Fournier, 1985) that stabilized amorphous silica at shallow depths.

Abundant colloform-banded silica identified in the veins alongside rare adularia as well as the presence of lattice-bladed quartz textures suggest that boiling was the main ore precipitating mechanism at Gicik (Simmons and Browne, 2000; Moncada et al., 2012). Fluid inclusion assemblages comprising co-existing vapor-rich and liquid-rich two-phase inclusions were not identified in any of our mineralized vein samples, but amorphous silica (or derivative recrystallized quartz) often does not host such primary boiling assemblages, especially when colloform banding develops through vigorous boiling ("flashing" or "flash vaporization"; Buchanan, 1979; Moncada et al., 2012). Au-Ag ± Te mineralization is well-developed within this boiling horizon, but average grades vary significantly within narrow drill hole intervals, from several 10 s of g/t to 0.2–0.5 g/t Au. This also implies that ore deposition occurred in a dynamic system, where constrictions along steeply-dipping faults likely provided fluid throttling points during intermittent boiling (Rowland and Simmons, 2012) and also focused fluid flow.

In their study on the Acupan Au-Ag-telluride deposit, numerical modeling by Cooke and McPhail (2001) showed that Te-rich ores formed from boiling fluids of possible magmatic origin and that most Te fractionated into the vapor phase upon boiling. Such vapors are predicted to deposit telluride-bearing precious metal ores through condensation into shallow meteoric waters. According to Cooke and McPhail (2001), calaverite precipitation then occurs at significantly low temperatures (<125°C). We propose that main stage telluride-bearing Au veins at Gicik with calaverite as the main telluride phase may have formed through a similar mechanism at shallow depths and at temperatures below 200°C. In this case, the higher homogenization temperatures (up to 240°C) measured from quartz by Besbelli and Varol (2002) may not reflect the temperatures of the actual gold-mineralizing fluids, but rather represent those that are responsible for recrystallization of amorphous silica or conditions of post-ore stage fluids.

At Gicik, sulfide ores are often not well preserved at the surface due to variable degrees of weathering and oxidation. Still, relatively better-preserved vein samples contain a simple sulfide assemblage of pyrite-marcasite-arsenopyrite representing the early-stage mineralization and indicating low fluid fS_2 and fO_2 conditions as well as low fluid temperatures (<250°C). Low temperatures of the ore fluids are also confirmed by preliminary microthermometric data of Besbelli and Varol (2002). This assemblage and the low total sulfide abundance (<5 vol.%) of mineralized veins alongside textural and alteration features at Gicik are characteristic for low-sulfidation epithermal systems (Hedenquist et al., 2000; Simmons et al., 2005). Gold grades at this stage appear to be low, and refractory gold is associated with Fe-sulfides, primarily with pyrite.

Most Au was introduced into the epithermal system late within the life span of the Gicik hydrothermal system. Main mineralization stage is characterized by an increased abundance of base metals such as Cu and Zn as well as by significant enrichments in Au, Ag, Sb, Te, and Se. This element suite conforms well with the observed ore mineral assemblage in late, Au-Ag-Te-bearing breccia veins including Ag-tetrahedrite, chalcopyrite, sphalerite, and Au-Ag tellurides (alongside ubiquitous pyrite). Overprinting of early pyrite-marcasite-arsenopyrite with these late sulfide-telluride-gold assemblages in main stage veins reflects notable changes in fluid composition such as increased sulfidation states (Einaudi et al., 2003) and possibly fluid salinities. This late ingress of fluids may be associated with recharging by deeply-exsolved magmatic fluids in contrast to earlier fluids responsible for formation of pyrite-arsenopyrite-marcasite ores. It is generally accepted that low-sulfidation epithermal systems are primarily dominated by meteoric fluid convection in the shallow crustal levels and that contributions from magmatic fluids are relatively insignificant (Hedenquist et al., 2000; Sillitoe and Hedenquist, 2003; Simmons et al., 2005). Recently however, Gao et al. (2021, 2025) surmised that telluride-rich ores in low-sulfidation epithermal systems form from fluids of magmatic origin. Additionally, rare quartz fragments in hydrothermal breccias host primary, halite-bearing fluid inclusions with minute opaque daughters coexisting with vapor-rich two-phase fluid inclusions (Fig. 13I). The former type of fluid inclusions closely resembles quartz-hosted hypersaline inclusions in high-temperature porphyry-style veinlets (i.e., A- or B-type veinlets). This may also be indicative of a magmatic plumbing system underneath the Gicik epithermal mineralization, and that variations in fluid chemistry and ore mineralogy were dictated by degree of contribution from this potential source at depth. We should however note that these inclusions were only encountered rarely, and in the absence of an obvious sub-volcanic intrusion and drilling beyond the levels of known epithermal mineralization, we can only speculate on the presence of a porphyry system underneath Gicik. This observation calls for detailed isotopic and fluid inclusion analyses to constrain the source (s) ore-forming fluids.

The underexplored central segment of the Eocene magmatic belt contains a few porphyry occurrences including the Alaplı porphyry Cu prospect, which is located about 180 km northwest of Gicik. Given the favorable magma compositions, the magmatic centers in north Ankara, including Gicik, also have the potential to host deeper porphyry systems similar to Alaplı, Muratdere, and Halilağa. However, spatially- and temporally-associated porphyry–low-sulfidation epithermal systems are globally rare; the Sari Gunay Au-Ag deposit in NW Iran represents an

important example for such an association from this segment of the Tethyan belt. There, low-sulfidation-style veinlets progress into deeper sericite and locally K-feldspar altered porphyritic units containing banded quartz-sulfide-magnetite veinlets analogous to those observed in the Au-rich porphyry systems of the Maricunga Belt (Richards et al., 2006). Such examples are currently not known in Türkiye.

5.4. Epithermal-style mineralization and significance of telluride ores

The occurrence of telluride minerals in the Gicik vein system is distinctive among known magmatic-hydrothermal deposits of the Turkish part of the Tethyan belt. Rare Au tellurides were previously reported from the Küçükdağ HS epithermal Au-Ag prospect (Smith et al., 2016) in the Biga Peninsula. Recently, Tüysüz et al. (2023) showed that the Mastra intermediate-sulfidation epithermal deposit in Eastern Pontides also contains a variety of Au-Ag-Bi telluride phases. Both Küçükdağ and Mastra are post-subduction-related epithermal systems developed along the collisional belt between the Pontides and the ATB. Calc-alkaline magmatic activity at Mastra (~45 Ma; Tüysüz et al., 1995) is broadly contemporaneous with Gicik, whereas Küçükdağ is related to the younger, Oligocene post-collisional magmatic activity in the western part of the belt (Leroux, 2016).

Te-rich epithermal systems often develop in post-subduction to back-arc settings in particular association with extensional alkaline magmatism (e.g., Richards, 1995; Jensen and Barton, 2000; Richards et al., 2006; Harris et al., 2013; Kelley and Spry, 2016). Besides the archetypal examples of alkalic epithermal deposits such as Cripple Creek, Porgera, Ladolam, and Emperor, telluride-rich low-sulfidation epithermal deposits related to calc-alkalic magmatism also occur in compressional to extensional arc segments. Some examples of this type include the Acupan deposit in the Philippines (Cooke and McPhail, 2001), Sacarâmb in Romania (Alderton and Fallick, 2000), Perama Hill, Pefka, and Kassiteres-Sappes district deposits in Greece (Voudouris et al., 2006, 2007, 2011), and Heilongjiang Belt deposits in China (Gao et al., 2022).

In post-subduction tectonic environments, small degree partial melting of previously-metasomatized sub-continental lithospheric mantle (SCLM) may produce high-K to alkaline magmas that are potentially enriched in siderophile and chalcophile elements including Cu, Au, platinum group elements, and Te (Richards, 2009, 2011; Holwell et al., 2019). Relatively high Te contents of these magmas were explained by incorporation of Te-rich seafloor sediments into mantle-derived magmas in a supra-subduction setting (Jensen and Barton, 2000; Ciobanu et al., 2006; Holwell et al., 2019), potentially leading to formation of gold-telluride ores in the porphyry-epithermal environment. Middle Eocene volcanic rocks in north central Anatolia are interpreted to be low degree partial melts of previously subduction-modified SCLM (Kasapoğlu et al., 2016; Göçmengil et al., 2022). However, these middle Eocene igneous rocks are commonly medium- to high-K in composition (Fig. 7C), rather than being alkaline, likely due to significant crustal interaction and fractionation in a thickened collisional orogen undergoing compression (Kasapoğlu et al., 2016). Tüysüz et al. (2023) proposed that melting of subducted sediments of the Sakarya Zone are the likely sources of Te and Bi enrichment in Mastra. This may also be true for the coeval Gicik epithermal system occupying a similar tectonic position with Mastra along the southern collided margin of the Sakarya Zone. There is no detailed account of Bi-Te enrichment mechanisms in Mastra as of yet, and as such a comparison to Gicik is currently not possible. Future studies providing robust geochemical datasets from Mastra and other regional Eocene epithermal systems will be essential to further validate the role of subducted sediments or any other candidate lower crustal sources in understanding of the apparent Te enrichment along the Eocene metallogenic belt in northern Türkiye. At this point, however, it can be speculated that at least some of the middle Eocene igneous complexes located along the İAESZ may potentially host Te-rich magmatic-hydrothermal mineralization.

5.5. Exploration implications

The geological, structural, and alteration/mineralization model put forward for the Gicik Au-Ag ± Te deposit shows many similarities to low-sulfidation epithermal systems worldwide (Simmons et al., 2005) including several such deposits identified in the Eocene magmatic belt in northwestern Türkiye (e.g., Ünal-İmer et al., 2013; Dilekler, 2022). Firstly, a zoned alteration is evident around the mineralized veins from an outer zone of propylitic alteration to vein proximal argillic alteration and silicification. The footprint of argillic alteration is occasionally much larger than the veins themselves, particularly when the vein wall-rocks are relatively permeable volcaniclastic lithologies such as agglomerates and tuffs. Within this broader domain of argillic alteration, which is dominated by kaolinite-illite-quartz (±smectite ± adularia ± carbonate) assemblages, alteration intensity increases significantly adjacent to the mineralized veins. Similar clay-silica alteration was identified in a number of locations within coeval volcanic units farther north, near Bağlum and Çubuk (Besbelli and Varol, 2002), and such areas can be considered as prospective targets for epithermal-style mineralization.

Higher grade mineralization at Gicik is generally confined to vein portions showing greater textural variety, where paragenetically late hydrothermal breccias overprint earlier milky quartz, gray silica-sulfide veins, and lattice bladed quartz. These domains were inherently controlled by pre-existing oblique-slip structures, and repeated fault reactivation might have assisted in superimposition of various textural styles. Ore-controlling structures are oriented roughly parallel to the orogen (Fig. 1), and they also have prominent oblique components, which generated domains of contraction for focused fluid flow. Recognition of such structures within the Eocene volcanic belt in north central Anatolia may be key for new target generation.

6. Conclusions

The Gicik Au-Ag ± Te deposit is one of the better-known examples of gold mineralization that lies within the relatively less-explored portions of the Eocene magmatic belt in northern Türkiye, whereas the western and eastern sectors of this belt are well-endowed for various types of magmatic-hydrothermal mineralization. Mineralized veins at Gicik are spatio-temporally associated with calc-alkaline dacitic volcanic-volcaniclastic rocks (~44.5 Ma) that developed in a transpressional setting following collision of the Pontide and ATB fragments.

The nature of magmatism and style of mineralization show close similarities to other Eocene-aged ore systems that are recognized particularly in the Biga Peninsula (e.g., Lapseki, Madendağ, and the TV Tower district systems; Ünal-İmer et al., 2013; Leroux, 2016). Development of Eocene magmatism and attendant porphyry-epithermal mineralization in the Biga Peninsula as well as in the Eskişehir-Bursa District have been largely attributed to extensional tectonics in response to slab roll back and or break-off (Altunkaynak, 2007; Rabayrol et al., 2021). However, this study and other research (e.g., Göçmengil et al., 2022) on Eocene magmatic complexes indicate that coeval magmatic activity in north-central Anatolia is related to a phase of regional transpression within a post-collisional environment.

Gicik veins display characteristic textural as well as alteration ore mineralogical features of low-sulfidation epithermal systems examples of which are also widely present along the collided portion of the Tethyan belt in northern Türkiye. Gicik is distinguished from other regional epithermal systems by its locally well-developed Te-rich mineralization although contemporaneous systems elsewhere along the belt may have been overlooked in terms of Te mineralization. This is because Te is mostly not assayed in most exploration drilling programmes in Türkiye. We suggest that Eocene post-subduction magmatism may have contributed to Te enrichment in the Gicik epithermal deposit as also recognized in Mastra intermediate-sulfidation epithermal deposit in the eastern Pontides (Tüysüz et al., 2023).

Funding

This project was funded by the McKinstry Fund granted by the Society of Economic Geologists (SEG) in 2018 through a graduate student research grant to A.Ç.

Declaration of competing interest

The authors declare that they have no known competing financial interests or personal relationships that could have appeared to influence the work reported in this paper.

Acknowledgements

The study presented here is A.Ç.'s M.Sc. research project carried out at the Middle East Technical University. We would like to thank Prof. Dr. İlkay Kuşcu (Muğla Sıtkı Koçman University) for providing Ar-Ar geochronological data and for permission for its use as a part of this project. We also appreciate discussions with Mesut Soylu (EMX Royalty) as well as with Hikmet Yavuz and Ahmet Mert Özözlü from Koza Gold, which were helpful for understanding of the Gicik mineralization in the early stages of this work/research. Aynur Küçük (Central Laboratories, METU) is thanked for her assistance with the electron microprobe analysis. The manuscript benefited greatly from comments by two anonymous reviewers. The authors thank International Association on the Genesis of Ore Deposits (IAGOD) for providing an APC waiver that supported publication of this article.

Appendix A. Supplementary data

Supplementary data to this article can be found online at https://doi.org/10.1016/j.oregeorev.2026.107345.

Data availability

Data will be made available on request.

References

Ach, J. A. (1982). The petrochemistry of the Ankara volcanics, central Turkey. Department of Geological Sciences, MSc, 145.

Ach, J. A., and Wilson, F. H. (1986). Potassium-Argon ages of volcanic rocks from near Ankara, central Turkey.

Adıyaman, Ö., Chorowicz, J., Arnaud, O.N., Gündoğdu, M.N., Gourgaud, A., 2001. Late Cenozoic tectonics and volcanism along the North Anatolian Fault: New structural and geochemical data. Tectonophysics 338 (2), 135–165.

Akal, C., 2013. Coeval Shoshonitic-ultrapotassic dyke emplacements within the Kestanbol pluton, Ezine–Biga peninsula (NW Anatolia). Turk. J. Earth Sci. 22 (2), 220–238.

Akyürek, B., Bilginer, E., Akbaş, B., Hemşin, N., Pehlivan, Ş., Altın, O., Soysal, Y., Dauer, E., Çatal, E., Sözeri, B., Yıldırım, H., Hakyemez, Y., 1984. Ankara-Elmadağ-Kaleclk Dolayının Temel Jeoloji özellikleri. Jeoloji Mühendisliği Dergisi 8 (2), 31–46 in Turkish.

Akyürek, B., Bilginer, E., Akbas, B., Hepsen, N., Sunu, O., Soysal, Y., 1982. The geology of the vicinity of Ankara-Elmadag-Kalecik. MTA Report 7298.

Aldanmaz, E., Pearce, J.A., Thirlwall, M.F., Mitchell, J.G., 2000. Petrogenetic evolution of late Cenozoic, post-collision volcanism in western Anatolia, Turkey. J. Volcanol. Geoth. Res. 102 (1–2), 67–95.

Alderton, D.H., Fallick, A.E., 2000. The nature and genesis of gold-silver-tellurium mineralization in the Metaliferi Mountains of western Romania. Econ. Geol. 95 (3), 495–516.

Altunkaynak, Ş., 2007. Collision-driven slab breakoff magmatism in northwestern Anatolia, Turkey. J. Geol. 115 (1), 63–82.

Altunkaynak, Ş., Genç, Ş.C., 2008. Petrogenesis and time-progressive evolution of the Cenozoic continental volcanism in the Biga Peninsula, NW Anatolia (Turkey). Lithos 102 (1–2), 316–340.

Altunkaynak, Ş., Sunal, G., Aldanmaz, E., Genç, C. Ş., Dilek, Y., Furnes, H., Foland, K., A., Yang, J., and Yıldız, M. (2012). Eocene granitic magmatism in NW Anatolia (Turkey) revisited: new implications from comparative zircon SHRIMP U–Pb and 40Ar–39Ar geochronology and isotope geochemistry on magma genesis and emplacement. *Lithos*, *155*, 289–309.

Aluç, A., Kuşcu, İ., Ulyanov, A., Selby, D., Antoine, C., Spikings, R., Moritz, R., 2024. Protracted metallogenic and magmatic evolution of the Kirazlı epithermal Au-Ag and porphyry Cu deposits, Biga Peninsula, NW Turkey: evidence from zircon U-Pb, muscovite 40Ar/39Ar, and molybdenite Re-Os geochronology. Miner. Deposita 59 (5), 885–905.

Aydınçakır, E., Şen, C., 2013. Petrogenesis of the post-collisional volcanic rocks from the Borçka (Artvin) area: implications for the evolution of the Eocene magmatism in the Eastern Pontides (NE Turkey). Lithos 172, 98–117.

Aygül, M., Okay, A.I., Oberhaensli, R., Sudo, M., 2016. Pre-collisional accretionary growth of the southern Laurasian active margin, Central Pontides, Turkey. Tectonophysics 671, 218–234.

Bachmann, O., Dungan, M.A., Bussy, F., 2005. Insights into shallow magmatic processes in large silicic magma bodies: the trace element record in the fish Canyon magma body, Colorado. Contrib. Miner. Petrol. 149 (3), 338–349.

Berber, F., Sayit, K., Göncüoğlu, M.C., 2021. Geochemistry and U-Pb ages from the Kösdağ Metavolcanics in the southern Central Pontides (Turkey): Complementary data for early late cretaceous island arc development in the Northern Neotethys. Turk. J. Earth Sci. 30 (1), 59–80.

Besbelli, A., Varol, B., 2002. Tekke volkanıtlerinde hıdrotermal alterasyon ürünü kıl mıneralleşmeleri (çubuk, Ankara KD). MTA 125 (1902), 121–137 in Turkish.

Brenan, J.M., Shaw, H.F., Phinney, D.L., Ryerson, F.J., 1994. Rutile-aqueous fluid partitioning of Nb, Ta, Hf, Zr, U and Th: implications for high field strength element depletions in island-arc basalts. Earth Planet. Sci. Lett. 128 (3–4), 327–339.

Brunetti, P. (2016). Magmatic-hydrothermal evolution and post-ore modifications of the Halilağa Porphyry Cu-Au deposit, NW Turkey. Master's thesis, University of British Columbia, Vancouver, Canada.

Buchanan, L. J., 1979. The Las Torres Mines, Guanajuato, Mexico: Ore controls of a fossil geothermal system. Unpublished Ph. D. dissertation, Colorado School of Mines, Golden, Colorado, 138 pp.

Büyükönal, G. (1971). Microscopical study of the volcanic rocks around Ankara. Communications de La Faculté Des Sciences de l'Université d'Ankara, 15c.

Çalgın, R., Ercan, T., Pehlivanoğlu, H., and Şengün, M. (1973). Ankara çevresi jeolojisi. Ankara (in Turkish).

Carmichael, I.S., Ghiorso, M.S., 1990. The effect of oxygen fugacity on the redox state of natural liquids and their crystallizing phases. Rev. Mineral. Geochem. 24 (1), 191–212.

Chambefort, I., Dilles, J.H., Longo, A.A., 2013. Amphibole geochemistry of the yanacocha volcanics, peru: evidence for diverse sources of magmatic volatiles related to gold ores. J. Petrol. 54 (5), 1017–1046.

Çil, A., İmer, A., Koç Oğuz, S., Chiaradia, M., Ulyanov, A., and Moritz, R. (2025, September 26–29). Zircon and Apatite Geochemical Insights into Porphyry Cu Fertility in the Artvin District During Subduction–Collision Transition. SEG 2025 Conference, Brisbane, Australia.

Çinku, M.C., Hisarlı, Z.M., Heller, F., Orbay, N., Ustaömer, T., 2011. Middle Eocene paleomagnetic data from the eastern Sakarya Zone and the central Pontides: Implications for the tectonic evolution of north central Anatolia. Tectonics 30 (1).

Çinku, M. C., Hisarli, M., Hirt, A. M., Heller, F., Ustaömer, T., Kaya, N., Öksüm, E., and Orbay, N. (2016). Evidence of Late Cretaceous oroclinal bending in north-central Anatolia: palaeomagnetic results from Mesozoic and Cenozoic rocks along the İzmir–Ankara–Erzincan Suture Zone.

Ciobanu, C. L., Cook, N. J., and Spry, P. G. (2006). Preface-Special Issue: Telluride and selenide minerals in gold deposits-how and why?. *Mineralogy and Petrology*, *87*(3-4), 163.

Cooke, D.R., McPhail, D.C., 2001. Epithermal Au-Ag-Te mineralization, Acupan, Baguio district, Philippines: numerical simulations of mineral deposition. Econ. Geol. 96 (1), 109–131.

Deer, W.A., Howie, R.A., Zussman, J., 1997. Rock-forming minerals, 2nd ed. The Geological Society, London.

Deer, W.A., Howie, R.A., Zussman, J., 1992. An Introduction to the Rock-forming Minerals, (2 nd ed.). Longman Scientific & Technical.

Delaloye, M., Bingöl, E., 2000. Granitoids from western and northwestern Anatolia: geochemistry and modeling of geodynamic evolution. Int. Geol. Rev. 42 (3), 241–268.

Demirbilek, M., Mutlu, H., Fallick, A.E., Sarıız, K., Kibici, Y., 2018. Petrogenetic evolution of the Eocene granitoids in eastern part of the Tavşanlı Zone in northwestern Anatolia, Turkey. Lithos 314–315, 236–259.

Dilek, Y., and Altunkaynak, Ş. (2009). Geochemical and temporal evolution of Cenozoic magmatism in western Turkey: mantle response to collision, slab break-off, and lithospheric tearing in an orogenic belt.

Dilekler, G. (2022). Mineralization, textural and alteration characteristics of the Şahinli (Sırakayalar and Karatepe) low-sulfidation epithermal deposit (Lapseki, NW Turkey). Master's thesis, Middle East Technical University.

Dokuz, A., Aydin, F., Karslı, O., 2019. Postcollisional transition from subduction-to intraplate-type magmatism in the eastern Sakarya zone, Turkey: Indicators of northern Neotethyan slab breakoff. Bulletin 131 (9–10), 1623–1642.

Dönmez, M., Akçay, A. E., Türkecan, A., Satır, M., Evcimen, Ö., Gündoğdu, E. A., and Görmüş, T. (2009). Ankara ve Yakın Çevresi Geç Kretase - Tersiyer Volkanitlerinin Stratigrafisi ve Yeni Yaş Bulguları, 62. Türkiye Jeoloji Kurultayı, Bildiri Özleri Kitabı, 2(S 632).

Einaudi, M.T., Hedenquist, J.W., Inan, E.E., 2003. Sulfidation state of fluids in active and extinct hydrothermal systems: Transitions from porphyry to epithermal environments. Spec. Publ. Soc. Econ. Geol. 10, 285–314.

Ercan, T., Satır, M., Steinitz, G., Dora, A., Sarıfakıoğlu, E., Adis, C., Walter, H.J., Yıldırım, T., 1995. Biga Yarımadası ile Gökçeada, Bozcaada ve Tavşan Adalarındaki KB Anadolu tersiyer volkanizmasinin özellikleri. MTA Dergisi 117, 55–86.

Ercan, T., Türkecan, A., Guillou, H., Satır, M., Sevin, D., Şaroğlu, F., 1998. Features of the Tertiary volcanism around Sea of Marmara. Bull. Miner. Res. Explor. 120 (120), 97–118.

Ersoy, E.Y., Palmer, M.R., Genç, Ş.C., Prelević, D., Akal, C., Uysal, İ., 2017. Chemo-probe into the mantle origin of the NW Anatolia Eocene to Miocene volcanic rocks: Implications for the role of, crustal accretion, subduction, slab roll-back and slab break-off processes in genesis of post-collisional magmatism. Lithos 288–289, 55–71. https://doi.org/10.1016/j.lithos.2017.07.006.

Fournier, R. O. (1985). The behavior of silica in hydrothermal solutions.

Frey, F.A., Chappell, B.W., Roy, S.D., 1978. Fractionation of rare-earth elements in the Tuolumne Intrusive Series, Sierra Nevada batholith. Calif. Geol. 6 (4), 239–242.

Gao, S., Hofstra, A.H., Zou, X., Valley, J.W., Kitajima, K., Marsh, E.E., Lowers, A.L., Adams, D.T., Qin, K., Xu, H., 2021. Oxygen isotope evidence for input of magmatic fluids and precipitation of Au-Ag-tellurides in an otherwise ordinary adularia-sericite epithermal system in NE China. Am. Mineral. 106 (12), 2003–2019.

Gao, S., Hofstra, A.H., Qin, K., Zou, X., Xu, H., 2025. Formation of bonanza Au-Ag-telluride ores in epithermal systems: Constraints from Cu-O isotopes and modeling. Am. Mineral. 110 (5), 709–720.

Gao, S., Hofstra, A.H., Qin, K., Xu, H., 2022. A case of Te-rich low-sulfidation epithermal Au-Ag deposits in a calc-alkaline magmatic arc, NE China. Ore Geol. Rev. 151, 105158.

Gill, J.B., 1981. The role of subducted ocean crust in the genesis of orogenic andesite. Orogenic Andesites Plate Tecton. 230–247.

Göçmengil, G., Gülmez, F., Karacik, Z., Aysal, N., 2022. Petrogenesis of Early Cenozoic Sarıcakaya–Nallıhan Volcanism in NW Turkey: Implications for the Geodynamic setting and Source Characterization of the Balkanatolia Magmatic Realm. Minerals 12 (12), 1572.

Gökten, E., Özaksoy, V., Karakus, K., 1996. Tertiary volcanic and tectonic evolution of the Ayas-Güdül-Celtikci region, Turkey. Int. Geol. Rev. 38 (10), 926–934.

Green, T.H., Pearson, N.J., 1985. Experimental determination of REE partition coefficients between amphibole and basaltic to andesitic liquids at high pressure. Geochim. Cosmochim. Acta 49 (6), 1465–1468.

Gribble, C.D., Hall, A.J., 1992. Optical mineralogy: Principles and practice. CRC Press.

Güllü, B., Kadıoğlu, Y.K., 2022. Magmatic signature of the closure of the northern branch of Neo-Tethys: Upper Paleocene-Middle Eocene magmatism at the boundary of Tavşanlı-Sakarya Zone (Turkey). Geological Quarterly 66 (2), 66-13.

Gündüz, M., & Asan, K. (2023). MagMin_PT: An Excel-based mineral classification and geothermobarometry program for magmatic rocks. Mineralogical Magazine 87(1), 1–9 Middlemost, E. A., 1994. Naming materials in the magma/igneous rock system. Earth Science Reviews 37(3–4), 215–224.

Gülyüz, N., Gülyüz, E., Shipton, Z.K., Kuşcu, İ., Lord, R.A., 2020. Geological and mineralization characteristics of the Kestanelik epithermal Au-Ag deposit in the Tethyan Metallogenic Belt, NW Turkey. Geosci. J. 24 (4), 407–424.

Gülyüz, E., Özkaptan, M., Kaymakci, N., Persano, C., Stuart, F.M., 2019. Kinematic and thermal evolution of the Haymana Basin, a fore-arc to foreland basin in Central Anatolia (Turkey). Tectonophysics 766, 326–339.

Hanson, G. (1980). Geochemical evolution of the continental crust. *Studies in Geophysics, Continental tectonics*, 151–157.

Harris, N.B., Kelley, S., Okay, A.I., 1994. Post-collision magmatism and tectonics in northwest Anatolia. Contrib. Miner. Petrol. 117, 241–252.

Harris, A. C., Cooke, D. R., Blackwell, J. L., Fox, N., and Orovan, E. A. (2013). Volcanotectonic setting of world-class alkalic porphyry and epithermal Au±Cu deposits of the southwest Pacific.

Hawkesworth, C. J., Person, G., Turner, S. P., Van Calsteren, P., and Gallagher, K. (1993). The continental lithosphere: a geochemical perspective. *Anais da Academia Brasileira de Ciencias*, *65*.

Hawthorne, F.C., Oberti, R., Harlow, G.E., Maresch, W.V., Martin, R.F., Schumacher, J. C., Welch, M.D., 2012. Nomenclature of the amphibole supergroup. Am. Mineral. 97 (11–12), 2031–2048.

Hedenquist, J.W., Arribas, A., Gonzalez-Urien, E., 2000. Exploration for epithermal gold deposits. Rev. Econ. Geol. 13 (1), 245–277.

Helvacı, C., Öztürk, Y.Y., Satır, M., Shang, C.K., 2014. U-Pb zircon and K-Ar geochronology reveal the emplacement and cooling history of the late cretaceous Beypazarı granitoid, central Anatolia, Turkey. Int. Geol. Rev. 56 (9), 1138–1155.

Holwell, D.A., Fiorentini, M., McDonald, I., Lu, Y., Giuliani, A., Smith, D.J., Keith, M., Locmelis, M., 2019. A metasomatized lithospheric mantle control on the metallogenic signature of post-subduction magmatism. Nat. Commun. 10 (1), 3511.

Irvine, T.N., Baragar, W.R.A., 1971. A guide to the chemical classification of the common volcanic rocks. Can. J. Earth Sci. 8 (5), 523–548.

Jensen, E. P., and Barton, M. D. (2000). Gold deposits related to alkaline magmatism.

Karaoğlu, Ö., Varol, E., Lustrino, M., Chiaradia, M., Toygar Sağın, Ö., Hemming, S.R., Uysal, İ., 2024. Large-volume and swift magmatic response to late Cenozoic segmentation of the subducted Neotethyan oceanic slab: evidence from the Galatian Volcanic Province, northwestern Turkey. Int. Geol. Rev. 66 (19), 3428–3456.

Karslı, O., Ketenci, M., Uysal, İ., Dokuz, A., Aydın, F., Chen, B., Kandemir, R., Wijbrans, J., 2011. Adakite-like granitoid porphyries in the Eastern Pontides, NE Turkey: potential parental melts and geodynamic implications. Lithos 127 (1–2), 354–372.

Kasapoğlu, B., Ersoy, Y.E., Uysal, İ., Palmer, M.R., Zack, T., Koralay, E.O., Karlsson, A., 2016. The petrology of Paleogene volcanism in the Central Sakarya, Nallıhan Region: Implications for the initiation and evolution of post-collisional, slab break-off-related magmatic activity. Lithos 246, 81–98.

Kaymakçı, N., White, S.H., Vandijk, P.M., 2003. Kinematic and structural development of the Çankiri Basin (Central Anatolia, Turkey): a paleostress inversion study. Tectonophysics 364 (1–2), 85–113.

Kaymakcı, N., Özçelik, Y., White, S.H., Van Dijk, P.M., 2009. Tectono-stratigraphy of the çankırı Basin: late cretaceous to early Miocene evolution of the Neotethyan suture zone in Turkey. Geol. Soc. Lond. Spec. Publ. 311 (1), 67–106.

Kelley, K. D., and Spry, P. G. (2016). Critical elements in alkaline igneous rock-related epithermal gold deposits.

Keskin, M., Genç, Ş.C., Tüysüz, O., 2008. Petrology and geochemistry of post-collisional Middle Eocene volcanic units in North-Central Turkey: evidence for magma generation by slab breakoff following the closure of the Northern Neotethys Ocean. Lithos 104, 267–305.

Koza Altın İşletmeleri A.Ş. (2025). *Annual activity report: January 1 – September 30, 2025.*

Kuşcu, İ., Tosdal, R.M., Gençalioğlu-Kuşcu, G., 2019. Episodic porphyry Cu (-Mo-Au) formation and associated magmatic evolution in Turkish Tethyan collage. Ore Geol. Rev. 107, 119–154.

Leroux, G., M. (2016). Stratigraphic and petrographic characterization of HS epithermal Au-Ag mineralization at the TV Tower district, Biga Peninsula, NW Turkey. Master's thesis the University of British Columbia, Vancouver, Canada.

Maniar, P.D., Piccoli, P.M., 1989. Tectonic discrimination of granitoids. Geol. Soc. Am. Bull. 101, 635–643.

McFall, K., Roberts, S., McDonald, I., Boyce, A.J., Naden, J., Teagle, D., 2019. Rhenium enrichment in the Muratdere Cu-Mo (Au-Re) porphyry deposit, Turkey: evidence from stable isotope analyses (δ 34S, δ 18O, δ D) and laser ablation-inductively coupled plasma-mass spectrometry analysis of sulfides. Econ. Geol. 114 (7), 1443–1466.

Meijers, M.J., Kaymakcı, N., Van Hinsbergen, D.J., Langereis, C.G., Stephenson, R.A., Hippolyte, J.C., 2010. Late cretaceous to Paleocene oroclinal bending in the central Pontides (Turkey). Tectonics 29 (4).

Moix, P., Beccaletto, L., Kozur, H.W., Hochard, C., Rosselet, F., Stampfli, G.M., 2008. A new classification of the Turkish terranes and sutures and its implication for the paleotectonic history of the region. Tectonophysics 451 (1–4), 7–39.

Moncada, D., Mutchler, S., Nieto, A., Reynolds, T.J., Rimstidt, J.D., Bodnar, R.J., 2012. Mineral textures and fluid inclusion petrography of the epithermal Ag–Au deposits at Guanajuato, Mexico: Application to exploration. J. Geochem. Explor. 114, 20–35.

Moore, G., Carmichael, I.S.E., 1998. The hydrous phase equilibria (to 3 kbar) of an andesite and basaltic andesite from western Mexico: constraints on water content and conditions of phenocryst growth. Contrib. Miner. Petrol. 130 (3), 304–319.

Morimoto, N., Fabries, J., Ferguson, A. K., Ginzburg, I. V., Ross, M., Seifert, F. A., Zussman, J., Aoki, K., and Gottardi, G. (1988). Nomenclature of pyroxenes. *Mineral. Mag.*, *52*(367), 535–550.

Mueller, M.A., Licht, A., Campbell, C., Ocakoğlu, F., Taylor, M.H., Burch, L., Ugrai, T., Kaya, M., Kurtoğlu, B., Coster, P.M.C., Métais, G., Beard, K.C., 2019. Collision chronology along the İzmir-Ankara-Erzincan suture zone: Insights from the Sarıcakaya Basin, western Anatolia. Tectonics 38 (10), 3652–3674.

Nairn, S. P., Robertson, A. H. F., Ünlügenç, U. C., Taşlı, K., and İnan, N. (2012). Tectonostratigraphic evolution of the Upper Cretaceous-Cenozoic central Anatolian basins: an integrated study of diachronous ocean basin closure and continental collision. Geological Society, London, Special Publications, 372, 343-384, 8 October 2012.

Okay, A.I., Göncüoğlu, M.C., 2004. The Karakaya complex: a review of data and concepts. Turk. J. Earth Sci. 13 (2), 75–95.

Okay, A.I., Nikishin, A.M., 2015. Tectonic evolution of the southern margin of Laurasia in the Black Sea region. Int. Geol. Rev. 57 (5–8), 1051–1076.

Okay, A.I., Sunal, G., Sherlock, S., Kylander-Clark, A.R., Özcan, E., 2020. İzmir-Ankara suture as a Triassic to cretaceous Plate Boundary—data from central Anatolia. Tectonics 39 (5), e2019TC005849.

Okay, A.I., Topuz, G., Kylander-Clark, A.R., Sherlock, S., Zattin, M., 2022. Late Paleocene–Middle Eocene magmatic flare-up in western Anatolia. Lithos 428, 106816.

Okay, A. I., and Şahintürk, O. (1997). AAPG Memoir 68: Regional and Petroleum Geology of the Black Sea and Surrounding Region. Chapter 15: Geology of the Eastern Pontides.

Okay, A.I., Tüysüz, O., 1999. Tethyan sutures of northern Turkey. Geol. Soc. Lond. Spec. Publ. 156 (1), 475–515.

Okay, A.I., Tüysüz, O., Satır, M., Özkan-Altıner, S., Altıner, D., Sherlock, S., Eren, R.H., 2006. Cretaceous and Triassic subduction-accretion, high-pressure–low-temperature metamorphism, and continental growth in the Central Pontides, Turkey. Geol. Soc. Am. Bull. 118 (9–10), 1247–1269.

Okay, A., Satır, M., 2006. Geochronology of Eocene plutonism and metamorphism in northwest. Geodin. Acta 19 (5), 251–266.

Parlak, B. (2016). Mayısılar (Sarıcakaya-Eskişehir) polimetalik cevher oluşumlarının jeolojik incelenmesi. Doctoral dissertation, Ankara University, Ankara, Turkey (in Turkish).

Pearce, J. A., and Peate, D. W. (1995). Tectonic implications of the composition of volcanic arc magmas. *Annual Review Of Earth And Planetary Sciences, Volume 23, pp. 251-286.*, *23*, 251-286.

Peccerillo, A., Taylor, S.R., 1976. Geochemistry of Eocene calc-alkaline volcanic rocks from the Kastamonu area, northern Turkey. Contrib. Miner. Petrol. 58, 63–81.

Pickett, E.A., Robertson, A.H., 1996. Formation of the late Palaeozoic–Early Mesozoic Karakaya complex and related ophiolites in NW Turkey by Palaeotethyan subduction–accretion. J. Geol. Soc. London 153 (6), 995–1009.

Prowatke, S., Klemme, S., 2006. Rare earth element partitioning between titanite and silicate melts: Henry's law revisited. Geochim. Cosmochim. Acta 70 (19), 4997–5012.

Rabayrol, F., Hart, C. J., Friedman, R. M., and Spikings, R. A. (2021). Diachronous Magmatic and Cu-Au-Mo Metallogenic Responses to Slab Roll-Back Initiation from Northwest Anatolia to the Balkans, Western Tethyan Eocene Magmatic Belt.

Revan, M.K., Demir, Y., Uysal, İ., Özkan, M., Dumanlılar, Ö., Şen, C., Kara, R.T., Hamzaçebi, S., Göç, D., Müller, D., Tokoğlu, M., 2024. Recently-discovered Bahçecik Au±Ag mineralization in the Eastern Pontides, Gümüşhane-NE Türkiye: geological

and geochemical implications on the intermediate sulfidation epithermal deposit. Int. Geol. Rev. 66 (15), 2673–2698.
Reyes, A.G., 1990. Petrology of Philippine geothermal systems and the application of alteration mineralogy to their assessment. J. Volcanol. Geoth. Res. 43, 279–309.
Rice, S.P., Robertson, A.H., Ustaömer, T., 2006. Late Cretaceous-Early Cenozoic tectonic evolution of the Eurasian active margin in the Central and Eastern Pontides, northern Turkey. Geol. Soc. Lond. Spec. Publ. 260 (1), 413–445.
Richards, J. P. (1995). Alkalic-type gold deposits: A review. *Magmas, fluids and ore deposits*.
Richards, J.P., 2009. Postsubduction porphyry Cu-Au and epithermal Au deposits: Products of remelting of subduction-modified lithosphere. Geology 37 (3), 247–250.
Richards, J.P., 2011. High Sr/Y arc magmas and porphyry Cu±Mo±Au deposits: just add water. Econ. Geol. 106 (7), 1075–1081.
Richards, J.P., Kerrich, R., 2007. Special paper: adakite-like rocks: their diverse origins and questionable role in metallogenesis. Econ. Geol. 102 (4), 537–576.
Richards, J.P., Wilkinson, D., Ullrich, T., 2006. Geology of the Sari Gunay epithermal gold deposit, northwest Iran. Econ. Geol. 101 (8), 1455–1496.
Ridolfi, F., Renzulli, A., Puerini, M., 2010. Stability and chemical equilibrium of amphibole in calc-alkaline magmas: an overview, new thermobarometric formulations and application to subduction-related volcanoes. Contrib. Miner. Petrol. 160 (1), 45–66.
Rowland, J.V., Simmons, S.F., 2012. Hydrologic, magmatic, and tectonic controls on hydrothermal flow, Taupo Volcanic Zone, New Zealand: implications for the formation of epithermal vein deposits. Econ. Geol. 107 (3), 427–457.
Rutherford, M., Hill, P., 1993. Magma Ascent rates from Amphibole Breakdown: an Experimental Study Applied to the 1980-1986 Mount St. Helens Eruptions. J. Geophys. Res. 98 (B11), 19667–19685.
Sánchez, M. G., McClay, K. R., King, A. R., and Wijbrams, J. R. (2016). Cenozoic crustal extension and its relationship to porphyry Cu-Au-(Mo) and epithermal Au-(Ag) mineralization in the Biga peninsula, northwestern Turkey.
Sayit, K., Göncüoğlu, M.C., Ellero, A., Ottria, G., Frassi, C., Marroni, M., Pandolfi, L., 2022. Late cretaceous arc magmatism in the southern Central Pontides: constraints for the closure of the northern Neotethyan branches. Ofioliti 47 (1), 19–35.
Seyitoğlu, G., Büyükönal, G., 1995. Geochemistry of Ankara Volcanics and the implications of their K-Ar dates on the Cenozoic stratigraphy of central Turkey. Turk. J. Earth Sci. 4, 77–92.
Sherlock, S., Kelley, S., Inger, S., Harris, N., Okay, A., 1999. 40 Ar-39 Ar and Rb-Sr geochronology of high-pressure metamorphism and exhumation history of the Tavsanli Zone, NW Turkey. Contrib. Miner. Petrol. 137, 46–58.
Sillitoe, R.H., Hedenquist, J.W., 2003. Linkages between volcanotectonic settings, ore-fluid compositions, and epithermal precious-metal deposits. Soc. Econ. Geolog. Spec. Publ. 10, 315–343.
Simmons, S.F., Browne, P.R., 2000. Hydrothermal minerals and precious metals in the Broadlands-Ohaaki geothermal system: Implications for understanding low-sulfidation epithermal environments. Econ. Geol. 95 (5), 971–999.
Simmons, S. F., White, N. C., and John, D. A. (2005). Geological characteristics of epithermal precious and base metal deposits. Economic Geology 100th Anniversary, 29(January 2005), 485–522.
Sipahi, F., Kaygusuz, A., Saydam Eker, Ç., Vural, A., Akpınar, İ., 2018. Late cretaceous arc igneous activity: the Eğrikar Monzogranite example. Int. Geol. Rev. 60 (3), 382–400.
Sisson, T.W., 1994. Hornblende-melt trace-element partitioning measured by ion microprobe. Chem. Geol. 117 (1–4), 331–344.
Smith, M. T., Lepore, W. A., İncekaraoğlu, T., Boran, H., Barrios, Q., Lerous, G., Ross, K., Büyüksolak, A., Sevili, A., Raabe (2016). High-sulfidation epithermal Au and porphyry Cu-Au mineralization at the Karaayı target Biga Penisula, northwestern Turkey. Society of Economic Geologists Special Publications pp. 85–112.
Sun, S.S., McDonough, W.F., 1989. Chemical and isotopic systematics of oceanic basalts: Imlications for mantle composition and processes. Geol. Soc. Lond. Spec. Publ. 42, 313–345.
Tankut, A., 1985. Ankara dolaylarındaki Neojen yaşlı volkaniklerin jeokimyası. Türkiye Jeoloji Bülteni 28 (1973), 55–66 in Turkish.
Tankut, A., Wilson, M., Yihunie, T., 1998. Geochemistry and tectonic setting of Tertiary volcanism in the Güvem area, Anatolia, Turkey. J. Volcanol. Geoth. Res. 85 (1–4), 285–301.
Tatsumi, Y., and Eggins, S. (1995). Subduction zone magmatism. In *Subduction zone magmatism*. Blackwell Science; Frontiers in Earth Sciences.
Topuz, G., Altherr, R., Schwarz, W.H., Siebel, W., Satır, M., Dokuz, A., 2005. Post-collisional plutonism with adakite-like signatures: the Eocene Saraycık granodiorite (Eastern Pontides, Turkey). Contrib. Miner. Petrol. 150 (4), 441–455.
Topuz, G., Okay, A.I., Altherr, R., Schwarz, W.H., Siebel, W., Zack, T., Satır, M., Şen, C., 2011. Post-collisional adakite-like magmatism in the Agvanis Massif and implications for the evolution of the Eocene magmatism in the Eastern Pontides (NE Turkey). Lithos 125 (1–2), 131–150.
Tüysüz, N., Yaylalı-Abanuz, G., Gümrük, O., Ar, B., 2023. Textural and genetic investigations of gold mineralization in fault-controlled quartz carbonate veins in Bayburt-Zarani area (Eastern Pontides-NE Turkey). Turk. J. Earth Sci. 32 (5), 277–600.
Tüysüz, O., Dellaloğlu, A.A., Terzioğlu, N., 1995. A magmatic belt within the Neo-Tethyan suture zone and its role in the tectonic evolution of northern Turkey. Tectonophysics 243 (1–2), 173–191.
Ünal-İmer, E., Güleç, N., Kuşçu, İ., Fallick, A.E., 2013. Genetic investigation and comparison of Kartaldağ and Madendağ epithermal gold deposits in Çanakkale, NW Turkey. Ore Geol. Rev. 53, 204–222.
Ustaömer, P.A., Ustaömer, T., Collins, A.S., Reischpeitsch, J., 2009. Lutetian arc-type magmatism along the southern Eurasian margin: New U-Pb LA-ICPMS and whole-rock geochemical data from Marmara Island, NW Turkey. Miner. Petrol. 96, 177–196. https://doi.org/10.1007/s00710-009-0051-8.
Ustaömer, T., Robertson, A.H.F., 1994. Late Palaeozoic marginal basin and subduction-accretion: the Palaeotethyan Küre complex, central Pontides, northern Turkey. J. Geol. Soc. London 151 (2), 291–305.
Van Hinsbergen, D.J., Maffione, M., Plunder, A., Kaymakcı, N., Ganerød, M., Hendriks, B. W., Corfu, F., Gürer, D., de Gelder, G.I.N.O., Peters, K., McPhee, P.J., Brouwer, F.M., Advokaat, E.L., Vissers, R.L., 2016. Tectonic evolution and paleogeography of the Kırşehir Block and the Central Anatolian Ophiolites. Turkey. Tectonics 35 (4), 983–1014.
Varol, E., Temel, A., Gourgaud, A., 2008. Textural and compositional evidence for magma mixing in the evolution of the çamlıdere volcanic rocks (Galatean Volcanic Province), Central Anatolia, Turkey. Turk. J. Earth Sci. 17 (4), 709–727.
Varol, E., Temel, A., Gourgaud, A., Bellon, H., 2007. Early Miocene adakite-like volcanism in the Balkuyumcu region, central Anatolia, Turkey: Petrology and geochemistry. J. Asian Earth Sci. 30 (5–6), 613–628.
Varol, E., Temel, A., Yürür, T., Gourgaud, A., Bellon, H., 2014. Petrogenesis of the Neogene bimodal magmatism of the Galatean Volcanic Province, Central Anatolia, Turkey. J. Volcanol. Geoth. Res. 280, 14–29.
Voudouris, P., Tarkian, M., Arikas, K., 2006. Mineralogy of telluride-bearing epithermal ores in the Kassiteres-Sappes area, western Thrace, Greece. Mineral. Petrol. 87 (1), 31–52.
Voudouris, P., Papavassiliou, C., Alfieris, D., Falalakis, G., 2007. Gold-silver tellurides and bismuth sulfosalts in the high-intermediate sulfidation Perama Hill deposit, western Thrace (NE Greece). Geol. Surv. Finland Guide 53, 77–84.
Voudouris, P.C., Melfos, V., Spry, P.G., Moritz, R., Papavassiliou, C., Falalakis, G., 2011. Mineralogy and geochemical environment of formation of the Perama Hill high-sulfidation epithermal Au-Ag-Te-Se deposit, Petrota Graben, NE Greece. Mineral. Petrol. 103 (1), 79–100.
Wilson, M., Tankut, A., Guleç, N., 1997. Tertiary volcanism of the Galatia province, north-west Central Anatolia. Turkey. Lithos 42 (1–2), 105–121.
Yavuz, H., Demir, Y., Kasapçı, C., Uysal, İ., Helvacı, C., 2022. Geology and genesis of the Silica-Listwaenite hosted Kaymaz gold deposit, Eskişehir, NW-Turkey: Implications from fluid inclusions and pyrite chemistry. J. Asian Earth Sci.: X 8, 100104.
Yilmaz, H., Oyman, T., Sonmez, F.N., Arehart, G.B., Billor, Z., 2010. Intermediate sulfidation epithermal gold-base metal deposits in Tertiary subaerial volcanic rocks, Sahinli/Tespih Dere (Lapseki/Western Turkey). Ore Geol. Rev. 37 (3–4), 236–258.
Yılmaz, B. (2005). Muratdere (Bozüyük-Bilecik)'deki Cu-Mo ve Au cevher oluşumlarının maden jeolojisi. Doctoral dissertation, Ankara University, Ankara, Turkey (in Turkish).
Yürür, T., Temel, A., Köse, O., 2002. Evidences of extensional tectonics at the southern boundary of the galatean volcanic Province, NW central anatolia. Geol. Bull. Turkey 45 (1), 85–98.
Zürcher, L., Bookstrom, A.A., Hammarstrom, J.M., Mars, J.C., Ludington, S.D., Zientek, M.L., Dunlap, P., Wallis, J.C., 2019. Tectono-magmatic evolution of porphyry belts in the central Tethys region of Turkey, the Caucasus, Iran, western Pakistan, and southern Afghanistan. Ore Geol. Rev. 111, 102849.